UNIVERSITÀ DEGLI STUDI DI TORINO
Facoltà di Scienze Matematiche Fisiche e Naturali
Corso di Laurea Magistrale in Fisica

Tesi di Laurea Magistrale

Study of P-Wave Bottomonium states with the CMS detector at LHC

Relatore:
Dott. Stefano Argirò

Controrelatore:
Dott. Stefania Beolè

Candidato:
Alessandro Degano

Luglio 2012 – A.A. 2011-2012

Contents

List of Figures

List of Tables

Abstract

This thesis presents the measurement of the $\frac{\sigma(pp\to\chi_b(2P))}{\sigma(pp\to\chi_b(1P))}$ ratio and the measure of χ_b(3P) barycenter with the CMS detector at LHC. The measurement was performed with $4.7fb^{-1}$ of pp collisions at $\sqrt{s} = 7TeV$ collected in 2011. The radial decay of P-wave states is considered and their product reconstructed, that is the Υ(1S) mesons and photons. The Υ(1S) meson is reconstructed through its decay in $\mu^+ + \mu^-$ while the photon is reconstructed when it converts into a positron-electron pair. The kinematic range covered is $|y(\Upsilon)| < 1.0$ and $p_T(\gamma) > 0.5$ GeV for the cross-section ratio measure, while $p_T(\gamma) > 1.0$ GeV for 3P barycenter measure.

Both measurements are compared to the theory predictions obtained with different models derived from QCD.

Thanks to the excellent performance of the CMS tracking system the observed resonances are very sharp and precise measurement are achieved. The relative reconstruction efficiency of the considered χ_b states is studied through various Monte Carlo simulations. Several source of systematic uncertainty are examined.

The production cross-section ratio is found to be: $\frac{\sigma(pp\to\chi_b(2P))}{\sigma(pp\to\chi_b(1P))} = 1.1 \pm 0.1(stat.) \pm 0.2(syst.) \pm 0.1(BR)$. This consitutes the first measurement of this quantity carried at a hadron collider.

The barycenter of 3P is found to be: $m_{\chi_b(3P)} = 10.509 \pm 0.004(stat.)^{+0.009}_{-0.011}(syst.)GeV$, in agreement with previous measurement performed by the ATLAS experiment and by the D0 experiment.

Abstract (in italiano)

Questa tesi presenta la misura della frazione $\frac{\sigma(pp\to\chi_b(2P))}{\sigma(pp\to\chi_b(1P))}$ e del baricentro del mesone χ_b(3P) con il detector CMS a LHC. Le misure sono state eseguite con $4.7fb^{-1}$ di collisioni pp a $\sqrt{s} = 7TeV$ raccolte nel 2011. Sono considerati i decadimenti radiativi degli stati in onda P e in mesoni Υ(1S) e fotone. Il mesone Υ(1S) è ricostruito attraverso il suo decadimento in $\mu^+ + \mu^-$ mentre il fotone è ricostruito mediante conversione in una coppia positrone-elettrone. La regione cinematica coperta è $|y(\Upsilon)| < 1.0$ e $p_T(\gamma) > 0.5$ GeV per la misura della sezione d'urto, mentre $p_T(\gamma) > 1.0$ GeV per la misura del baricentro del 3P.

Entrambe le misure sono comparate alle predizioni teoriche ottenute con diversi modelli derivati dalla QCD.

Grazie alle performance eccezionali del sistema di tracking di CMS le risonanze osservate sono molto strette e delle misure precise sono possibili. L'efficienza di ricostruzione relativa tra gli stati χ_b considerati è studiata a fondo attraverso varie simulazioni Monte Carlo. Diverse sorgenti di incertezza sistematica sono esaminate.

Il rapporto di sezione d'urto di produzione è valutato: $\frac{\sigma(pp\to\chi_b(2P))}{\sigma(pp\to\chi_b(1P))} = 1.1 \pm 0.1(stat.) \pm 0.2(syst.) \pm 0.1(BR)$. Questo costituisce la prima misura di questa quantità svolta ad un collisore adronico.

Il baricentro del 3P è valutato: $m_{\chi_b(3P)} = 10.509 \pm 0.004(stat.)^{+0.009}_{-0.011}(syst.)$ GeV, in accordo con le precedenti misure effettuate dall' esperimento ATLAS e dall' esperimento D0.

Introduction

In this thesis two measurements in the bottomonium P-wave spectrum are presented. The production cross-section of 2P over 1P states and the barycenter of the 3P state are measuered.

The first chapter will briefly summarize the theory underlying heavy quarkonia production at hadron colliders. The basics of the main theory models and their predictions will be reviewed to better understand the current status of research in the field. Moreover a brief summary of χ_b measurements at other hadron colliders is presented.

The second and third chapter of this thesis are devoted to the description of the Large Hadron Collider, its goals and some technical details. There will also be a description of the Compact Muon Solenoid experiment and its subdetectors, as the technical details of the subdetectors (tracking system in particular) will be useful in the later chapters of the thesis. This introductory section will also include some details about the software framework, the data storage model and the related computational challenge.

The fourth chapter contains all the details of the analysis from candidates selection cuts and conversion reconstruction to efficiency and acceptance estimation. Various sources of possible systematic errors will be examined.

In the bibliography references for technical details on the Large Hadron Collider, the Compact Muon Solenoid detector and all of its subdetectors can be found. Bibiliography references are also provided for theoretical models on quarkonia production and decays.

Chapter 1

Theory Overview and Previous Studies

1.1 Review on the Theory of Bottomonium Production and Decays

The quarkonium is a quark-antiquark bound state. Quarks with a mass higher than $\Lambda_{QCD} \simeq 300MeV$ (the scale at which perturbative expansion of QCD breaks), nominally the charm ($m_c \simeq 1.4GeV$), bottom ($m_b \simeq 4.5GeV$) and top ($m_t \simeq 175GeV$) quarks, are called "heavy". Heavy quarkonia are the bound states $Q\bar{Q}$, where Q is either a c or b quark. Due to the high mass and very short life-time, $t\bar{t}$ pairs are not known to form bound states (t quarks decay before bound states can be formed).

The lower-mass states of heavy quarkonium resonances are relatively stable particles: due to their mass below the threshold for open heavy flavored meson pair production, their decay modes are either electromagnetic or OZI-suppressed. The first excited state above the ground state for $c\bar{c}$ mesons is the J/ψ ($m_{J/\psi} \simeq 3.1GeV, \Gamma = 91keV$), while for $b\bar{b}$ mesons is the Υ ($m_\Upsilon = 9.46GeV, \Gamma = 54keV$). The excited states below the open charm/beauty threshold have widths ranging from a few dozens keV to a few dozens MeV. The spectrum of the bottomonium states is shown in Figure 1.1.

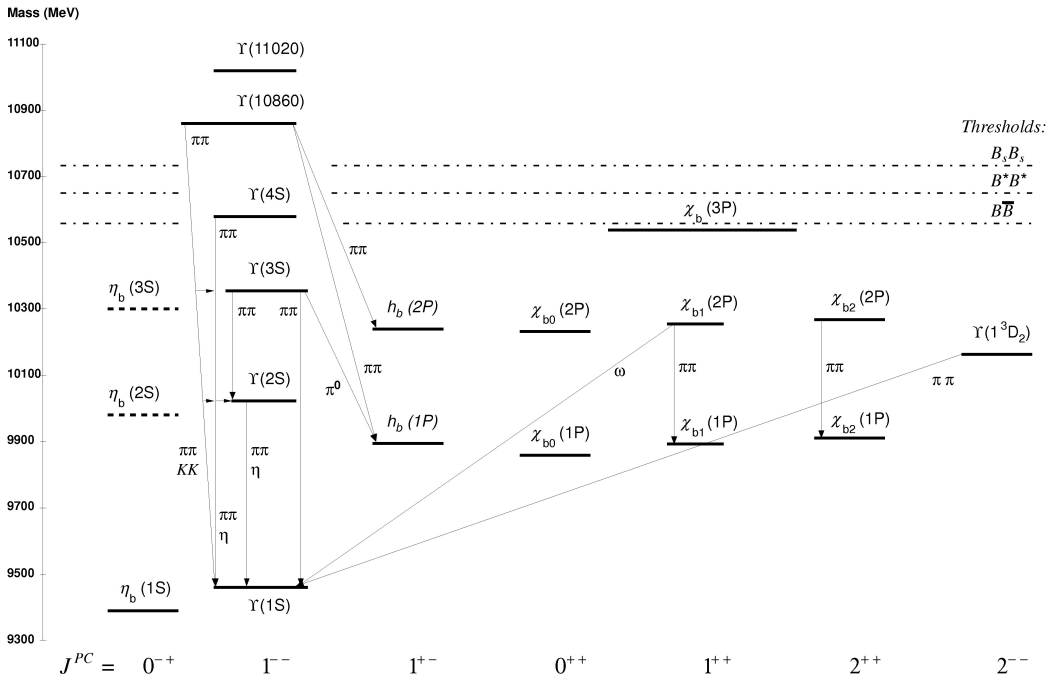

Figure 1.1: Bottomonium spectroscopy diagram

The spectroscopy of quarkonia is phenomenologically described by assuming that the $Q\bar{Q}$ pair is subjected to the Cornell potential, consisting of a Coulomb-like term accounting for gluon-exchange between the two quarks and a confining term parametrizing the non-perturbative effects:

$$V(r) = -\frac{4}{3}\frac{\alpha_s(r)}{r} + k^2 r \tag{1.1}$$

The results obtained by solving the Schroedinger equation with the potential in Equation 1.1 with ad-hoc values of the parameters are in fair agreement with the observed spectra.

The mechanism of quarkonium production at hadron colliders is still an open research field. For what concerns the identification of the partons involved in the production of the $Q\bar{Q}$ pairs, earlier experiments ruled out the hypotesis of electromagnetic production via quark-quark annihilation. Similarly, the hypotesis of $q\bar{q}$ annihilation into a gluon as the main production process was rejected after the comparison between the production rate in pp and in $p\bar{p}$ collisions, since the difference between the $\bar{q}$ content of proton and antiproton should lead to a suppression in pp collisions by a factor 5-10, which is not observed. Thus quarkonium production proceeds mainly via gluon fusion ($gg \rightarrow Q\bar{Q}$) or gluon fragmentation. In Figure 1.2 reporting the main tree level Feynman diagrams contributing to quarkonium production.

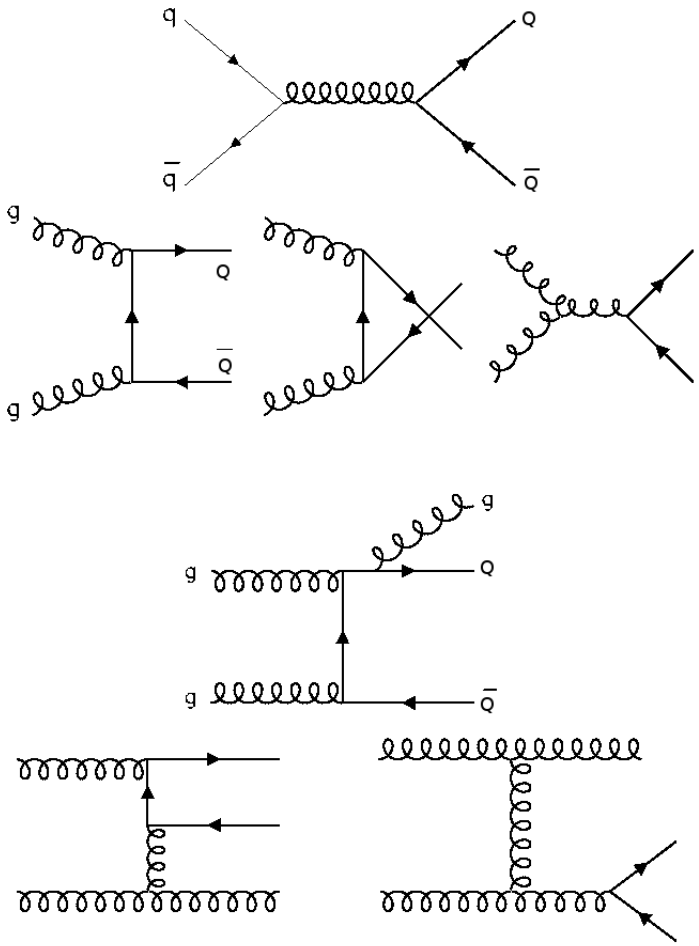

Figure 1.2: Main Feynman diagrams contributing to quarkonium production

In both heavy quarkonium annihilation decays and hard scattering production, large energy and momentum scales appear. The heavy quark mass m_Q is much larger than Λ_{QCD} and, in the case of production, the transverse momentum p_T can be much larger than Λ_{QCD} as well. This implies that the values of the QCD running coupling constant are much smaller than unity ($\alpha_S(m_c) \approx 0.25$ and $\alpha_S(m_b) \approx 0.18$). Therefore, one might hope that it would be possible to calculate the rates for heavy quarkonium decay and production accurately in perturbation theory. However, there are low-momentum, non-perturbative effects associated with the dynamics of the quarkonium bound state that invalidate the direct application of perturbation theory. In order to make use of perturbative methods, one must first separate the short-distance/high-momentum perturbative effects from the long-distance/low-momentum non perturbative effects; such a process is known under the name of factorization and nowadays is the basic approach to the problem of quarkonium production. Several models were developed over the years to describe theoretically or phenomenologically the quarkonia production mechanism and such models have been tested in the nineties on data collected at Tevatron.

1.1.1 Colour Evaporation Model (CEM)

The Colour Evaporation Model is the most phenomenological one and was first proposed in 1977. In the CEM, the production cross section for a quarkonium state H is a certain fraction F_H of the cross section for producing $Q\bar{Q}$ pairs with invariant mass below the $M\bar{M}$ threshold, where M is the lowest mass meson containing the heavy quark Q. This cross section has therefore an upper limit on the $Q\bar{Q}$ pair mass but no constraints on the colour or spin of the final state. The $Q\bar{Q}$ pair is assumed to neutralize its colour by interaction with the collision-induced colour field by colour evaporation. If the $Q\bar{Q}$ invariant mass is less than the heavy-meson threshold $2m_M$, then the additional energy that is needed to produce heavy-flavoured hadrons can be obtained from the nonperturbative colour field. Thus, the sum of the fractions F_H over all quarkonium states H can be less than unity. Further details about CEM can be found in references [15] [18] [17] [3].

The fractions F_H are assumed to be universal so that, once they are determined by data, they can be used to predict the cross sections for other processes and for other kinematic regions. The leading-order calculation cannot describe the quarkonium p_T distribution, since the p_T of the $Q\bar{Q}$ pair is zero at LO. At NLO in α_S the subprocesses $ij \to kQ\bar{Q}$ (where k is a light quark, antiquark or gluon) produce $Q\bar{Q}$ pairs with nonzero p_T . The most recent set of F_H values have been determined from complete NLO calculations of quarkonium production in hadronic collisions.

The most basic prediction of the CEM is that the ratio of the cross sections for any two quarkonium states should be constant, independent of the process and the kinematic region. Some variations in these ratios have been observed: for example the ratio of the cross sections for χ_c and J/ψ are rather different in photoproduction and hadroproduction. Such variations present a serious challenge to the status of the CEM as a quantitative model for quarkonium production, but nevertheless the model is still widely used as simulation benchmark.

1.1.2 Colour Singlet Model (CSM)

The colour-singlet model (CSM) was first proposed shortly after the discovery of the J/ψ. The main concept of the CSM is that, in order to produce a quarkonium, the $Q\bar{Q}$ pair must be generated with the quarkonium quantum numbers; in particular the pair has to be produced in a colour-singlet state. The CSM was succesfull in predicting quarkonium production rates at relatively low energy. However, recently, it has been found that at higher energies next-to-leading-order (NLO) and next-to-next-leading-order (NNLO) calculations in α_s rises very large corrections to CSM. It is, therefore, unclear if the perturbation expansions in α_s converges.

1.1.3 Non Relativistic QCD (NRQCD)

One convenient way to carry out the separation between perturbative and nonperturbative effects is through the use of the effective field theory called Non Relativistic QCD (NRQCD). NRQCD is more than a phenomenological model since it reproduces full QCD accurately at momentum scales of order $m_Q v$ and smaller, where v is the typical heavy quark velocity in the bound state in the CM frame ($v^2 \approx 0.3$ for charmonium, and $v^2 \approx 0.1$ for bottomonium). Virtual processes involving momentum scales of order m_Q

and larger can affect the lower-momentum processes, and their effects are taken into account through the short-distance coefficients of the operators that appear in the NRQCD action.

The $Q\bar{Q}$ pair can be produced in a colour-singlet state or in a colour-octet state. Its spin state can be singlet or triplet and it also can have orbital angular momentum. An important property of the matrix, which greatly increases the predictive power of NRQCD, is the fact that they are process independent; they can be calculated in lattice simulations or determined from phenomenology.

In practical calculations of the rates of quarkonium decay and production some uncertainties arises: in hadroproduction, for istance, the momentum transferred to the $Q\bar{Q}$, which is an important parameter for the calculation of quarkonia production, can only be evaluated statistically from the Parton Distribution Functions and the initial momentum of the hadrons colliding. In addition, the matrix elements are often poorly determined, either from phenomenology or lattice measurements. There are also large uncertainties in the heavy-quark masses (approximately 8% for m_c and approximately 2.4% for m_b) that can be very significant for quarkonium rates that are proportional to a large power of the mass. Many of the largest uncertainties in the theoretical predictions, as well as some of the experimental uncertainties, cancel out in the ratios of cross sections.

Another set of observables in which many of the uncertainties cancel out consists of polarization variables, which can be defined as ratios of cross sections for the production of different spin states of the same quarkonium. The NRQCD is in good agreement with data from CDF Run I for what concerns J/ψ and $\psi(2S)$ production cross sections but seems to fail in the case of $\Upsilon(1S)$ at low-pT because the NRQCD curve diverges like $1/p_T$ for small values of p_T.

In conclusion, NRQCD has been proved to be in good agreement with experimental results on quarkonium production cross sections. The measurement of polarization represents a further important test for the model. Further details about NRQCD can be found in references [4] [24] [16] [12].

1.2 The χ_b States

The observed P-wave triplets of Bottomonium are the 1P, the 2P and, very recently, the 3P. 1P and 2P states was first observed at Columbia University in 1983 and 1992 respectively, while the 3P state was first observed by ATLAS at LHC in December 2011 [25]. Spectroscopic information and symmetry properties of χ_b states and their mass and radiative decay branching ratio are shown in tables 1.1 and 1.2.

This analysis focuses on the radiative decays of the P-wave states of the Bottomonium which are the most probable for this states. As can be seen from table 1.2 the fine energy splitting between spin states of the same radial number n is rather low in comparison to the mass of the states themselves (e.g. 20 MeV between J=1 and J=2 spin states of the 1P triplet). Another important aspect of the nP triplets is that their J=0 spin states have very low Branching Ratio in radiative decay and therefore in an experiment they should have very much small yield with respect to the one of J=1 and J=2 states.

The theoretical models, through various approximations, are able to give very precise prediction of the levels of the Bottomonium spectroscopy, therefore an accurate measure-

ment of those states represent a very important benchmark for QCD models on meson production and decay.

Another important test can be done measuring the production cross-section ratio of different nP states. A significant source of uncertainty in theoretical models, indeed, is the initial wave-function of the mesons, however evaluating a ratio of cross-section of similar bound states cancel out some of the variables in the wave-function at the origin thus making the prediction easier.

Resonance	I^G	J^{PC}
$\Upsilon(1S)$	0^-	1^{--}
$\chi_{b0}(nP)$	0^+	0^{++}
$\chi_{b1}(nP)$	0^+	1^{++}
$\chi_{b2}(nP)$	0^+	2^{++}

Table 1.1: χ_b states quantum numbers, n=1,2,3.

	Mass [MeV]	BR($\chi_b \to \Upsilon(1S) + \gamma$)	$\Delta m(\chi_b, \Upsilon)$ [MeV]
$\chi_{b0}(1P)$	$9859.44 \pm 0.42 \pm 0.31$	$< 6\%$	399.1
$\chi_{b1}(1P)$	$9892.78 \pm 0.26 \pm 0.31$	$35 \pm 8\%$	432.5
$\chi_{b2}(1P)$	$9912.21 \pm 0.26 \pm 0.31$	$22 \pm 4\%$	451.9
$\chi_{b0}(2P)$	$10232.5 \pm 0.4 \pm 0.5$	$0.9 \pm 0.6\%$	772.5
$\chi_{b1}(2P)$	$10255.46 \pm 0.22 \pm 0.5$	$8.5 \pm 1.3\%$	795.2
$\chi_{b2}(2P)$	$10268.65 \pm 0.22 \pm 0.5$	$16.2 \pm 2.4\%$	808.4
$\chi_b(3P)$	$10539 \pm 4 \pm 8$	$(unkown)$	899

Table 1.2: Masses, branching ratios and Q-value of χ_b states from PDG.

Note that 3P mass refer to the barycenter of mass of the triplet of spin, since the single spin states have not yet been observed.

1.3 Previous studies of χ_b states at hadronic colliders

While χ_b 1P and 2P have been observed in a number of different experiment in both adronic and leptonic collisions, the 3P is a recent discovery. The Atlas collaboration observed first the state and, few months later, also the D0 collaboration [27] at Tevatron confirmed the existence of the state.

Both experiments reconstructed the χ_b candidates through their decay in Υ(1S) and a photon, Atlas observed the decay also in the Υ(2S) + γ channel. Both experiments search for converted photons from χ_b decay in their tracker, that is photons that through pair production converted in a couple of electron and positron allowing for a better resolution of the mass of the χ_b states. Atlas, however, confirmed the observation of the state also through electromagnetic calorimeter reconstructed photons.

The study published by the ATLAS collaboration is performed on the 2011 data, the kinematical selections used for the analysis are the following: Υ mesons are reconstructed

in the $\mu^+\mu^-$ decay channel, the dimuon must have transverse momentum $p_T > 12.0$ GeV and pseudorapidity $|\eta| < 2.0$. The photon must have $p_T > 1.0$ GeV and $|\eta| < 2.30$. The considered quantity in the study is the invariant mass difference Δm = $m_{\mu\mu\gamma}$ - $m_{\mu\mu}$ which is the difference between the invariant mass of the two muons from the Υ decay and the photon and the invariant mass of the dimuon alone. This technique minimizes the effect of the finite $\Upsilon \to \mu^+ + \mu^-$ mass resolution. In order to display the plot with the correct χ_b mass, the quantity $m_{\Upsilon(PDG)}$ which is the world average of the mass of the Υ(1S) is added to Δm. Finally a fit is performed on the distribution of Δm + $m_{\Upsilon(PDG)}$ using a Crystal Ball PDF for the signal shape, leaving the barycenter mass of the 3P triplet free. Further details on ATLAS analysis can be found in [25]. The result of the fit is shown in figure 1.3.

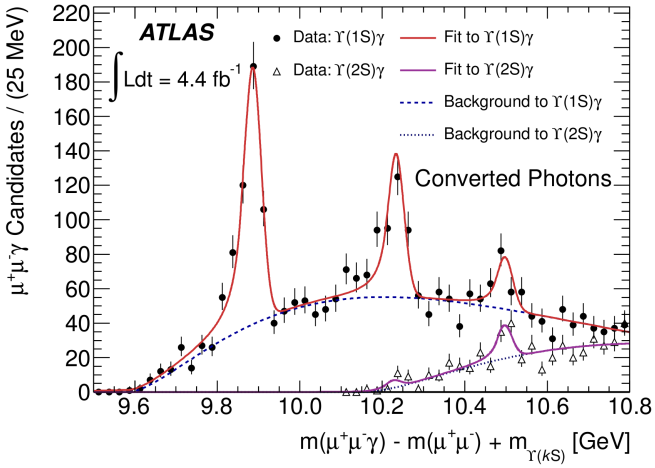

Figure 1.3: Invariant mass $m_{\mu\mu\gamma}$ - $m_{\mu\mu} + m_{\Upsilon(PDG)}$ obtained in ATLAS experiment with converted photons and it's fit.

Since the Atlas experiment is not able to separate the contribution of the individual spin states χ_{b1} and χ_{b2} only the barycenter of 3P state is evaluated, its value is $m_{\chi_b(3P)}$ = 10.539±0.004(stat.)±0.008(syst.) GeV. Atlas evaluate the significance of the 3P signal to be 6σ.

The D0 collaboration used the same technique used by ATLAS for his study: studying the decay $\chi_b \to \Upsilon(1S) + \gamma$ with $\Upsilon(1S) \to \mu^+\mu^-$, searching for converted photons and fitting the invariant mass $m_{\mu\mu\gamma}$ - $m_{\mu\mu} + m_{\Upsilon(PDG)}$. Since the experimental setup is different the kinematic selections are different as well: single muons must have $p_T > 1.5$ GeV, there is no kinematic selection on photons alone but the χ_b candidate must have $p_T > 5.0$ GeV. The fit to the invariant mass is again performed using Crystal Ball PDF to fit the signal. Further details on D0 measurement of 3P state can be found in [27]. The result of the fit is shown in figure 1.4.

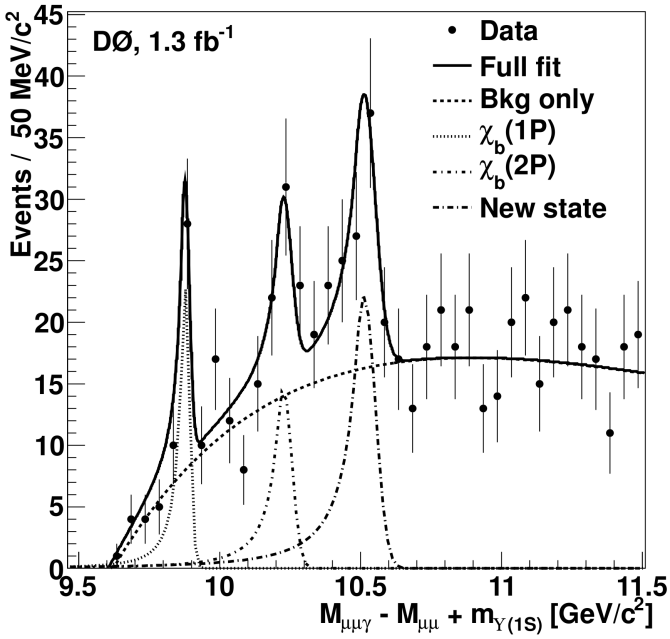

Figure 1.4: Invariant mass $m_{\mu\mu\gamma}$ - $m_{\mu\mu} + m_{\Upsilon(PDG)}$ obtained in D0 experiment with converted photons and it's fit.

The barycenter of 3P state is thus evaluated by the D0 collaboration to be $m_{\chi_b(3P)} = 10.551 \pm 0.014(\text{stat.}) \pm 0.017(\text{syst.})$ GeV, resulting compatible to the one found by ATLAS but less accurate.

Despite the several observation of the 1P and 2P χ_b states in different experiment over the years, no study was performed on the production cross-section ratio of the two states. Such a measure would be very useful to further test QCD models of the mesons production. The cross-section measurement, however, present several experimental difficulties: it generally depends on the reconstruction efficiency the experiment can achieve, they depend on the recorded Luminosity and on the kinematic region where the study is performed.

Studying a ratio of cross-section has the advantage of cancelling some of this dependences: the Luminosity cancels out when using the same dataset to reconstruct the two states, the kinematic region can be fixed to be the same for the two states and the absolute value of reconstruction efficiency is not needed to know but only the relative value of one state respect to the other.

1.4 Current theory prediction

Several theoretical works predicted in detail the structure of the Bottomonium spectrum and, therefore, the masses of the spin states of the 3P triplet.

The most recent of those works extends the standard NRQCD potential model to include the coupled-channel effect. In bottomonium, the process $(b\bar{b}) \to (b\bar{n})(n\bar{b})$ via light quark pair $n\bar{n}$ creation would induce the hadronic loop shown in figure 1.5, where

the initial bottomonium decays into intermediate virtual $B\bar{B}$ states and then reforms the original bottomonium state. Since the open-flavor decay couplings of bottomonium states to two-body $B\bar{B}$ final states are large, the resulting loop effects is important.

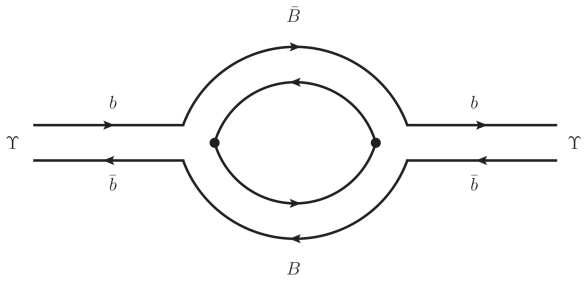

Figure 1.5: Hadronic loop in bottomonium state.

Finally this theoretical work predicts the mass of the triplet of 3P states of bottomonium to be: $m_{\chi_{b0}} = 10.4959$ GeV, $m_{\chi_{b1}} = 10.5173$ GeV, $m_{\chi_{b2}} = 10.5324$ GeV. Considering that χ_{b0} does not contribute to the barycenter of 3P and considering an approximate abundancy of J=2 over J=1 states of 0.5 the barycenter of 3P from the theoretical work would be $m_{3P} = 10.522$ GeV which is smaller than the value found by ATLAS but compatible with it. Further details of the work can be found in [19].

Despite theoretic models allow a prediction on the production cross-section ratio of 2P states over 1P states, only one work carried out the calculation to our knowledge. Developed using the Color Octet Model in Next to Leading Order (NLO), the work estimate the production cross-section ratio of 2P over 1P bottomonium states at LHC. At LHC energies the main contribution to $q\bar{q}$ production is given by gluon-gluon interaction, since the tipical fractions of proton momentum are rather small ($x \sim M/\sqrt{s} \sim 10^{-3}$) . The reasons to develop the calculation at NLO are twice: the total cross-section of eq. 1.2 is obtained by summing the single partonic cross-sections integrated over the gluon transverse momentum and at Leading Order gives no information on the p_T distribution of final quarkonia. Therefore, it is necessary to to consider at least NLO with the emission of an additional gluon in the final state, as shown in Feynman digrams of figure 1.6.

$$d\sigma[pp \to \chi_{bJ} + X] = \sum_{i,j} \int dx_1 dx_2 f_i(x_1) f_j(x_2) d\hat{\sigma}[\chi_{bJ}] \tag{1.2}$$

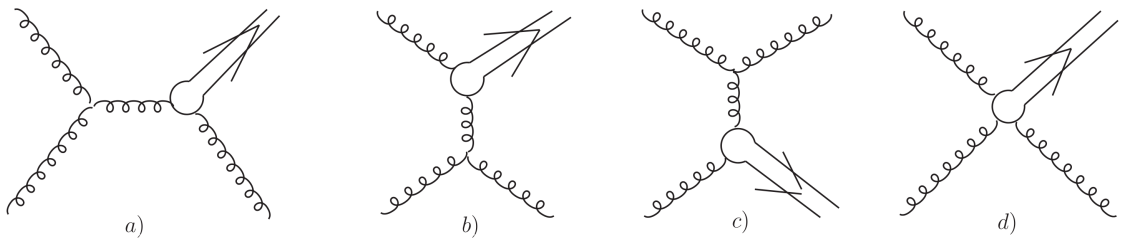

Figure 1.6: Feynman diagrams of the $gg \to \chi_b g$ subprocesses.

The second reason that requires a calculation at NLO is that at LO the Landau-Yang theorem forbid the production of axial mesons which, however, are abundantly observed in experiments. At NLO the production of axial mesons is allowed, reproducing the observed behaviour of Bottomonium production.

The work, then, assumes that the p_T distribution of χ_b at LHC is the same of those of χ_c multiplied by a scale factor. The only parameter left is the initial wave-function ratio of the quarkonia considered in the cross-section ratio. The results of the work are expressed for different potential models used to evaluate the wave function of the quarkonia and are reported in table 1.3, note that the Branching Ratios are alredy extracted from the results.

Potential Model	$\sigma(\chi_b(2P))/\sigma(\chi_b(1P))$
1	$0.4\pm0.01^{th}\pm0.14^{br}$
2	$0.25\pm0.01^{th}\pm0.1^{br}$
3	$0.32\pm0.02^{th}\pm0.1^{br}$
4	$0.34\pm0.01^{th}\pm0.12^{br}$
5	$0.34\pm0.01^{th}\pm0.12^{br}$
6	$0.14\ \pm0.05^{br}$

Table 1.3: Theoretical evaluation of $\sigma(\chi_b(2P))/\sigma(\chi_b(1P))$ for various potential models.

For further details on the work and reference to potential models used see [1].

As said alredy, there is no experimental work that studied the cross-section production of χ_b(2P) over χ_b(1P) neither at LHC nor in any other experiment, therefore the comparison with the just mentioned theory will be done in the present work in the relative chapter.

Chapter 2

LHC

The Large Hadron Collider (LHC) is -as of 2012- the world's largest and highest energy particle accellerator. It is located at CERN beneath the Franco-Swiss border near the city of Geneva. The LHC was designed to confirm the yet undetected prediction of the Standard Model (SM): the Higgs mechanism([22]), to probe for sign of the Supersymmetric extension of the SM and the quark-gluon plasma theories and generally to study particle physics at the TeV energy scale.

2.1 Technical design

The strict requirements needed to build a machine able to probe new physics up to the TeV energy scale imposed some design features:

- A hadron collider: The need of high energy collisions requires massive particles with low syncrotron radiaton to be used. The exact energy of interacting parton is thus unknown when colliding hadrons, it's mean can be, however, estimated. LHC desing collision energy is $\sqrt{s} = 14TeV$, being the mean partons momenta fractions $x_1, x_2 \cong 0.15 - 0.20$ the energy range which can be tipically explored is thus $\sqrt{\hat{s}} = \sqrt{x_1 x_2 s} = 1 - 2TeV$.

- Proton-Proton collision: With respect to a proton-antiproton machine it is easier to store and accumulate high intensity of proton beams. Furthermore the Higgs production process is dominated by gluon fusion, therefore its cross-section is nearly the same for proton-proton and proton-antiproton.

- High luminosity: The cross section determines the event rate R of a given process according to the formula $R = \mathcal{L}\sigma$. The factor $\mathcal{L}$ is called luminosity, it represents the number of collisions per unit time and cross-sectional area of the beams. It is specific to the collider parameters and does not depend on the interaction considered: $\mathcal{L} = \frac{fn1n2}{A}$ where f is the collision frequency of bunches composed of n1 and n2 particles and A is theoverlapping cross-sectional area of the beams. To compensate for the low cross section of the interesting processes the LHC must have a very high luminosity: the very short bunch crossing interval (25ns, frequency of 40M Hz) and the high number of bunches accelerated by the machine (2808 per beam) allows to reach the peak luminosity of $10^{34} cm^{-2} s^{-1} = 1 nb^{-1} s^{-1}$.

To meet the above requirements LHC was installed in the 27 km underground tunnel previously used for LEP. The keys features of the accellerator are the following:

- Circumference: 26.659 Km
- Centre of mass energy: 14 TeV per proton in pp collisions or 1148 TeV per nucleus in Pb Pb collisions.
- Dipole magnetic field: 8.3T.
- Number of particles per bunch: 2808 in pp collisions or 608 in Pb Pb collisions.
- Bunch length: 53mm in pp collisions or 75mm in Pb Pb collisions.
- Bunch crossing rate: 40.08 MHz in pp collisions or 0.0006 MHz in Pb Pb collisions.
- Design luminosity: $10^{34} cm^{-2} s^{-1}$ for pp collisions and $10^{27} cm^{-2} s^{-1}$ for Pb Pb collisions.
- Beam readius at interaction point: $15 \mu m$

The Large Hadron Collider posed new technological and engineering challenges to the scientific communities. In total, over 1,600 superconducting magnets are installed, each weighting over 27 tonnes. Approximately 96 tonnes of liquid helium are needed to keep the magnets, made of copper-clad niobium-titanium, at their operating temperature of 1.9K (271.25 C), making the LHC the largest cryogenic facility in the world at liquid helium temperature. In 2.1 a section of the superconducting magnet can be seen.

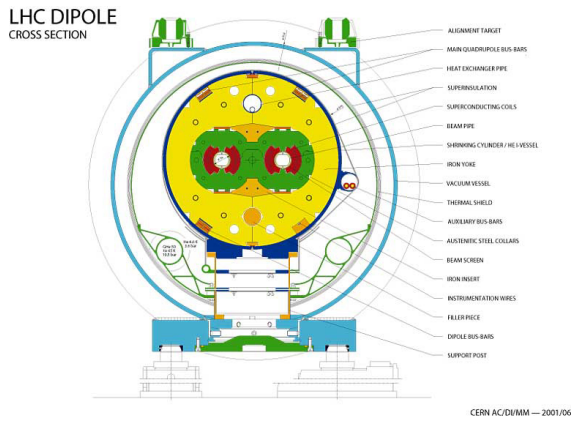

Figure 2.1: LHC dipole Cross-section.

One important downside aspect of LHC design is the overwhelming background process rate compared to the interesting physics processes: the Higgs production, for instance, has a cross section at least ten orders of magnitude smaller than the total inelastic cross section, as shown in 2.2. In fact, most of of the events produced in pp collisions is either due to low p_T scattering, where the protons collide at large distance, or to QCD high p_T processes. All these events are collectively called minimum bias and they are in

general considered not interesting since they constitute a background for other interesting processes, where massive particles like the Higgs are created in the hard scattering.

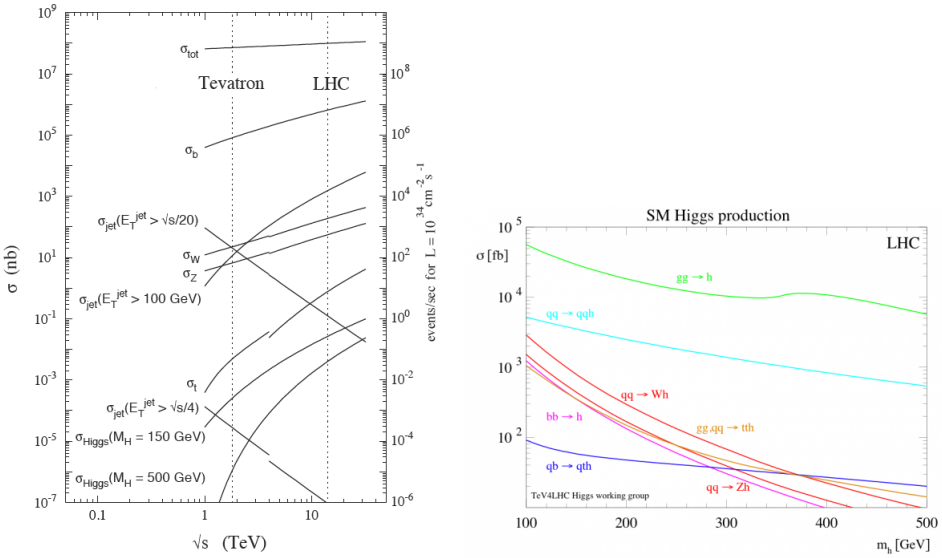

Figure 2.2: Production cross section of various SM predicted processes.

The proton remnants, that carry a good fraction of the proton energy, are scattered at small angles and are mostly lost in the beam pipe, escaping undetected. Experimentally, it is therefore not possible to define the total and missing energy of the event, but only the total and missing transverse energies. Thus, all the interesting physics observable are measured in the plane transverse to the beamline. The first beam was circulated through the LHC 10 September 2008. CERN successfully fired the proton beam around the tunnel in stages, however shortly after, on 19 September 2008, a quench occurred in about 100 bending magnet causing a loss of approximately six tonnes of liquid helium, which was vented into the tunnel. Most likely the cause of the problem was a faulty electrical connection between two magnets. A total of 53 magnets were damaged in the incident and were repaired or replaced during the winter shutdown, however almost a year passed before the LHC was put in function again. Due to this accident the LHC is now running with a reduced energy of collisions $\sqrt{s} = 7TeV$ instead of the project nominal energy of $\sqrt{s} = 14TeV$. According to the plans, LHC will run with $\sqrt{s} = 8TeV$ center of mass energy for the whole 2012, then there will be a shutdown for at lest one year to technically prepare LHC for running at $\sqrt{s} = 14TeV$. This technical stop is needed make sure that accidents like the one happened in 2008 won't happen again. During this time the various detectors installed at LHC may install upgrades to their sub-detectors systems to improve their performance in view of the higher energy, higher luminosity runs.

2.1.1 Experiments

The Large Hadron Collider is the host of six different experiment, each experiment has a different composition and geometry of the subdetectors so that it is more specialized in a

particular area of the research in particle physics. ATLAS (A Toroidal Lhc ApparatuS) and CMS (Compact Muon Solenoid) are two general-purpose, high-luminosity detectors; they are built with a cylindrical geometry around the beamline. Even if theoretically "general-purpose" detectors, these two have been designed for the discovery of new physics in the TeV scale, thus their subdetectors are optimized for the reconstruction of high energy objects with great efficiency and accuracy. With LHC steadly incresing interaction energy ATLAS and CMS will be able to observe new and yet unobserved particles with partons colliding up to 3-4 TeV. While similar in their purposes, the design of the two detectors differs significantly, since different solutions were chosen for the configuration of the magnetic field. ATLAS uses a toroidal field produced by three sets of air-core toroids complemented by a small solenoid in the inner region, while CMS uses a solenoidal field generated by the world's largest superconducting solenoid. ALICE (A Large Ion Collider Experiment) is a detector optimized for PbPb collisions, in particular for the study of the properties of matter at high temperature and high energy density generated by such collisions (Quark Gluon Plasma). LHCb is specialized in studies regarding the physics of heavy quarks and heavy mesons with a particular attention to the b quark and its mesons. TOTEM and LHCf are forward detectors of CMS and ATLAS repectively, they are placed 100m from the interaction points of the main experiments to study diffractive physics happening in the very forward region of the collision. Such detectors have to be put far from the interaction point so that the products of such very forward (i.e. high η, small angle with respect to the beamline) inelastic or elastic collisions may exit the beampipe. Further details about LHC can be found in reference [23].

Chapter 3

The CMS Experiment

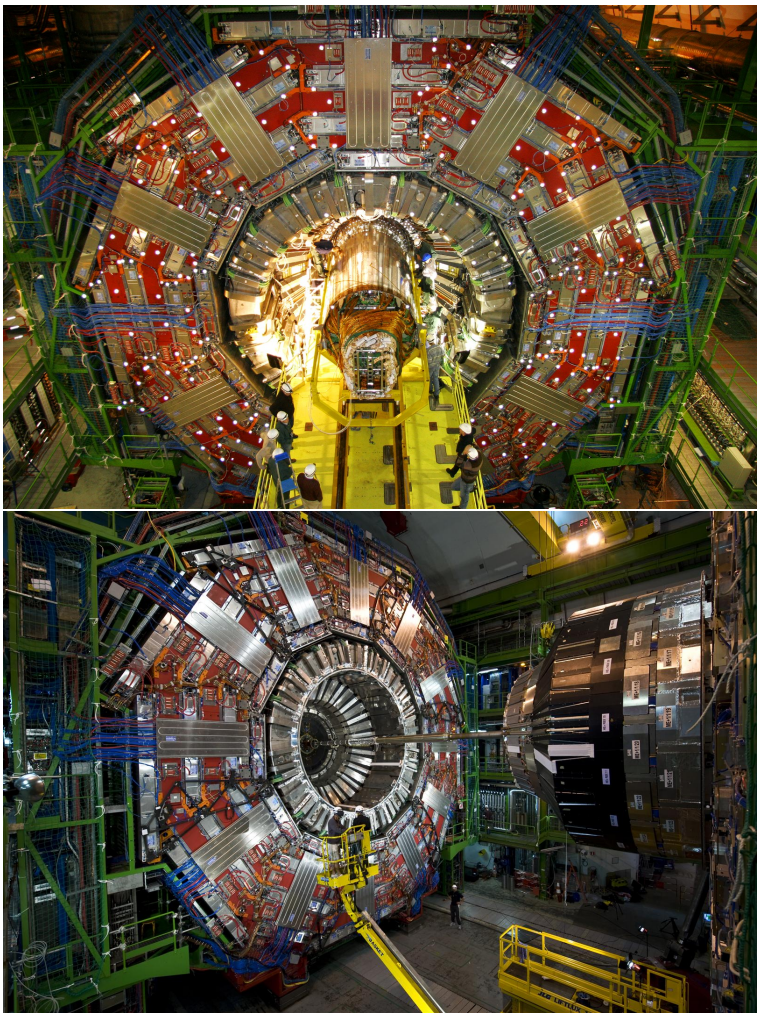

Figure 3.1: Two views of the CMS detector before closing.

As stated before, among the main goals of the LHC machine there is the study of the electroweak symmetry breaking mechanism and the search for physics beyond the Standard Model, to fulfill this goal the most important requirements are:

- good muon identification and momentum resolution over a wide range of momenta in the region $|\eta| < 2.5$. The charge of muons should be determined without ambiguity for momenta up to 1 TeV;
- good dimuon mass resolution (about 1% at 100 GeV);
- good charged particle momentum resolution and reconstruction efficiency in the tracking system together with efficient triggering and offline tagging of tau leptons and b-jets;
- good electromagnetic energy resolution, good diphoton and dielectron mass resolution, measurement of the direction of photons and correct localization of the primary interaction vertex, π_0 rejection and efficient photon and lepton isolation at high luminosities;
- good missing energy and dijet mass resolution, using hadron calorimeters with a large hermetic geometric coverage ($|\eta| < 5$) and with fine lateral segmentation.

The main layout of the CMS detector is shown in figure 3.2. The final design of the detector allows a reliable identification and precise measurement of the muon momentum by means of a redundant muon identification system (tracking system and muon chambers), a precise measurement of photons and electrons energy with a high resolution calorimeter system and an excellent reconstruction of the charged particle tracks and measurement of their momentum resolution thanks to a high quality tracking system. The inner tracking system allows also a precise localisation of the primary vertex of interaction, which is an essential feature in the scenario of high luminosity collisions causing high pileup of events.

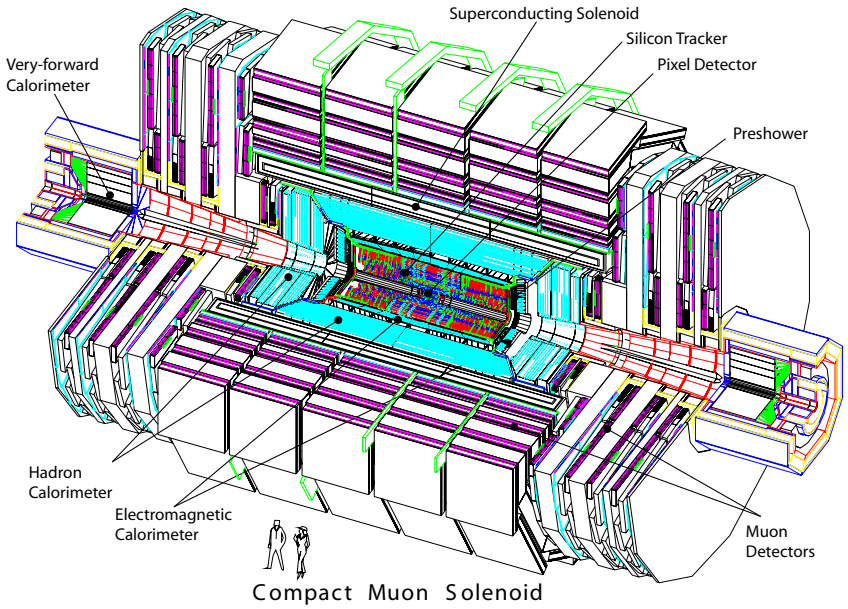

Figure 3.2: CMS detector structure [7].

The detector structure consists of a cylindrical barrel closed by two endcap disks. The overall length is $21.6m$, the diameter $14.6m$ and the total weight about 12500 tons. The thickness of the detector in radiation lengths is greater than $25X_0$ for the electromagnetic calorimeter, and the thickness in interaction lengths varies from 7 to 11 λ_I for the hadronic calorimeter, depending on the η region. For a particle carrying quadrimomentum (E, p_x, p_y, p_z), the momentum vector p can be divided in two components: the longitudinal momentum p_z and the transverse momentum defined as $p_T = \sqrt{{p_x}^2 + {p_y}^2}$. The rapidity is defined as:

$$y = \frac{1}{2} \log \left(\frac{E + p_z}{E - p_z} \right) \tag{3.1}$$

Being invariant under boost of the centre-of-mass along the z direction, the rapidity is used for describing angular distribution of momentum of particles. For an ultra-relativistic particle ($p \gg m$) y can be approximated to the pseudorapidity :

$$\eta = -\log \left(\tan \frac{\theta}{2} \right) \tag{3.2}$$

were θ is the angle between the particle momentum p and the z axis. The specific choice of a solenoid magnetic field led to a very compact design for the CMS system with respect to, for example, the ATLAS design. This allowed the calorimeters to be installed inside the magnet, with a strong improvement in the detection and energy measurement of electrons and photons. In particular the almost constant magnetic field inside the solenoid magnet makes the momentum measurement easier and thus much more precise, with repect to, for example, a non spatially uniform magnetic field. Moreover, tracks exiting the yoke point back to the interaction point, useful for track reconstruction. The downside of this design is that muons passing through the magnet and its return yoke experience multiple scattering effects thus affecting negatively the performance of the muon chambers. The longitudinal view of one quarter of CMS and the transverse view of the barrel region are shown in Figure 3.3.

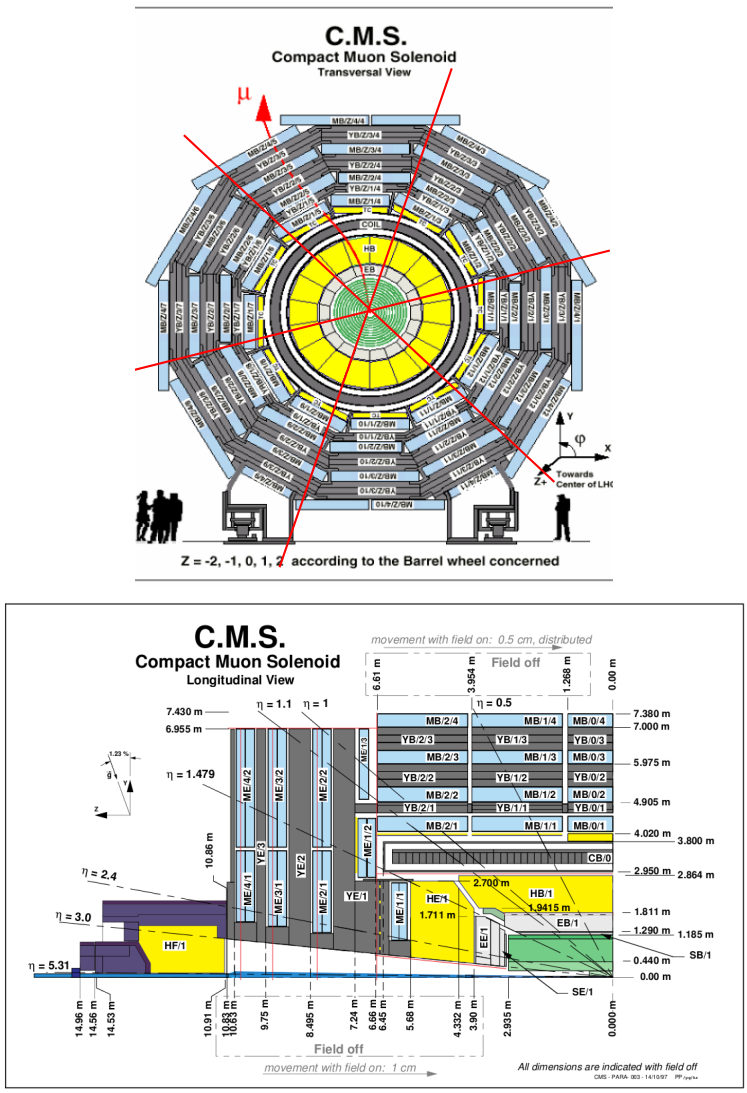

Figure 3.3: Section and side view of the CMS detector [7].

The core of the apparatus is the magnet (CB), a $13m$ long super-conductive solenoid cooled with liquid helium, which provides a $3.8T$ magnetic field. The magnet coil has a diameter of $5.9m$ and contains the Tracker, the electromagnetic and hadronic calorimeters. The iron return yoke of the magnet (YB, YE) hosts the muon spectrometer, composed by 4 stations of drift tube detectors (DT) in the barrel region (MB) and 4 stations of cathode strip chambers (CSC) in the endcaps (ME). Both the barrel and the endcaps are equipped with resistive plate chambers (RPC) which ensure redundancy and robustness at the muon trigger system. The overall pseudorapidity coverage of the muon system goes up to $|\eta| = 2.4$. The hadronic calorimeter (HCAL) is a brass/scintillator sampling calorimeter. The barrel and endcap parts (HB and HE) have the same pseudorapidity coverage as the electromagnetic calorimeter, and are complemented by a very forward calorimeterm(HF), which extends the coverage up to $|\eta| < 5.3$. Inside HCAL, the electromagnetic calorimeter (ECAL) is installed: it is an homogeneous calorimeter made of

lead tungstate ($PbWO_4$) scintillating crystals. The pseudorapidity coverage extends up to $|\eta| < 3.0$. In the endcaps a lead/silicon pre-shower detector is installed to improve the resolution on electron and photon direction and help π rejection.

The tracking detector is placed in the core of CMS: its design was driven by the requirement of a precise vertex reconstruction and a reliable b-tagging with very high track multiplicity. To achieve this goal very fine segmentation is crucial. The choice of CMS was to employ 10 layers of silicon microstrip detectors, which provide the required granularity and precision. In addition, 3 layers of silicon pixel detectors are placed close to the beampipe an the interaction region in order to improve the measurement of the position of primary and secondary vertices. The tracking device allows charged particle tracks reconstruction with at least 12 detector hits and a coverage of $|\eta| < 2.5$.

More detailed technical information on the CMS detector and its subdetectors can be found in [7], [5], [14], [6], [13].

3.1 Tracking System

The tracking system is the core of the CMS detector and it is essential for the reconstruction of the physical object produced by collisions.

In a proton collider the longitudinal momentum of the interacting partons $p_z = p \cdot \cos(\theta)$ is not exactly known for every event (only on a statistical basis), and the measurement of the physics observables is thus usually performed in the transverse plane.

In a proton collider the momentum of interacting partons is not exactly known for every event (only their mean on a statistical basis), moreover the longitudinal momentum of the interaction products is tipically hard to measure.

Therefore, it becomes essential to measure the transverse momentum $p_T = p \cdot \sin(\theta)$ with a very high resolution. The trajectory of a particle with transverse momentum p_T and charge $Q = ze$ inside a magnetic field B is an helix, with radius R. The relation among these quantities is:

$$p_T = 0.3 \cdot z \cdot B \cdot R \tag{3.3}$$

where p_T is expressed in GeV, B in T e R in m. What is experimentally measured is the radius R, or better, the curvature $k = Q/R$. The distribution of the measurements is gaussian, and the error can be written as the sum in quadrature of two contributions, the resolution on the measurement (δk_{res}) and the multiple Coulomb scattering (δk_{ms}):

$$\delta k = \sqrt{\delta k_{res}^2 + \delta k_{ms}^2} \tag{3.4}$$

Parametrizing the formula in terms of p_T, the particle transverse momentum resolution can be written as:

$$\frac{\delta p_T}{p_T} = C_1 p_T \oplus C_2 \tag{3.5}$$

where the term C_2 contains the multiple Coulomb scattering effects, while the angular coefficient C_1 depends on the detector geometry, in particular from the number of points used for the track reconstruction (n), its length (L), and the resolution on the single point measurement (σ_x):

$$C_1 \propto \frac{\sigma_x}{\sqrt{n} \cdot B \cdot L^2} \tag{3.6}$$

For low energetic particles C_2 dominates. C_1 is minimized having a long Tracker detector, and a consistent number of points n in the track fit. The resolution σ_x on a single measured point is given by:

$$\sigma_x = \sqrt{\sigma_{int}^2 + \sigma_{syst}^2} \tag{3.7}$$

where σ_{int} is the intrinsic resolution of the detectors and σ_{syst} the systematic error given by the unknown spatial position of hit module: this last one can be minimized by alignment procedures.

The major requirements for the CMS Tracker can be summarized in the:

- promptness in the response, given the high track population during the nominal LHC collisions of one (plus pile-up) event every $25ns$;
- robustness of its components to the radiation exposure, given the high density of hadronic tracks up to $10^{14} n_e q \cdot cm^{-2}$, where $n_e q$ are "equivalent" $1MeV$ neutrons;
- minimization of the crossed material, with the aim of reducing the multiple Coulomb scattering of charged particles crossing the detector, photon conversion and electron energy loss via Bremsstrahlung;
- perfect alignment, internal of its components and with the muon system, in order to provide a reliable measurement of the particle momentum.

The CMS Tracker detector was designed in order to fulfill these requirements, giving at its nominal performance:

- reconstruction capability in the region $|\eta| < 2.5$ with an efficiency of at least 95% for charged tracks with $p_T > 10GeV$;
- high momentum resolution for isolated tracks:

$$\frac{\delta p_T}{p_T} = (1.5 \cdot p_T \oplus 0.5)\% for |\eta| < 1.6 \tag{3.8}$$

$$\frac{\delta p_T}{p_T} = (6.0 \cdot p_T \oplus 0.5)\% for |\eta| < 2.5 \tag{3.9}$$

  where the p_T is expressed in TeV. As shown in Figure 3.4 adding the information from the muon system, the resolution, for $p_T > 0.1TeV$ muons, becomes:

$$\frac{\delta p_T}{p_T} = (4.5\% \cdot \sqrt{p_T}) \tag{3.10}$$

- high resolution for transverse impact parameter, $\sigma(d_{xy}) = 35\mu m$ and longitudinal impact parameter $\sigma(d_z) = 75\mu m$.

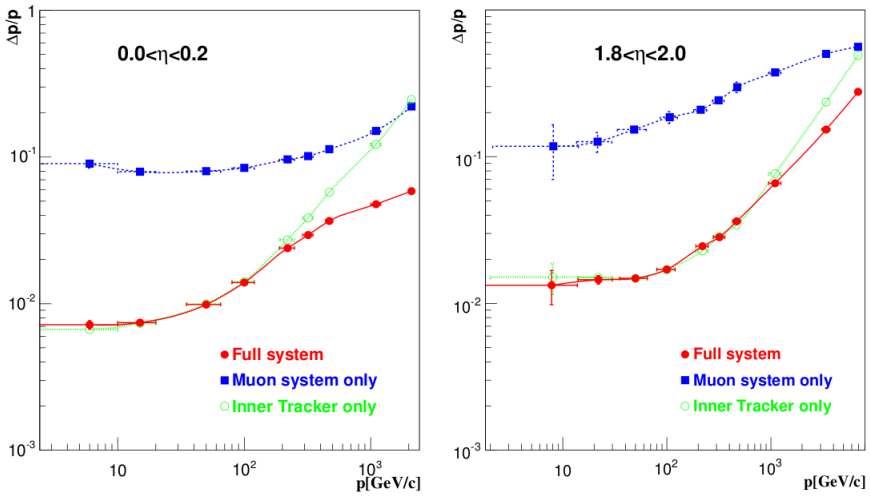

Figure 3.4: Expected momentum resolution of muons as a function of momentum p, using measurements of the muon system only (blue), the Tracker only (green) or both detectors (red). Left. Central region $0 < \eta < 0.2$. Right. Forward endcap region $1.8 < \eta < 2.0$ [7].

The CMS collaboration decided to build the whole detector using a silicon detector technology. This type of detector provides a narrow spatial resolution, from $10\mu m$ to $20\mu m$ and a fast collection of the charge deposited on the sensible elements, below $10ns$. The Tracker covers the pseudorapidity region $|\eta| < 2.5$ with a radius ranging between $4.3cm$ and $120cm$ in the z interval between $-270cm$ and $270cm$. The innermost region is made of pixel detectors, while the outermost one is built with strip detectors.

3.1.1 The Pixel Detector

The pixel Tracker consists of three $53.3cm$ long barrel layers and two endcap disks on each side of the barrel section, as shown in 3.5. The innermost barrel layer has a radius of $4.4cm$, while for the second and third layer the radii are $7.3cm$ and $10.2cm$, respectively. The layers are composed of modular detector units (called modules) placed on carbon fiber supports (called ladders). Each ladder includes eight modules, consisting of thin ($285\mu m$), segmented silicon sensors with highly integrated readout chips (ROC) connected by Indium bump-bonds. Each ROC serves a 52×80 array of $150\mu m \times 100\mu m$ pixels. The Barrel Pixel (BPIX) region is composed of 672 full modules and 96 half modules, each including 16 and 8 ROCs, respectively. The number of pixels per module is 66560 (full modules) or 33280 (half modules). The total number of pixels in the barrel section is 47923200.

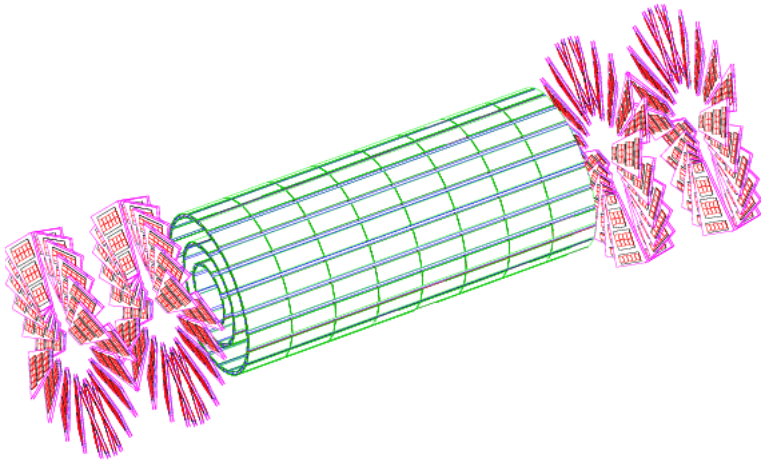

Figure 3.5: Schematic illustration of the pixel tracker. [7]

The Forward Pixel (FPIX) endcap disks, extending from $6cm$ to $15cm$ in radius, are placed at $z = \pm 35.5cm$ and $z = \pm 48.5cm$. Disks are split into half-disks, each including 12 trapezoidal blades arranged in a turbine-like geometry. Each blade is a sandwich of two back-to-back panels. Rectangular sensors of five sizes are bump-bonded to arrays of ROCs, forming the so-called plaquettes. Three (four) plaquettes are arranged on the front (back) panels with overlap to provide full coverage for charged particles originating from the interaction point. The endcap disks include 672 plaquettes ($270\mu m$ thick), for a total of 17971200 pixels. The minimal pixel cell area is dictated by the readout circuit surface required for each pixel. In localizing secondary decay vertices both transverse ($r\phi$) and longitudinal (z) coordinates are important and a nearly square pixel shape is adopted. Since the deposited charge is often shared among several pixels, an analog charge readout is implemented. Charge sharing enables interpolation between pixels, which improves the spatial resolution. In the barrel section, the charge sharing in the $r\phi$-direction is largely due to the Lorentz effect. In the endcap pixels, the sharing is enhanced by arranging the blades in the turbine-like layout.

3.1.2 The Strip Detector

Outside the pixel detector, the Tracker (see Figure 3.6) is composed of 10 layers of silicon microstrip detectors. The barrel region ($|\eta| < 1.6$) is divided into two parts: the Tracker Inner Barrel (TIB), covering $20 < r < 60cm$ and the Tracker Outer Barrel (TOB), covering $60 < r < 120cm$. The TIB is composed by four layers of p-on-n type silicon sensors with a thickness of $320\mu m$ and strip pitches varying from $80\mu m$ to $120\mu m$. The first two layers are made with double sided modules, composed by two detectors mounted back to back with the strips tilted by $100mrad$. This kind of sensors provides a measurement in both $r\phi$ and $r - z$ coordinates with a single point resolution between $23 - 34\mu m$ and $230\mu m$ respectively. The TOB is made of six layers. In this region the radiation levels are smaller and thicker silicon sensors ($500\mu m$) can be used to maintain a good signal-to-noise ratio for longer strip length. The strip pitch varies from $120\mu m$ to $180\mu m$. Also the first two layers of the TOB provide a stereo measurement with a single point resolution which varies from $35\mu m$ to $52\mu m$ in the r direction and $530\mu m$ in z. The

endcap region ($|\eta| > 1.6$) is covered by the Tracker Inner Disks (TID) and Tracker End Cap (TEC). The three disks of the TID fill the gap between the TIB and the TEC while the TEC comprises nine disks that extend into the region $120cm < |z| < 280cm$. Both subdetectors are composed of wedge shaped modules arranged in rings, centred on the beam line, and have strips that point towards the beam line (radial topology).

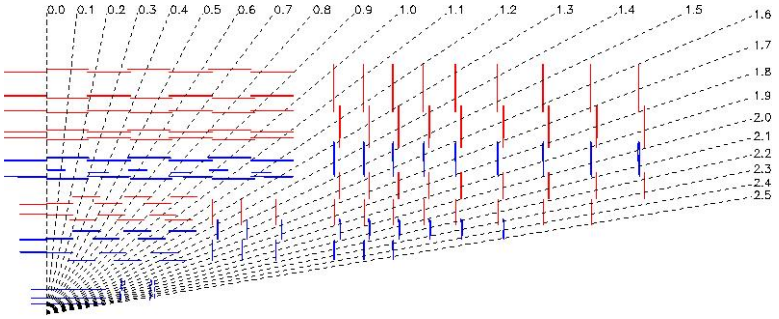

Figure 3.6: Schematic view of the strip tracker. [7]

3.2 Electromagnetic Calorimeter

The goal of the electromagnetic calorimeter is the accurate measurement of the energy and position of electrons and photons. The physics process that imposes the strictest requirements on its performance is the low mass ($mH \simeq 120 - 140GeV$) Higgs decay into two photons $H \to \gamma\gamma$. The goal is 1% resolution on the diphoton invariant mass. The natural choice to achieve this task is a homogeneous calorimeter.

The ECAL is composed of 75,848 finely segmented lead tungstate ($PbWO_4$) crystals chosen because of their excellent energy resolution. Lead tungstate is a fast, radiation-hard scintillator characterised by a small Moliere radius ($R_M = 1.9mm$) e and a short radiation length ($X_0 = 8.9mm$), that allows good shower containment in the limited space available for the detector. Moreover, these crystals are characterised by a very short scintillation decay time that allows the electronics to collect about 80% of the light within $25ns$. A pre-shower detector is installed in front of the endcaps, consisting of two lead radiators and two planes of silicon strip detectors, with a total radiation length of $3X_0$. It allows rejection of photon pairs from π_0 decays and improve the estimation of the direction of photons, to improve the measurement of the two-photon invariant mass. The geometric coverage of the calorimeter extends up to $|\eta| = 3.0$, as shown in 3.7. The crystals are arranged in a $\eta - \phi$ grid in the barrel and a $x - y$ grid in the endcaps and they are almost pointing to the interaction point: the axes are tilted a 3° in the barrel and at $2° - 5°$ in the endcaps with respect to the line from the nominal vertex position.

Contribution	Barrel($\eta = 0$)	Endcap($\eta = 2$)
Stochastic term a	2.7%	5.7%
Noise (low luminosity) b	$0.155GeV$	$0.205GeV$
Noise (high luminosity)	$0.210GeV$	$0.245GeV$
Constant term c	0.55%	0.55%

Table 3.1: Different contributions to the energy resolution of ECAL

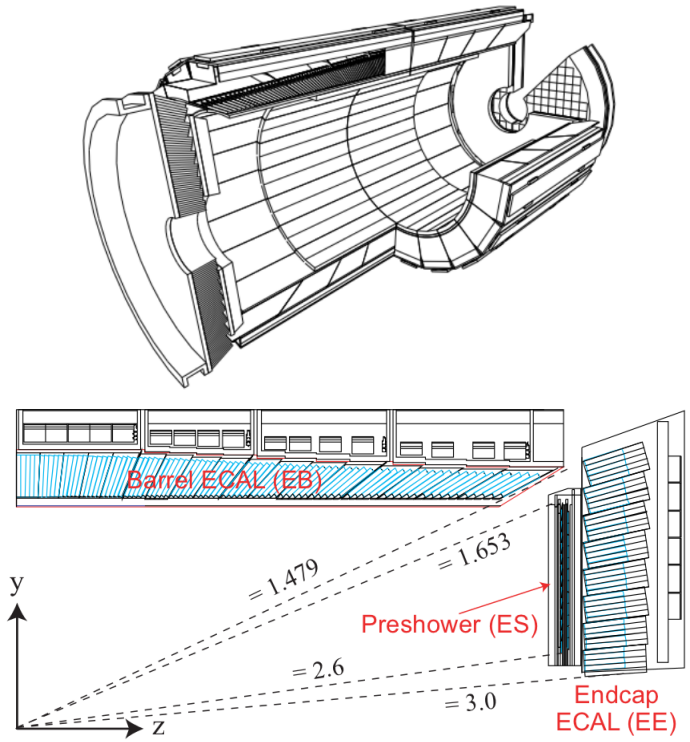

Figure 3.7: Schematic view of the Electromagnetic Calorimeter [7]

The energy resolution of a calorimeter is usually parameterized as:

$$\left(\frac{\sigma_E}{E}\right)^2 = \left(\frac{a}{\sqrt{E}}\right)^2 + \left(\frac{b}{E}\right)^2 + c^2 \tag{3.11}$$

where a is the stochastic term and it includes the effects of fluctuations in the number of photo-electrons as well as in the shower containment, b is the noise from the electronics and pile-up and c is a constant term related to the calibration of the calorimeter. The values of the three constants measured on test beams are reported in Table 3.1. The different contributions as a function of the energy are shown in Figure 3.8.

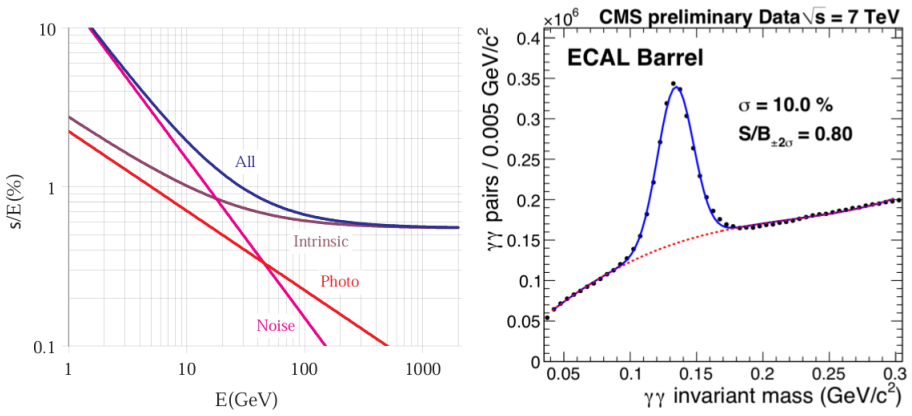

Figure 3.8: Left: Different contributions to the energy resolution of the ECAL. Right: diphoton invariant mass spectrum reconstructed by ECAL with about $250nb^{-1}$ of data at. The π_0 peak is visible, the mass resolution is of the order of 10% [7].

3.3 Hadron Calorimeter

The goal of the hadron calorimeter is to measure the direction and energy of hadronic jets, the total transverse energy and the missing transverse energy (MET) of the event. High hermeticity is required for this purpose, which means the subdetector must cover a portion of the solid angle as big as possible. For this reason, the barrel and endcap parts installed inside the magnet are complemented by a very forward calorimeter which is placed outside the magnet return yokes, with a total coverage of $|\eta| < 5.3$. The barrel and endcap HCAL cover the region $|\eta| < 3.0$. They are sampling calorimeters, whose active elements are plastic scintillators interleaved with brass absorber plates and read out by wavelength-shifting fibres. The first layer is read out separately, while all others are read out together. The absorber material has been chosen for its short interaction length, and its non-magnetic property. Both barrel and endcap are read-out in towers with a size of $\Delta\eta \times \Delta\phi$.

In the barrel, full shower containment is not possible within the magnet volume, and an additional tail catcher is placed outside the magnet consisting of an additional layer of scintillators. The projective depth in terms of nuclear absorption length goes from $5.1\lambda_I$ at $\eta = 0$ to $9.1\lambda_I$ at $\eta = 1.3$ and $10.5\lambda_I$ in the endcap. The very forward calorimeter is placed outside the magnet yoke, $11m$ from the interaction point. The active elements are quartz fibres parallel to the beam, inserted in steel absorber plates. The signal originated from quartz fibres is Cerenkov light.

The expected energy resolution (E in GeV) is $\sigma/E \simeq 65\%\sqrt{E} \oplus 5\%$ in the barrel, $\sigma/E \simeq 85\%\sqrt{E} \oplus 5\%$ in the endcaps and $\sigma/E \simeq 100\%\sqrt{E} \oplus 5\%$ in the very forward calorimeter.

3.4 Magnet and Muon Detection System

3.4.1 The Superconducting Magnet

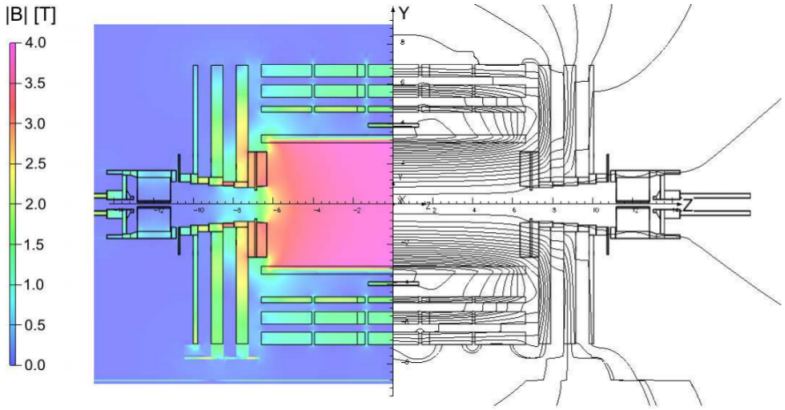

Figure 3.9: The CMS magnet and the generated magnetic field [7]

The CMS magnet is a $13m$ long superconducting solenoid, the largest ever built. It is able to generate a uniform magnetic field of $4T$ in the inner region, storing about $2.5GJ$ of energy. It operates at a temperature of $4K$, ensured by a sophisticated helium cooling system. At such temperatures, the flat $NiTb$ cable becomes superconducting, allowing a $20kA$ current to flow without appreciable loss.

The whole magnet is contained in a enormous vacuum cylinder, which isolates it from the external environment. Outside, an iron structure composed by five barrel layers and three disks for each endcap constitutes the iron yoke, needed to guide the return magnetic field, which would get lost otherwise, causing interferences. The CMS magnet provides a huge bending power, allowing a precise measurement of the transverse momentum of charged particles inside the solenoid, operated by the inner tracking system. A further and independent p_T measurement outside the solenoid is possible thanks to the iron yoke, which surrounds the muon chambers.

3.4.2 The Muon System

Muons provide a clear signature for many physics processes. For this reason, the muon spectrometer must provide a robust trigger and an accurate measurement of the muon momentum and charge, also without the contribution of the Tracker. The muon system, shown in 3.10, is embedded in the iron return yoke of the magnet, which shields the detectors from charged particles other than muons. The minimum value of the muon transverse momentum required to reach the system is $\simeq 5GeV$. The muon spectrometer consists of three independent subsystems.

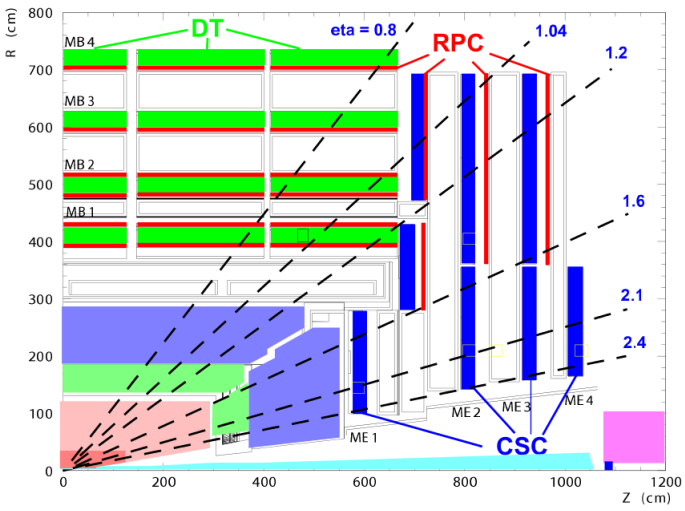

Figure 3.10: Schematic view of the Muon system. [7]

In the barrel ($|\eta| < 1.2$), where the track density and the residual magnetic field are low, four layers (stations) of drift tube chambers (DT) are installed. The chamber segmentation follows that of the iron yoke, consisting of five wheels along the z axis, each one divided into 12 azimuthal sectors. Each chamber has a resolution of about $100\mu m$ in $r\phi$ and $1mrad$ in ϕ.

In the endcaps ($0.8 < |\eta| < 2.4$), four disks (stations) of cathode strip chambers (CSC) are located, being this detector technology more indicated in a region suffering high particle rates and large residual magnetic field between the plates of the yoke. The rings are formed by 18 or 36 trapezoidal chambers, which are stacked with a small overlap in ϕ. These chambers have a spatial resolution of about $200m$ ($100m$ for the chambers belonging to the first station) and $10mrad$ in $r - \phi$. Redundancy is obtained with a system of resistive plate chambers (RPC), that are installed in both the barrel and the endcaps. RPCs have limited spatial resolution, but fast response and excellent time resolution of few ns, providing unambiguous bunch crossing identification. RPC detectors operate in avalanche mode, thus allowing the detectors to sustain higher rates. This mode is obtained with a lower electric field, thus the gas multiplication is reduced and an improved electronic amplification is required. In the barrel the RPC chambers follow the segmentation of DT chambers. A total of six layers of RPCs are present. In the endcaps the chambers are trapezoidal distributed on four disks. They are also used to complement DTs and CSCs in the measurement of p_T. The RPC system covers the region $|\eta| < 2.1$. The robustness of the spectrometer is also guaranteed by the different sensitivity of DT, RPC and CSC to the background. The main sources of background particles in the LHC environment will be represented by secondary muons produced in pion and kaon decays, from punch-through hadrons and from low energy electrons originating after slow neutron capture by nuclei with subsequent photon emission. This neutron induced background will be the responsible of the major contribution to the occupancy level in the muon detectors. CSC and DT chambers, in contrast with RPC detectors, are characterised by a layer layout which helps in reducing the effect of background hits: the request of correlation between consecutive layers is particularly effective against background hits

affecting only a single layer.

3.5 Trigger System and Data Acquisition

The huge amount of data produced due to the high interaction rate produced at LHC cannot be sustained by any storage system presently available. Given the typical size of a raw event ($1MB$), only a rate of $\approx 100Hz$ can be stored for offline analysis, when the collisions rate is in fact $40MHz$. A huge reduction factor is thus necessary: it is accomplished by the trigger and the data acquisition systems.

3.5.1 The Trigger System

The event rate is mainly composed of protons interactions with particles of low transverse momentum. A good triggering system should have a large rejection of the less interesting particles and maintain at the same time a high efficiency on the (potential) interesting events. This characteristic is achieved at CMS in two steps: a Level 1 Trigger (L1) and a High Level Trigger (HLT). The rate reduction capability is designed to be a factor of 107 for the combined L1 and HLT.

3.5.2 The Level 1 Trigger

The Level 1 Trigger consists of custom-designed, largely programmable electronics: it reduces the rate of selected events down to $100kHz$ for the high luminosity runs. The full data are stored in pipelines of processing elements, while waiting for the trigger decision. The maximum latency allowed is $3.2\mu s$: if the L1 accepts the event, the data are moved to be processed by the High Level Trigger. The high bunch crossing rate does not permit the full readout of the detector, mainly because of the slowness of the tracker algorithms: only the calorimetric and muons information are employed. The Calorimeter Trigger identifies the best four candidates of each of the following classes: electrons and photons, central jets, forward jets and so on identified from the shape of the deposited energy. The information of these objects is passed to the Global Trigger, together with the measured missing E_T . The Muon trigger is performed separately for each muon detector. The information is then merged and the best four muon candidates are transferred to the Global Trigger. The Global Trigger takes the decision to reject an event or to accept the event for further evaluation by the HLT. The decision is based on algorithm calculations and on the readiness of the sub-detectors and the DAQ. The L1 Trigger electronics is housed partly on the detectors, partly in the underground control room located at a distance of approximately $20m$ from the CMS detector site.

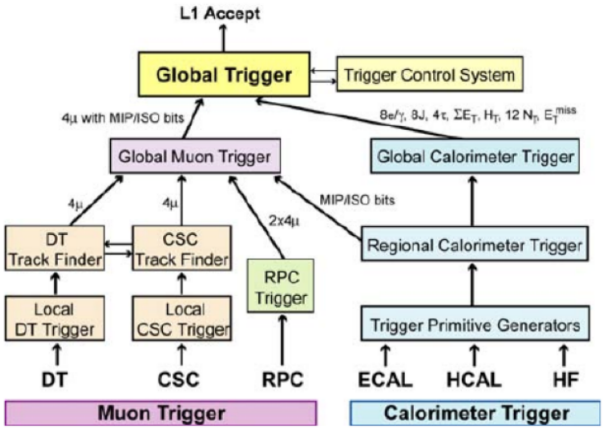

Figure 3.11: Scheme of the L1 trigger. [7]

3.5.3 The High Level Trigger (HLT)

HLT is a software system (implemented in a filter farm of about one thousand commercial processors) which reduces the output rate down to around 100 Hz. The idea of the HLT trigger software is the regional reconstruction on demand: only objects in the useful regions are reconstructed and uninteresting events are rejected as soon as possible. The HLT has access to the high-resolution data in pipelined memories in the front-end electronics as well as the information from the silicon tracker: it can therefore perform complex calculations. The L1 and HLT schema lead to the development of three "virtual trigger" levels: at the first level only the full information of the muon system and of the calorimeters is used, in the second level the information of the tracker pixels is added and in the third and final level the full event information is available.

3.5.4 The Data Acquisition (DAQ)

The CMS Data Acquisition (DAQ) [32] has the task to transport the data from about 650 data sources at the detector side, to the filter units for processing of complete events. Each data source provides event fragments of about $2kB$. The central DAQ runs online software on about 3000 PC used for buffering and processing of event data. The DAQ system of CMS is shown in 3.12. The detector is read out through a builder network with a bandwidth of $100GB/s$ by the so called Front-End Drivers (FED). The FEDs are located in the underground counting room $\sim 70m$ from the detector. Complete events are fed to the event filter systems at a rate of maximal $100kHz$. The large rate to the filter systems stems from the design choice of CMS to build the full event already after the first level trigger instead of building partial events as in traditional multi level trigger systems. This requires the read-out, assembly and forwarding of the full event data at the nominal level one trigger rate. The total rate of data produced by the online trigger system is $\sim 230MB/s$. These data need to be stored for further processing and analysis.

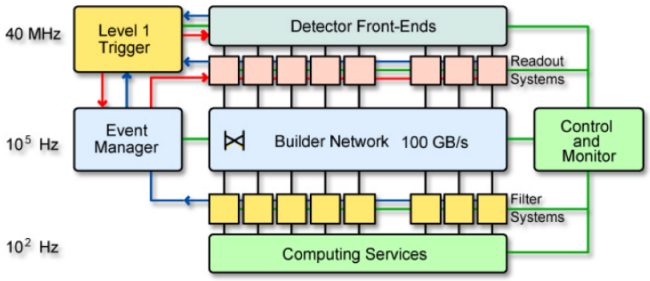

Figure 3.12: Scheme of the DAQ system. [7]

3.6 Software Framework and Computational Challenge

The CMS experiment poses new challenges not only in terms of the physics to discover and the detector to build and operate, but also in terms of the data volume and the necessary computing resources. Datasets and resource requirements are at least an order of magnitude larger than in previous LEP experiments.

CMS computing and storage requirements is, with present technology, impossible to fulfil in only one place, for both technical and funding reasons. Therefore, the CMS computing environment has been constructed as a distributed system of computing services and resources that interact and cooperate with each other, as Grid services. The set of services and computing resources are used for storage, connectivity resources, data processing, data archiving, Monte Carlo event generation and all kinds of computing-related activities.

Grid computing aims to provide reliable and secure access to widely scattered resources for authorized users located virtually anywhere in the world. When a user submits a job, the Grid software controls where the job gets sent for processing.

A 3-level Tier structure of computing resources has been organized to handle the vast storage and computational requirements of the CMS experiment. A CMS physicist may use Grid tools to submit a CMS analysis job to a "Workload Management System" (WMS), and does not need to worry about the details such as location of data and available computing power, which are handled transparently.

The CMS Grid system is part of the larger Worldwide LHC Computing Grid Project (WLCG). The mission of the WLHC Computing Project (WLCG) is to build and maintain a data storage and analysis infrastructure for the entire high energy physics community that will use the LHC. The WLCG project aims to collaborate and interoperate with other major Grid development projects and production environments around the world. As such, WLCG has developed relationships with regional computing centres as T1 centres. These centres exist in a number of different countries in Europe, North America and Asia.

As stated just above, the computing centres available to CMS through the Grid system around the world are distributed and configured in a "tier" architecture. Each of the three tier levels provides different resources and services:

- Tier-0, the first tier in the CMS model, for which there is only one site, CERN.

Among its tasks there are: accept, archive and distribute RAW data collected from the CMS Online Data Acquisition and Trigger System (TriDAS), perform Prompt calibration in order to get the calibration constants needed to run the reconstruction, perform prompt first pass reconstruction which writes the RECO and Analysis Object Data (AOD) extraction, transfer Prompt reconstructed RECO and AOD datasets to Tier-1.

- Tier-1: there is a set of seven Tier-1 (T1) sites, which are large centers in CMS collaborating countries (large national labs o research institutes, e.g. INFN, and FNAL) Among its tasks there are: archive and redistribute to Tier-2 RAW, RECO, AOD and MC samples,

- Tier-2: this is a more numerous set of smaller centres, but with substantial CPU resources, providing capacity for user analysis, calibration studies, and Monte Carlo production. Tier-2 provide limited disk space, and no tape archiving. T2 centers rely upon T1s for access to large datasets and for secure storage of the new data (i.e. Montecarlo simulations) produced at the T2.

CMS Data is arranged into a hierarchy of data tiers. Each physics event is written into each data tier, where the tiers each contain different levels of information about the event. The three main data tiers used in CMS are:

- RAW: full event information from the Tier-0 (i.e. from CERN), containing 'raw' detector information (detector element hits, detailed trigger information, various electronic info). Not used directly for analysis.

- RECO ("RECOnstructed data"): the output from first-pass processing by the Tier-0. This layer contains reconstructed physics objects and part of RAW info, thus it's still very detailed and may slow down analysis when CMS has collected a substantial data sample.

  The event reconstruction step from RAW to RECO is structured in several hierarchical steps:

  1. Detector-specific processing: Starting from detector data unpacking and decoding, detector calibration constants are applied and cluster or hit objects are reconstructed.
  2. Tracking: Hits in the silicon and muon detectors are used to reconstruct global tracks. Pattern recognition in the tracker is the most CPU-intensive task.
  3. Vertexing: Reconstructs primary and secondary vertex candidates.
  4. Particle identification: Produces the objects most associated with physics analyses. Using a wide variety of sophisticated algorithms, standard physics object candidates are created (electrons, photons, muons, missing transverse energy and jets; heavy-quarks, tau decay).

  The normal completion of the reconstruction task will result in a full set of these reconstructed objects usable in physics analyses. Reconstruction is expensive in terms of CPU and is dominated by tracking.

- AOD ("Analysis Object Data"): this is a "distilled" version of the RECO event information, and is expected to be used for most analyses. AOD provides a compromise between event size and complexity of the available information to optimize flexibility and speed for analyses, most of the raw information of the detector are lost at this point.

The overall collection of software used in CMS is referred to as CMSSW, it is built around a Framework, an Event Data Model (EDM), and Services needed by the simulation, calibration and alignment, and reconstruction modules that process event data so that analysis can be performed. The primary goal of the Framework and EDM is to facilitate the development and deployment of reconstruction and analysis software.

The CMSSW event processing model consists of one executable, called cmsRun, and many plug-in modules which are managed by the Framework. All the code needed in the event processing (calibration, reconstruction algorithms, etc.) is contained in the modules. The same executable is used for both detector and Monte Carlo data.

The CMSSW executable, cmsRun, is configured at run time by the user's job-specific configuration file. This file tells cmsRun

- which data to use
- which modules to execute
- which parameter settings to use for each module
- what is the order or the executions of modules, called path
- how the events are filtered within each path and how the paths are connected to the output files

The CMS Event Data Model (EDM) is centered around the concept of an Event. An Event is a C++ object container for all RAW and reconstructed data related to a particular collision. During processing, data are passed from one module to the next via the Event, and are accessed only through the Event. All objects in the Event may be individually or collectively stored in ROOT files, and are thus directly browsable in ROOT.

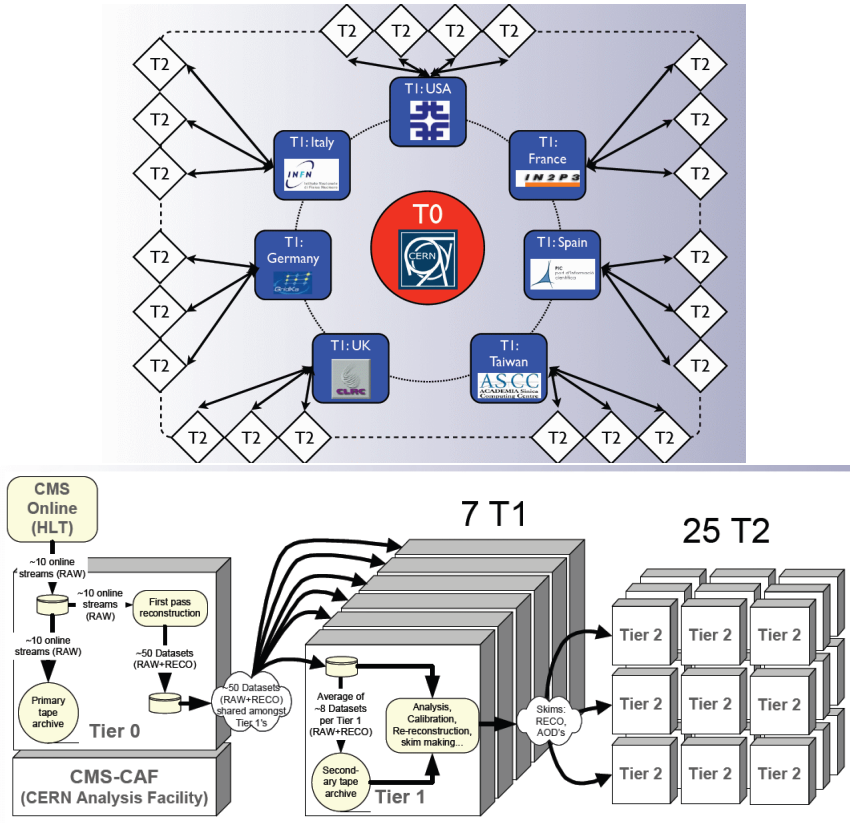

Figure 3.13: Schematic representation of the CMS Grid storage tier structure and the associated data workflow [7]

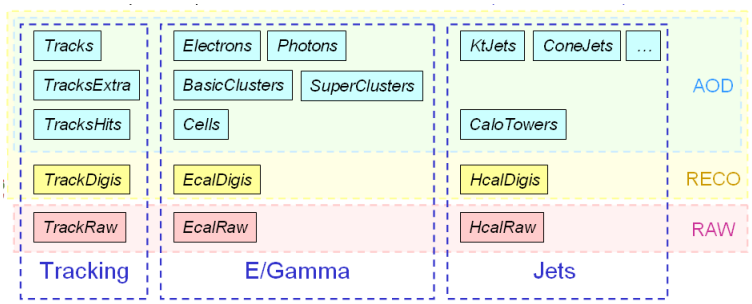

Figure 3.14: Schematic representation and comparison of the CMS Data tiers content [7]

Given the large data volumes involved and the large size of the CMS collaboration, a fully distributed computing model is used for data reconstruction and analysis. The system is based upon Grid middleware, with the common Grid services at centres defined and managed through the Worldwide LHC Computing Grid (WLCG) project, a collaboration between LHC experiments, computing centres, and middleware providers.

Chapter 4

Data Analysis

This analysis has two main goals, the first -developed in this chapter- is to evaluate production cross-section ratio of $\chi_b(2P)$ over $\chi_b(1P)$ inclusively of all angular momentum eigenstate for each nP state. The second goal -developed in next chapter- is to measure the barycenter of mass of the recently discovered 3P state. At the time of the writing there is no public experimental result for the first measurement, while for the second the first public result appeared in late December 2011 published by the ATLAS collaboration [25].

This work consider only J=1 and J=2 spin state for each nP state, χ_b spin 0 states are not considered in this work due to their very low branching ratio in $\Upsilon + \gamma$ with respect to others spin states, therefore give a negligible constribution(e.g. for 1P: $\frac{BR(j=0)<6\%}{BR(j=1)\simeq 35\%}$), moreover J=1 and J=2 states of the same nP triplet cannot be clearly separated due to the resolution being greater than their energy separation.

4.1 Experimental method

χ_b states masses are reconstructed through the decay chain $\chi_b \to \Upsilon(1S)+\gamma$ and $\Upsilon(1S) \to \mu^+ + \mu^-$. The main difficulty reconstructing such a decay in CMS is the photon detection -which has relatively low energy- with a good resolution. In the center of mass of χ_b states photon has 432 MeV and 795 MeV decaying from $\chi_b(1P_1)$ and $\chi_b(2P_1)$ respectively. The standard CMS subdetector designated to photon detection is the Electromagnetic Calorimeter (ECAL) which, however, would give a rather poor resolution (O $\sim$ 50 MeV) when recostructing photons from $\chi_b's$ decay.

The strategy is, therefore, to search for photons which, through pair-production, converted in the beam-pipe or the inner layers of CMS silicon tracker and reconstruct the tracks left by the electron-positron pair inside the tracker. This tecnique not only allows for a better energy resolution (O $\sim$ 15 MeV) than the one that would be obtained using ECAL, but it also gives a very accurate spatial resolution of the photon which allows to distinguish the Primary Vertex the photon come from: essential feature in events with multiple p-p collisions (pileup).

The drawback of such strategy is the reduced yield of reconstructed events. Two factors limit the yield of events: the probability that a photon converts in the tracker and, most important, the difficulty to reconstruct low transverse momentum (p_T) pairs. Since the standard CMS algorithm is not optimized to reconstruct such low energy conversion a new one was developed for this kind of analysis.

In order to cancel the di-muon invariant mass resolution uncertainty, the difference between $\mu\mu\gamma$ and $\mu\mu$ invariant masses is used (Q value). The experimental method consist in applying a maximum likelihood fit to Q value and extract the number of candidates χ_b for each nP multiplet and also the mass of the 3P state.

To evaluate the production cross-section ratio of 2P over 1P state it is necessary to calculate the total reconstruction efficiency for each of the states. The result is thus obtained with the formula:

$$\frac{\sigma(pp \to \chi_b(2P))}{\sigma(pp \to \chi_b(1P))} = \frac{N_{\chi_b(2P)}}{N_{\chi_b(1P)}} \cdot \frac{\epsilon_1}{\epsilon_2} \cdot \frac{BR(\chi_b(1P) \to \Upsilon(1S)\gamma)}{BR(\chi_b(2P) \to \Upsilon(1S)\gamma)} \tag{4.1}$$

where $N_{\chi_b(nP)}$ is the number of candidates of each type obtained from the fit, $\frac{\epsilon_1}{\epsilon_2}$ is the efficiency correction derived from a full detector simulation and BR are the branching ratios obtained from PDG tables.

4.2 Event reconstruction and selection

4.2.1 Dataset

The whole amount of data acquired by LHC in the 2011 run has been taken into account in this analysis. The 2011 LHC run is subdivided in two periods: 2011A and 2011B, the latter is characterized by higher instantaneous luminosity and larger number of interactions per bunch crossing. The data was collected using High Level Trigger (HLT) paths specifically optimized to collect events containing $\Upsilon \to \mu^+ + \mu^-$. Those trigger paths are called

`HLT_DimuonX_Upsilon_Barrel`

where X stands for the minimum p_T of the dimuon. The p_T threshold was continuosly raised throughout the year: it increased from initial 5 GeV to 7GeV and finally to 9GeV, each increase was imposed when the instantaneous luminosity exceeded 1 $nb^{-1}s^{-1}$, 3 $nb^{-1}s^{-1}$ and 5 $nb^{-1}s^{-1}$ respectively. Since LHC continuosly delivered increasing luminosity throughout 2011 raising p_T threshold in trigger menus allowed to keep roughly constant the data saving rate while keeping data quality constant.

Figure 4.1 shows the dimuon data collected with the triggers used between 13-03-2011 and 03-05-2011 which must be compared to the more restrictive requirements of the triggers used to collect data shown in figure 4.2 used between 16-06-2011 and 28-06-2011. Must also be noted that the quantity of dimuon reconstructed with the triggers menu refering to figure 4.1 are roughly the same obtained with the triggers used in figure 4.2, despite the former run lasted for a much longer period than the latter.

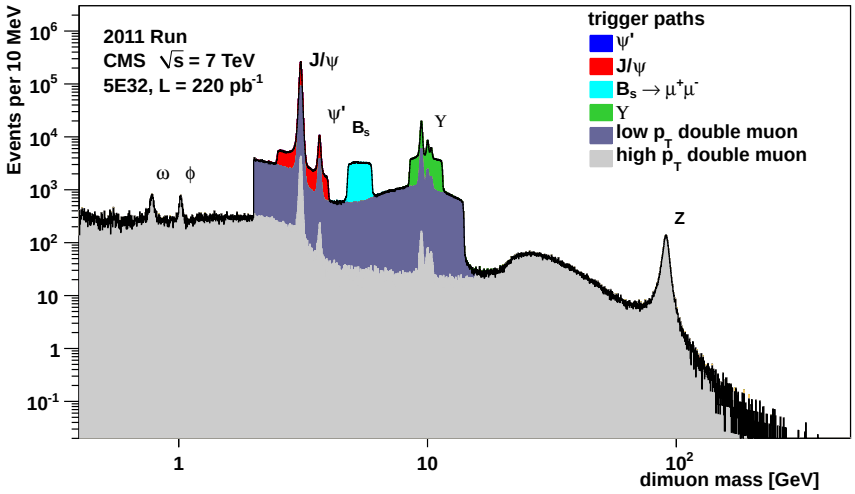

Figure 4.1: Dimuon mass spectrum with trigger menu used between 13/03 and 03/05 2011

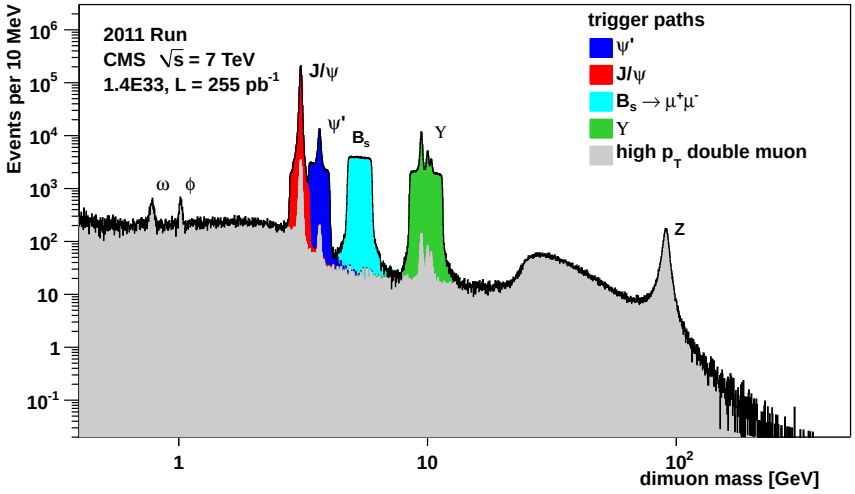

Figure 4.2: Dimuon mass spectrum with trigger menu used between 16/06 and 28/06 2011

The trigger requires the dimuon candidate to satisfy some requirements: the two muons must have opposite-sign charge, dimuon must have rapidity inside the barrel region $|y| < 1.25$, the two muon trajectories are fitted with a common vertex constraint and the events are retained if the fit χ^2 probability is larger than 0.5%, finally, the events are stored only if the dimuon mass is within the window 8.5–11.5 GeV.

4.2.2 $\Upsilon(1S)$ reconstruction

$\Upsilon(1S)$ candidates are reconstructed using a standard CMS tool: the $Onia2MuMu$ module. The module is extensively used in most Quarkonia and B-physics anlysis. In order to describe the parameters provided to $Onia2MuMu$ module few words must be spent

on how muons are reconstructed offline (that is after raw data from experiment has been saved) in CMS.

In the CMS standard offline muon reconstruction process, muons can be defined as three different object: standalone muons, tracker muons and global muons. Standalone muons are reconstructed only from the signal of the muon system, that is the Drift Tubes and the Cathode Strip Chambers, tracker muons are reconstructed only from the tracker signal and Global Muons are built as a combined fit of silicon and muon-chamber hits, coming from different track segments found in the tracker and muon systems. In the muon system at least two stations must be present.

Global Muon reconstruction, provides high-quality and high-purity muon reconstruction for tracks with $p_T > 4$GeV in the central pseudo-rapidity region, and $p_T > 1$ GeV in the forward region. Tracker Muon, however, achieves a better reconstruction efficiency at lower momenta.

The momentum measurement of muons and, more generally, of all charged tracks in the CMS detector is affected by systematic uncertainties due to imperfect knowledge of the magnetic field and of the material budget, to subdetectors misalignment and to biases in the algorithms which fit the track trajectory. Studies performed with cosmic-ray muons and collision data show a very precise control of all these possible biases.

This analysis uses the inclusive sample of *traker muons*, irrespectively of whether they are also reconstructed by the *global muon* reconstruction algorithm. The muon tracks are required to have at least 11 hits in the silicon tracker, of which at least two must be in the pixel layers and a compatible signal in the muon chambers. They must have a track fit χ^2 per degree of freedom smaller than 1.8, and be inside a cylinder of radius 4 cm and length 35 cm, whose barycenter is at (0, 0, 0) (with respect to CMS coordinates) and with the axis parallel to the beam line.

The single muon tracks are required to have $p_T > 3.3$ GeV for $|\eta| < 1.3$ and $p > 2.9$ GeV (total momentum) for $1.3 < |\eta| < 2.2$. In the offline data processing, a stricter cut is applied, of 1.0%, on the χ^2 probability of the dimuon vertex. Events are rejected if the distance in the plane transverse to the beam line between the dimuon vertex and the interaction point is larger than 100 μm (see figure 4.3), to reject muon pairs which have an invariant mass in the Υ mass region but which are not dimuons from Υ decays. In the (rare) cases when several dimuon candidates are found in the event, the one with the largest vertex χ^2-probability is retained.

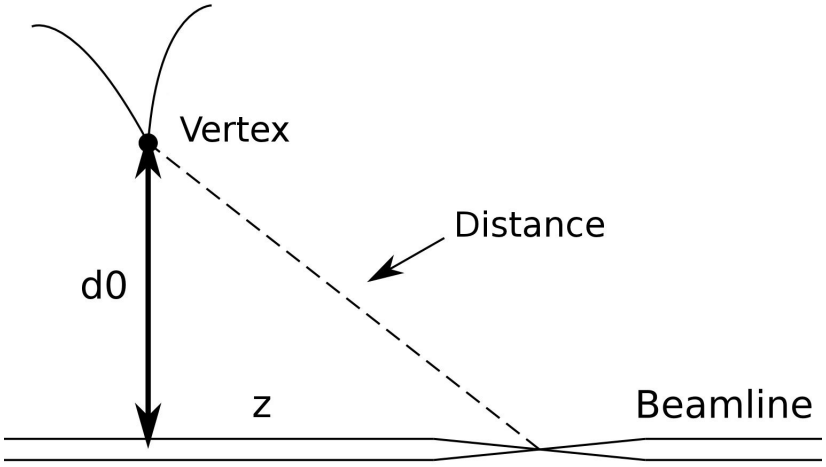

Figure 4.3: Schematic illustration of dimuon primary vertex

4.2.3 Photon reconstruction

The fundamental step in the χ_b candidate reconstruction is the reconstruction of the converted photon. This is a technically complicated step and, as will be shown later, it is the key ingredient to understand the ratio of reconstruction efficiency between $\chi_b(1P)$ and $\chi_b(2P)$.

The algorithm used in this analysis for photon conversion reconstruction has been developed within the CMS collaboration and it is described in detail in [9] [10].

Following is a brief summary of the algorithm specifications to select the conversion candidates and the modifications and additional cuts applied specific to this analysis.

Photon conversions are characterized by an electron-positron pair originating from the photon vertex. The invariant mass must be compatible with zero and the two tracks are therefore parallel at production vertex and open only in the transverse plane because of the magnetic field generated by the solenoidal superconducting magnet.

Photons originating from the radiative decay of the χ_b are relatively soft (with respect to typical LHC energies), and also the electron-positron pair resulting from an eventual photon conversions results is soft as well, moreover the pair tracks are asymmetric with one of the two leptons carrying most of the photon energy. Because the electrons produced in these conversions are of low energy, most of them are either fully stopped before they reach the electromagnetic calorimeter or they are bended in a spiral (helix in 3D) within the tracker, thus such conversions can be only reconstructed within the tracker detector. For this reason the algorithm is named tracker-only conversion reconstruction, as it uses only the tracker.

The algorithm relies on the capability of iterative tracking, described in [10], to efficiently reconstruct low-p_T and displaced tracks as the ones coming from a typical photon conversion.

Opposite-sign track pairs are firstly required to satisfy basic quality criteria, i.e. have ≥ 6 hits and normalised $\chi^2 < 10$. Then the tracker-only conversion finding exploits the conversion pair signature to distinguish genuine pairs from fake pairs. Tracks are required to have positive charge-signed transverse impact parameter (the primary vertex lies outside the track trajectory helix) and the distance of minimum approach in the xy

plane, d_m, between $-0.25cm$ and $1cm$ where d_m is defined as $d_{O_1-O_2} - (R_1 - R_2)$ where $d_{O_1-O_2}$ is the distance between the centres of the two track circles in the transverse plane and R_1 and R_2 are the two circles radii.

Further requirements include a small z separation between the tracks innermost points ($|\Delta z| < 5cm$) if they are in the barrel ($|z| < 120cm$) and a small opening angle in the longitudinal plane ($|\Delta \cot\theta| < 0.1$).

The two candidate conversion tracks must have one of the innermost two hits in the same detector layer. This to reduce the contribution of fake conversions due to soft displaced tracks that are artificially backward propagated.

Each conversion track candidate must be compatible in z, within five standard deviations, with at least one reconstructed primary vertex. Moreover the primary vertex closest in z to each track must be one of the two closest primary vertex of the other track.

Track pairs surviving the selection are then fitted to a common 3D-constrained kinematic vertex fitter. The 3D constraints imposes the tracks to be parallel in both transverse and longitudinal planes. The pair is retained if the fit converges and its χ^2 probability is greater than 5×10^{-4}.

For the present analysis only reconstructed conversion with a vertex transverse distance larger than $1.5cm$ with respect to the nominal beam spot are considered. This cut allows for the background contribution due to π_0 Dalitz decay to be suppressed while retaining photon conversion possibly occurring within the beam pipe volume.

The conversion reconstruction algorithm described above is not protected against the occurrence of a track shared among two or more reconstructed conversion. In this case only the conversion with the larger χ^2 probability is retained.

A reconstructed primary vertex is assigned to the photon reconstructed via the reconstruction of the conversion by extrapolating the reconstructed photon momentum and by choosing the closest vertex. If the distance is larger than ten standard deviations the conversion is rejected. The primary vertex associated to the conversion is required to be compatible with the reconstructed Υ vertex by asking their distance to be compatible within five standard deviations; furthermore, none of the two candidate muon tracks building the Υ vertex up must be the candidate electron or positron track of the reconstructed conversion vertex.

Finally each conversion candidate is associated to every other conversion candidate in the event, and to any Particle-Flow reconstructed photon. Particle-Flow photons are photons identified with the Particle-Flow algorithm.

The Particle-Flow algorithm consist in combining the information of the inner tracker, the electromagnetic and hadron calorimeter to try and associate to every track a cluster in the calorimeters. Once this step has been performed the ECAL clusters that weren't associated to any track are classified as Particle-Flow photons. This kind of photon identification is pretty loose allowing a high rate of fake photons. Any conversion building up a pair which invariant mass falls in the range between 2 standard deviation of the PDG π_0 mass is rejected, since it assumed to be compatible with a π_0 decay photon. Finally only reconstructed photons with $p_T > 0.5$ GeV are selected.

Further details on tracker physics performances and conversion reconstruction can be found in [8] [9] [10].

Some plot about reconstructed conversion as function of distance from the beam line and as function of p_T are shown in Figure 4.4

Some relevant plots about standard conversion reconstruction are shown in Figure 4.5, 4.6 and 4.7.

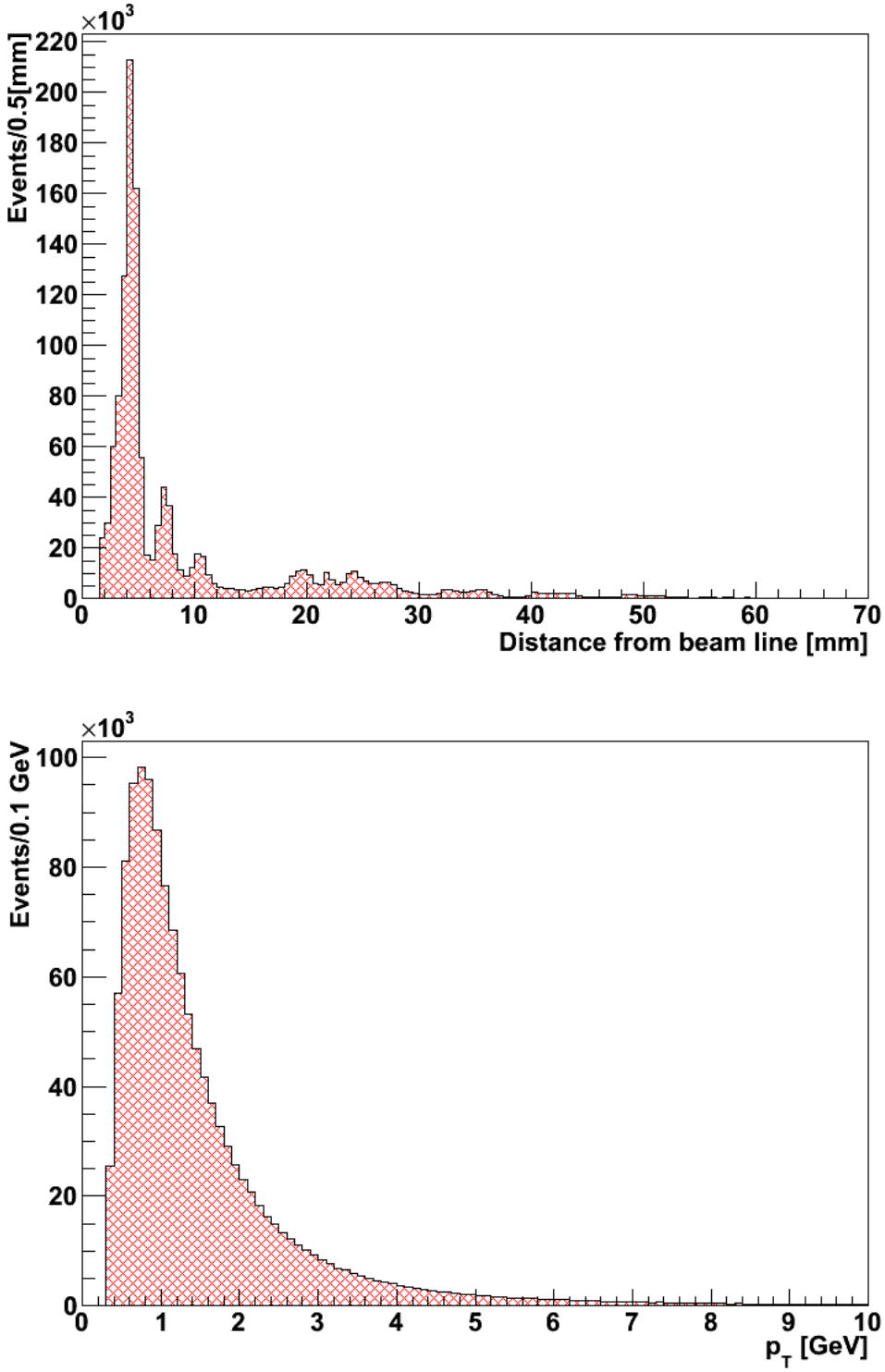

Figure 4.4: First figure, number of converted photons from 2011 data as a function of the distance from the beamline in mm, the first 3 peaks correspond to the pixel layers position. Second figure, number of converted photons from 2011 data as function of their transverse momentum in GeV.

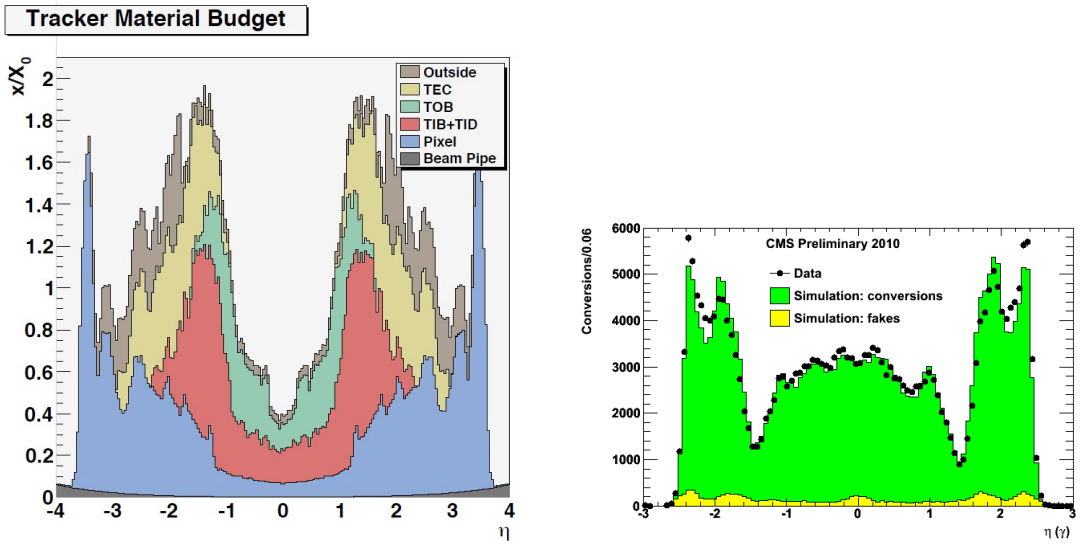

Figure 4.5: Material tracker budget in terms of radiation lengths (x/X_0) in function of pseudorapidity η and pseudorapidity distribution for all conversion candidates as reconstructed from the track-pair momentum in data and simulation (splitting fake candidates and real ones) [9].

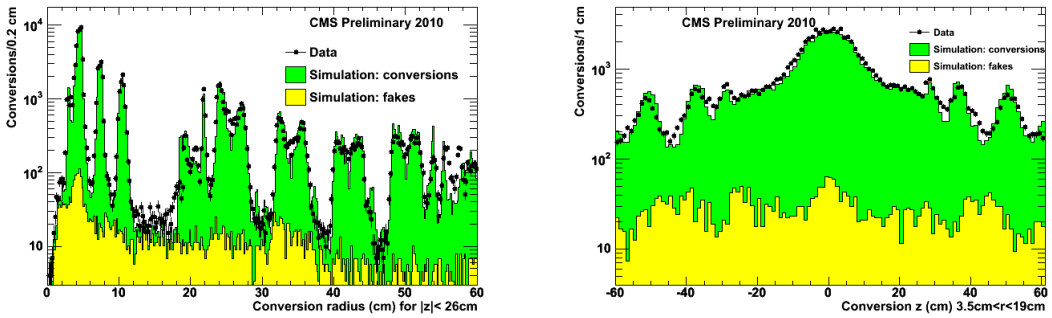

Figure 4.6: Conversion vertices: distributions of the radial position for $|z| < 26cm$, i.e. the central portion of the Tracker barrel, and longitudinal position for $3.5cm < R < 19cm$, i.e. Pixel Detector. In data the radius is calculated with respect to the centre of the Pixel detector. In simulation the contribution from real and fake conversions is splitted [9].

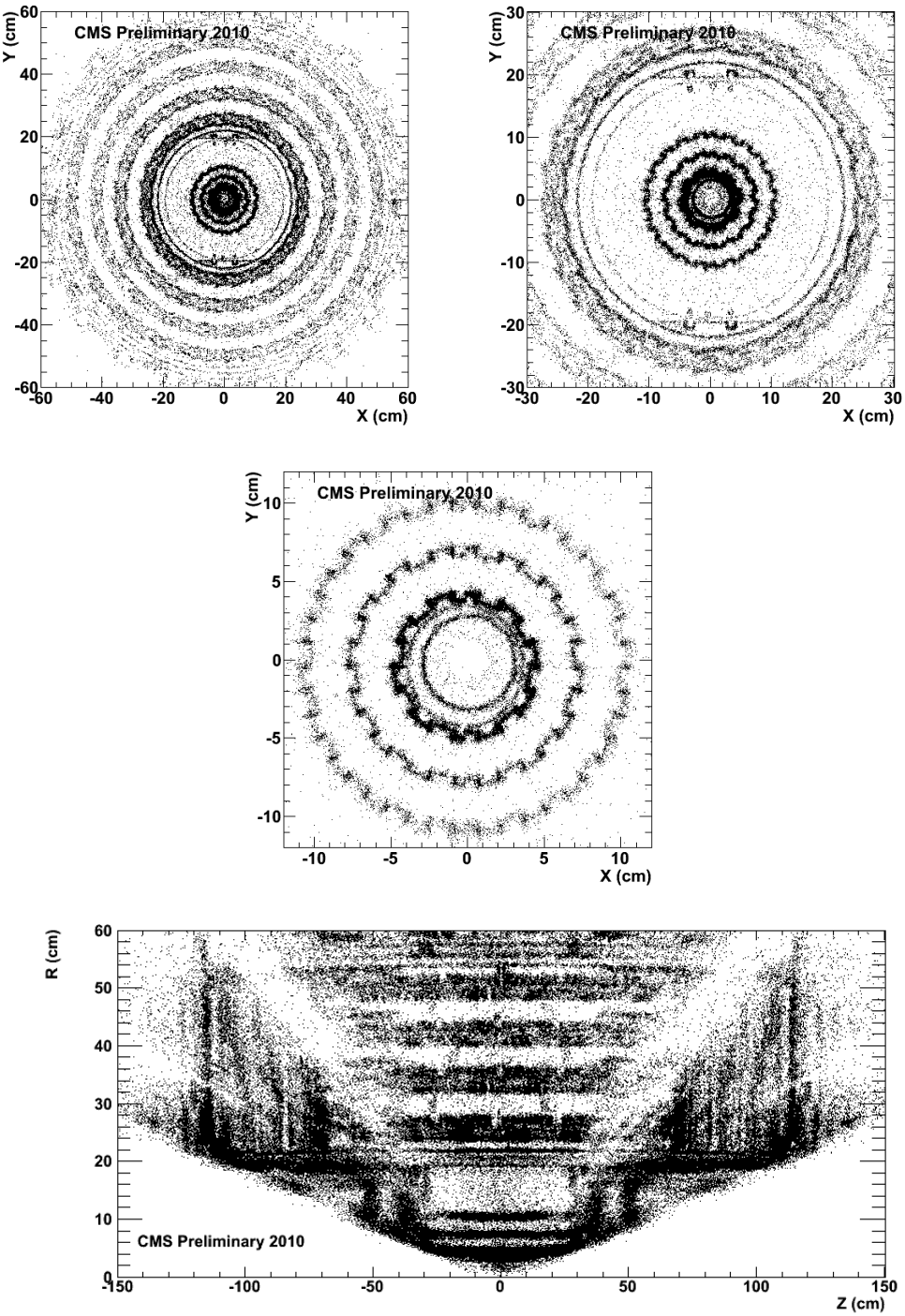

Figure 4.7: Conversion vertices in data in the (x, y) plane for $|z| < 26cm$ with increasing zoom and conversion vertices in data the (z, R) plane [9].

All the selections applied to this analysis are summarized in table 4.1.

Dimuon selection	
Track fit χ^2/ndf	< 1.8
Pixel layers with hits	≥ 2
Silicon tracker layers with hits	≥ 11
Fiducial cylinder around collision vertex	r = 4cm, h=35cm
$p_T(\mu)$ for $\|\eta\| < 1.3$	> 3.3 GeV
$p(\mu)$ for $1.3 < \|\eta\| < 2.2$	> 2.9 GeV
Tracker muon selector	$OneStationTight$
Dimuon vertex χ^2 probability	> 0.01
Transverse distance between dimuon vertex and interaction point	$< 100\mu m$
Photon selection	
Electron track hits	≥ 4
Electron track fit χ^2/ndf	< 10
Distance of approach	-0.25 cm $< d_m < 1$ cm
Signed impact parameter	$q \cdot d_0 > 0$
e^+ e^- vertex fit χ^2 probability	$> 5 \times 10^{-4}$
Minimum radius of conversion vertex	$\rho_{conv} > 1.5$ cm
$p_T(\gamma)$	≥ 0.5 GeV
π_0 rejection	$2\ \sigma$
χ_b **candidate selection**	
Photon - Υ vertex compatibility	5σ

Table 4.1: Summary table of selection cuts used in the analysis.

4.3 Reconstruction efficiency

The reconstruction efficiency is a measure of the ability to fully reconstruct a particle having measured the properties of it's decay products. Higher efficiency means that more particles can be reconstructed with respect to the total particles produced. Since there is no reliable way to know the number of produced χ_b by LHC nor other processes that would share a similar reconstruction efficiency of those of the χ_b, a Monte Carlo simulation is used to evaluate the reconstruction efficiency.

Called ϵ_n the total efficiency for a state nP, a possible difference between ϵ_1 and ϵ_2 must be considered. Efficiency is the result of experiment acceptance, kinematics range considered, photon conversion probability, converted photon reconstruction efficiency and Υ reconstruction efficiency. 1P and 2P states have a significant mass diffence (e.g. j=1 states have 363 MeV mass difference), this could result in different momentum spectra of both Υ and photon from decay, which, in turns, could result in different acceptance for each of the nP states.

A simulation is thus required to study variations of the reconstruction efficiency for the states 1P and 2P. The simulation produces a large amount of events with χ_b states and then reconstruct them with the same reconstruction software used on data analysis. The number of reconstructed events over the number of generated events in a certain kinematic region represent the total efficiency for a given state nP on that kinematic region.

The quantity needed to evaluate the ratio of the cross-section production of 2P over

1P states is the ratio $\frac{\epsilon_1}{\epsilon_2}$ which is the ratio of efficiencies for 1P and 2P states. this is defined as:

$$\frac{\epsilon_1}{\epsilon_2} = \frac{N_{reco}^{1P_1} + N_{reco}^{1P_2}}{N_{gen}^{1P_1} + N_{gen}^{1P_2}} / \frac{N_{reco}^{2P_1} + N_{reco}^{2P_2}}{N_{gen}^{2P_1} + N_{gen}^{2P_2}} \tag{4.2}$$

Where N_{reco} is the number of candidates reconstructed with the selection above, N_{gen} is the number of generated candidates in the kinematic range $|y(\Upsilon)| < 1.0$ and $p_T(\gamma) > 0.5$ GeV.

4.3.1 Monte Carlo configuration

To study the variation of the efficiency the simulation is performed using a PYTHIA6 particle gun. A particle gun simulator generate a single particle per event which is then decayed. The decay products of the generated particle are then processed into a full simulation of the CMS detector thus producing an output similar of that of real data. 10 million events where produced for each of 1P and 2P states, each event generated either a χ_{b1} in 57% of the events or a χ_{b2} in 43% of the events. The production ratio of χ_{b2} over χ_{b1} used in the simulation is the same measured in [26] for the production ratio of the χ_c meson: $\sigma_{\chi_{c2}}/\sigma_{\chi_{c1}}$. This is done because the production ratio of χ_b spin states is unknown while it is known the one of the χ_c which are rather similar states.

PYTHIA's particle gun was configurated to use PDG's masses, was then forced to decay all χ_b in $\Upsilon(1S) + \gamma$ and each $\Upsilon(1S)$ in $\mu^+ + \mu^-$. The relevant code used for PYTHIA configuration to generate 1P states is reported:

```
MSEL=61                         ! Quarkonia
MDME(1035,1)=1                  ! Upsilon -> mumu turned ON
MDME(1034,1)=0                  ! Upsilon -> ALL THE REST
MDME(1036,1)=0                  ! Upsilon -> ALL THE REST
MDME(1037,1)=0                  ! Upsilon -> ALL THE REST
MDME(1038,1)=0                  ! Upsilon -> ALL THE REST
MDME(1039,1)=0                  ! Upsilon -> ALL THE REST
MDME(1040,1)=0                  ! Upsilon -> ALL THE REST
MDME(1041,1)=0                  ! Upsilon -> ALL THE REST
MDME(1042,1)=0                  ! Upsilon -> ALL THE REST
BRAT(1565)=1.0                  ! chi_1b->Upsilon gamma 100%
BRAT(1566)=0.0                  ! chi_1b->g g   0%
BRAT(1043)=1.0                  ! chi_2b->Upsilon gamma 100%
BRAT(1044)=0.0                  ! chi_2b->g g   0%
```

To generate 2P states the two following lines where added to the above configuration to shift the mass of the χ_b states (J=1 and J=2) according to PDG values:

```
PMAS(294,1)=10.25546          ! Mass of chi_b1(2P)
PMAS(148,1)=10.26865          ! Mass of chi_b2(2P)
```

Since there is no work that studied the p_T distribution of the χ_b produced at LHC an approximation is needed. The particle with closest mass and properties with known p_T

spectrum is the Υ: the initial p_T spectrum of generated particle was setted according to a fit to the measured Υ p_T spectrum from [11]. The work of the reference studies the p_T distribution of Υ (1S), (2S) and (3S) measured in 2011 data with CMS experiment. The observed p_T spectrum is parametrized as:

$$f(x) = -axb^{\frac{1+x^2}{c}} \tag{4.3}$$

with the parameters for each Υ nS state reported in table 4.2.

	1S	2S	3S
a	0.1	0.1	0.1
b	3.46	3.25	3.05
c	69.1	83.4	84.5

Table 4.2: Parameters used in analytical form of p_T distribution of Υ.

The plot of the 3 PDF is shown in figure 4.8

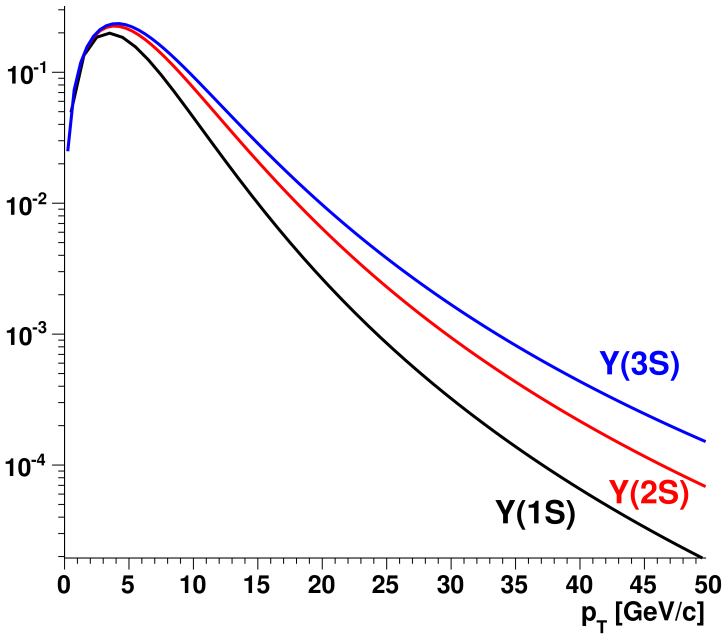

Figure 4.8: Analytical form of the p_T distribution of the Υ 1S, 2S and 3S obtained from the measured p_T of the work [11]

χ_b 1P and 2P where generated with both Υ 1S and 2S p_T spectrum to allow a complete study of systematic uncertainities deriving from the assumption on the distribution used.

4.3.2 Kinematic region

The efficiency of each state is sensible to the kinematic region in which it is calculated. In principle several distribution are involved in the evaluation of the efficiency, photons p_T and pseudorapidity, Υ p_T and rapidity and also photon reconstruction efficiency as

function of photon's p_T may all contribute to a variation of the efficiency according to the kinematical selection used.

To better understand the concept, in figure 4.9 and 4.10 are reported the plots of the relevant distributions as function of p_T and rapidity (or pseudorapidity in the case of photons) obtained from Monte Carlo simulation produced with the input p_T spectrum of the Υ(1S). Each figure shows both the generated distribution and the reconstructed distribution overlapping values for 1P state and 2P state.

Figure 4.9 shows the p_T distribution of photons and Υ from the simulated decays.

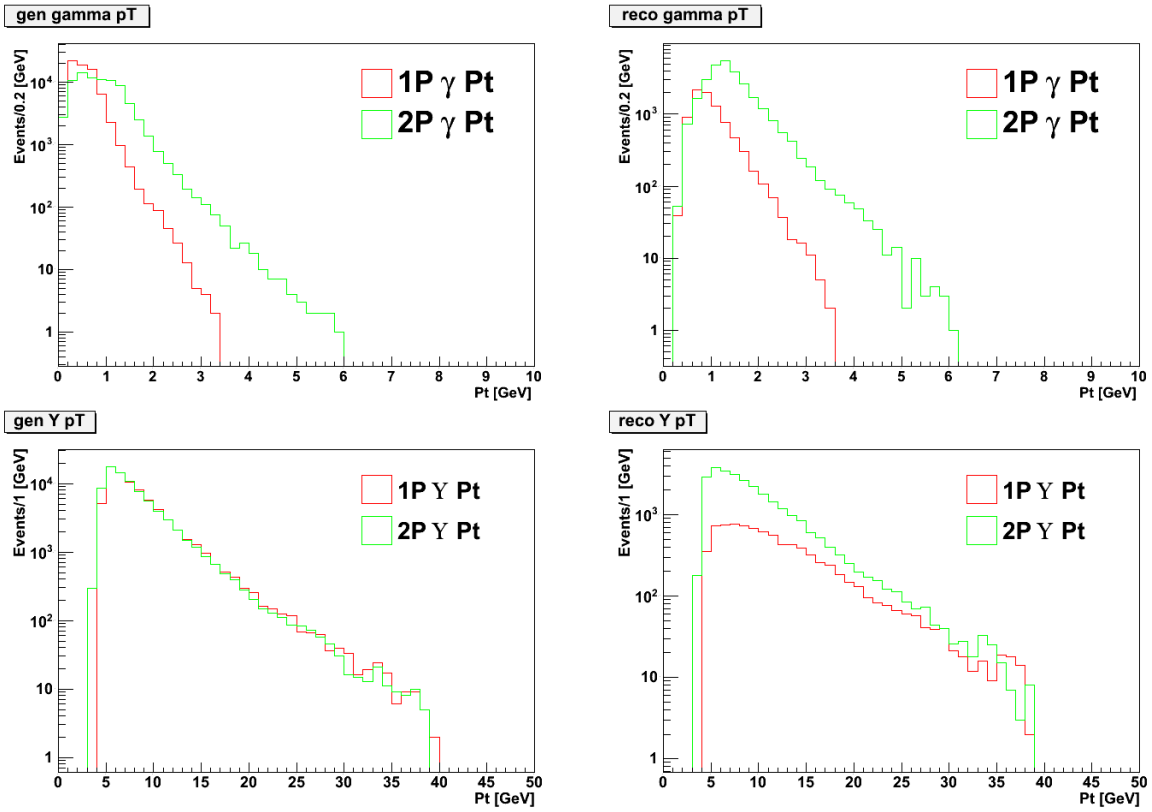

Figure 4.9: p_T of the Generated and Reconstructed photons and Υ

Note that while the p_T spectrum of the generated Υ is the same for the two states, the p_T spectrum of the reconstructed Υ is different for the two states, this is because the reconstructed Υ used for the plot are those from an event with a fully reconstructed χ_b candidate, therefore involving the reconstruction efficiency of the photon.

Figure 4.10 shows the pseudorapidity distribution of photons and rapidity distribution of Υ from the simulated decays.

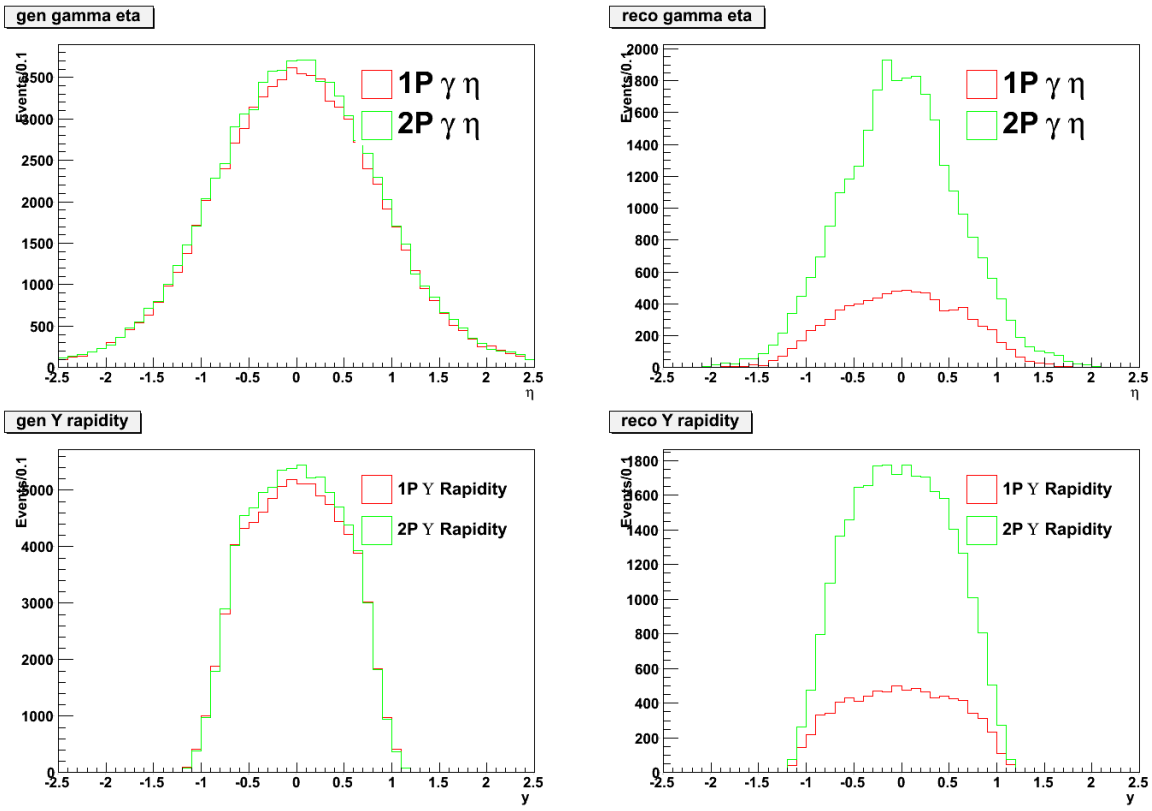

Figure 4.10: η of the Generated and Reconstructed photons and rapidity of Generated and Reconstructed Υ

From the plots it is clear that a possible variation in reconstruction efficiency between 1P and 2P should only lie in the different p_T spectrum of the generated photons. The p_T and rapidity distribution of the Υ and the pseudorapidity distribution of the photons are, indeed, very similar between 1P and 2P states and a selection on one of those kinematic variables should leave the efficiency ratio between the two state unmodified.

Figure 4.11 shows the conversion probability multiplied by the conversion efficiency of the photons as a function of the p_T of the photon. The plot was evaluated from a simulation and shows how dramatically the total conversion efficiency varies with different values of p_T of the photon.

It is, therefore, expected that only the selection on photon's p_T should lead to significant variation on efficiency ratio between the two considered states. In order to understand how p_T photons selection influences the efficiency one more distribution must be considered. The probability that a photon converts in CMS tracker and the reconstruction efficiency of the converted photons are not constant as function of photon's p_T. In figure 4.11 the the conversion probability multiplied by efficiency reconstruction of converted photons is plotted as function of photon's p_T.

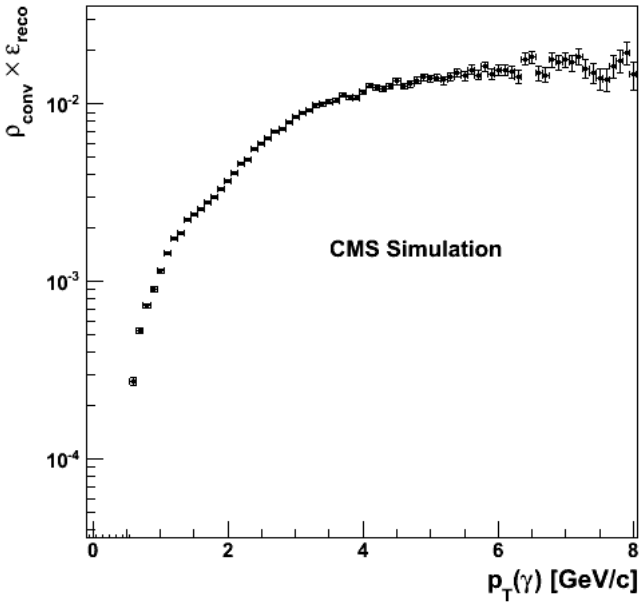

Figure 4.11: Conversion probability × converted photons reconstruction efficiency vs photon's p_T.

4.3.3 Result

The formula 4.2 is used to evaluate the ratio of efficiency $\frac{\epsilon_1}{\epsilon_2}$. In order to verify the hypothesis that the ratio is most sensible to p_T selection of photons the ratio is calculated for 15 values of minimum $\gamma(p_T)$ between 0.5 GeV and 2.0 GeV. The selection cuts are applied to both the number of Reconstructed events and to the number of Generated events. To reproduce the additional selection used in data Υ(1S) rapidity is asked to be between -1.0 and 1.0 and it's p_T to be greater than 3.0 GeV.

The study is performed with 7750000 Generated 1P states and 8020000 Generated 2P states, initial p_T spectrum of both states is setted to be the one of Υ(1S) as discussed above. Variations of the efficiency ratio using different generation p_T spectrum are treated as systematic uncertainties and discussed in the relative paragraph.

Figure 4.12 shows the plot of the efficiency ratio as function of the minimum $\gamma(p_T)$.

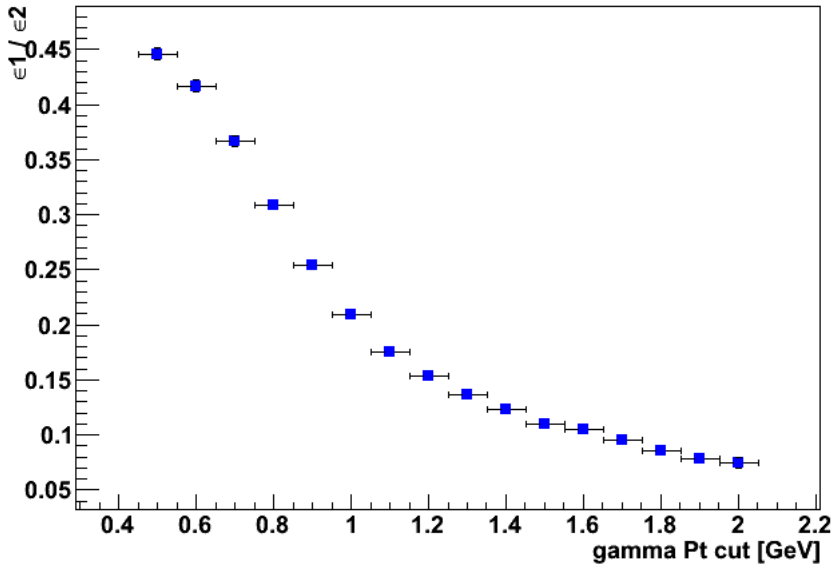

Figure 4.12: Efficiency ratio as function of minimum $\gamma(p_T)$.

The result obtained with $\gamma(p_T) > 0.5$ GeV is the one calculated for exactly the same kinematic region used in the data analysis. The estimation of the individual efficiencies for each state are: $\epsilon_1 = 0.0223 \pm 0.0003$ $\epsilon_2 = 0.0501 \pm 0.0002$ and the final value $\frac{\epsilon_1}{\epsilon_2} = 0.481 \pm 0.008$ is the one used to evaluate the cross-section ratio.

4.4 Data analysis

It's obtained as the convolution of a Gaussian distribution and two exponential function, one damping each tail of the Gaussian core Counting the number of 1P and 2P candidates requires, as previously said, a maximum likelihood fit to the events distribution as function of Q-value. A modelization of the signal shape is needed to extract the yield of χ_b 1P and 2P. Since the resonacnes are narrow, the lineshape is dominated by the experimental resolution. The fit is performed using 7 probability density functions. 6 Double Sided Crystall Ball PDF are used for each of the signal states nP^j (n=1,2,3;j=1,2) and one PDF for the combinatorial background.

The Crystal Ball is a function composed of a gaussian core, described by the two parameters μ and σ, and an exponential tail and is commonly used to describe processes in which radiative losses are important. The Double Sided Crystal Ball has exponential tails on both sides. It's analytical form is:

$$f_{CB}(m) = \begin{cases} (n_1/|\alpha_1|)^{n_1} e^{-\alpha_1^2/2} (\frac{n_1}{\alpha_1} - \alpha_1 - \frac{m-m_0}{\sigma})^{-n_1}, \text{ for } \frac{m-m_0}{\sigma} \leq -\alpha_1 \\ e^{-\frac{(m-m_0)^2}{2\sigma}}, \text{ for } -\alpha_1 < \frac{m-m_0}{\sigma} < \alpha_2 \\ (n_2/|\alpha_2|)^{n_2} e^{-\alpha_2^2/2} (\frac{n_2}{\alpha_2} - \alpha_2 - \frac{m-m_0}{\sigma})^{-n_2}, \text{ for } \frac{m-m_0}{\sigma} \geq \alpha_2 \end{cases} \quad (4.4)$$

Each Double Sided Crystal Ball function has six parameters: α_1, n_1, α_2, n_2, σ and m_0. α_1 and α_2 are the transition points of respectively the first and the second exponential

functions, n_1 and n_2 are the exponential base of the two functions, σ is the variance of the gaussian core and m_0 it's mean.

The evaluation of the 6 parameters is done by fitting the Monte Carlo samples created for the efficiency study using ROOFIT [29]. A sample for 3P states was created as well using the mass of $m_{3P_1} = 10.511$ GeV and $m_{3P_2} = 10.523$ GeV according to the theorical work in [21], the production ratio of J=2 over J=1 states was setted to a test value of 0.5. Each nP_j (n=1,2,3;j=1,2) signal is fitted individually, n_1 and n_2 are fixed and are the same for all signals, particularly the values $n_1 = 3.0$ and $n_2 = 2.0$ are used.The parameters α_1, α_2, m_0 and σ are left free in the fit. The number of reconstructed candidates in Monte Carlo simulation is known and therefore the number of events for each signal is fixed as well allowing the fitting algorithm to process the lowest possible number of free parameters. Figure 4.13 shows the resulting fits.

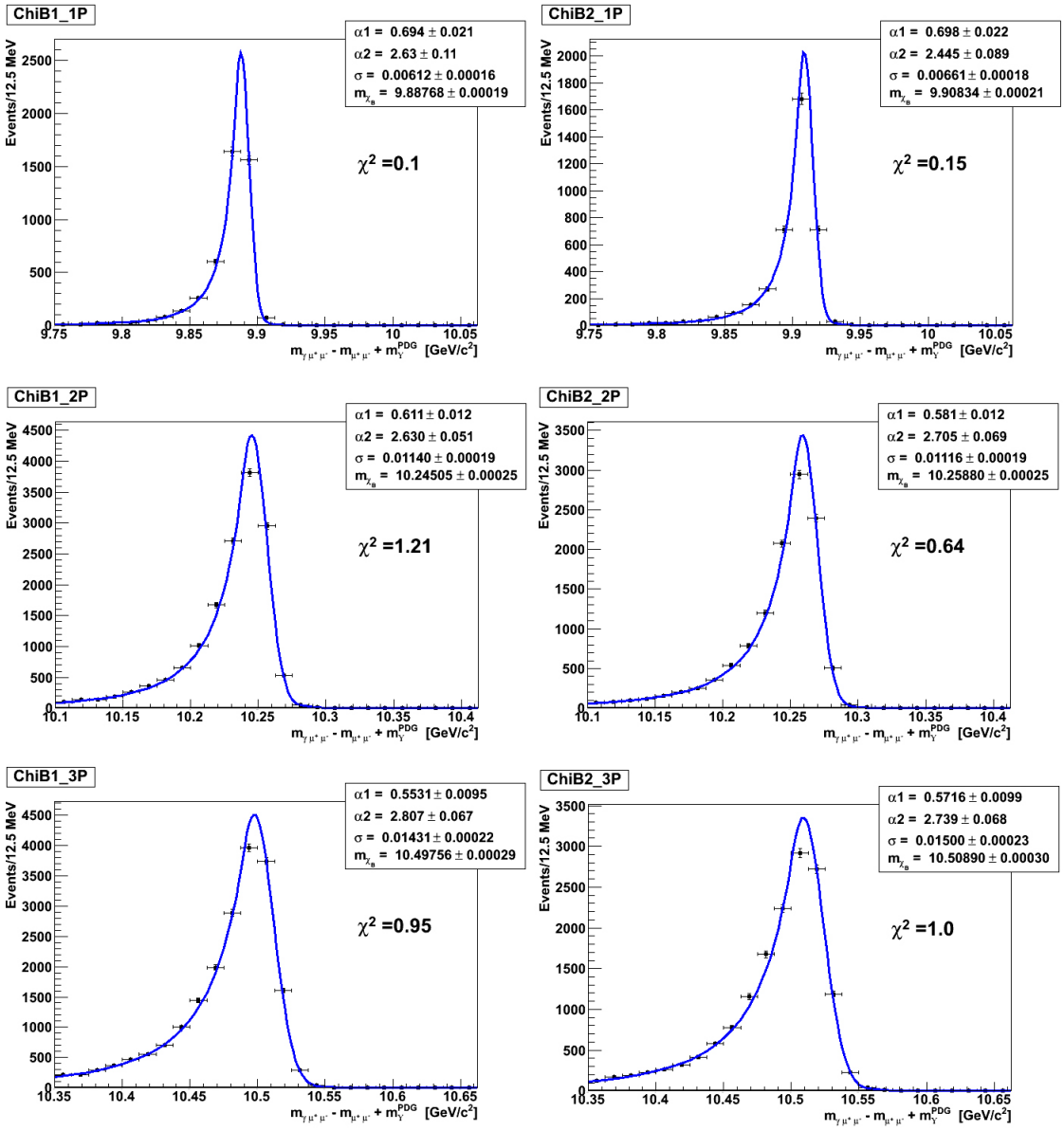

Figure 4.13: Fits of Monte Carlo samples of χ_b $1P_1$,$1P_2$,$2P_1$,$2P_2$,$3P_1$,$3P_2$

Data sample is then fit using 7 probability density functions. 6 Double Sided Crystall Ball PDF are used for each of the signal states nP_j (n=1,2,3;j=1,2) and one PDF for the combinatorial background, defined as:

$$N_{bkg} = (x - q_0)^{\alpha_1} \cdot e^{(x-q_0)\cdot\beta_1} \tag{4.5}$$

The resulting PDF is of the form:

$$P(Q) = \sum_{i=1}^{6} N_i \cdot S_i(Q) + N_B \cdot S_B(Q) \tag{4.6}$$

The parameters of each PDF are fixed to those value estimated with Monte Carlo samples (α_1, α_2, σ, m_0) and all signals have n_1 and n_2 setted to the values used for

simulation sample. The number of events for each state N_i, the number of background events N_B and background parameters are left free. In order to perform the fit an assumption on the unknown ratio of Spin 2 over Spin 1 states production is necessary, therefore the production ratio of χ_{c2} over χ_{c1} found in [26] is used for 1P and 2P states corrected for their Branching Ratio resulting in $R_{1P} = 0.57$ $R_{2P} = 0.68$. 3P states Branchig Ratios are unknown, therefore a test value for J=2 over J=1 production ratio of 0.5 was used. Note that the assumptions on spin production ratio has no effect on following results since the yield of 1P and 2P considers all spins of each state.

To plot the mass spectrum with the correct value, $\Upsilon(1S)$ mass from PDG [?] tables is added to the Q-value invariant mass.

Figure 4.14 shows the result of the fit on data.

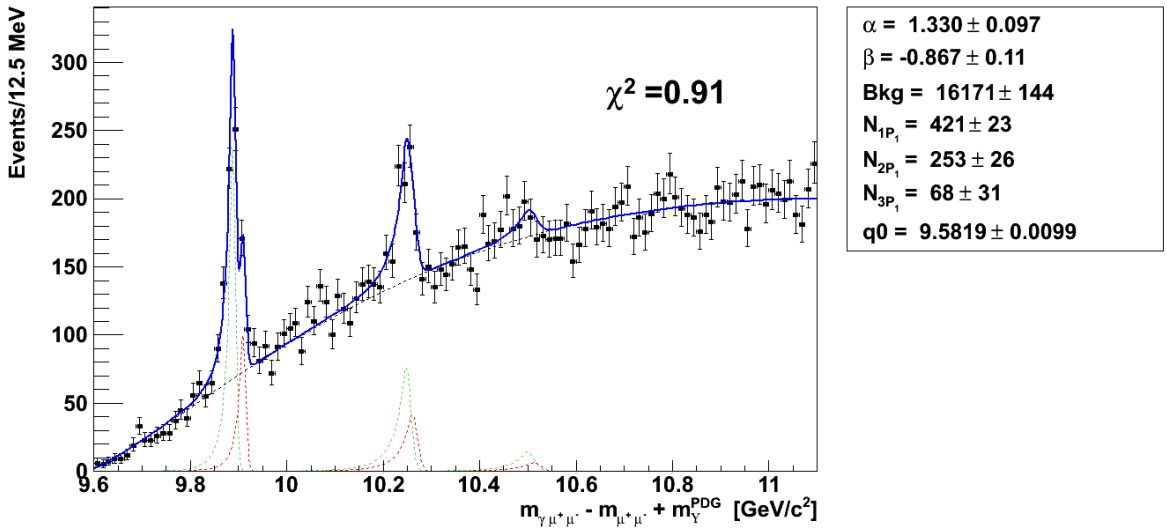

Figure 4.14: Unbinned maximum likelihood fit of χ_b invariant mass spectrum

The yield estimated on the examined dataset within the considered kinematical region amounts to 600±33 χ_b(1P) and 398±41 χ_b(2P). The ratio of 2P over 1P state is thus $\frac{N_2}{N_1}$ = 0.66 +/- 0.08 and correcting for the efficiency ratio found on previous paragraph it is possible to obtain the cross-section ratio times Branchin Ratios ratio: $\frac{\sigma_2}{\sigma_1} \times \frac{BR(\chi_b(1P)\to\Upsilon(1S)\gamma)}{BR(\chi_b(2P)\to\Upsilon(1S)\gamma)}$ = 0.32±0.03 where for both ratios only statistics errors are reported.

4.5 χ_b(1P) spin states J=2 over J=1 production ratio

The experimental resolution is such to allow an estimation of the spin states production ratio of the 1P resonance. The hypothesis that the production ratio of the spin states J=2 over J=1 is the same of the one found for the χ_c in [26] is tested. The production cross-section ratio for the χ_c spin states is $\sigma_{\chi_{c2}}/\sigma_{\chi_{c1}} = 0.759\pm0.025(\text{stat.})\pm0.015(\text{syst.})\pm0.043(\text{BR})$, the observed quantity in the data, however, is

$$R_b(1P) = \frac{\sigma_{\chi_{b2}}}{\sigma_{\chi_{b1}}} \times \frac{BR(\chi_{b2} \to \Upsilon(1S) + \gamma)}{BR(\chi_{b1} \to \Upsilon(1S) + \gamma)} \tag{4.7}$$

Imposing the same cross-section production ratio of the χ_c and substituting the values for the branching ratios (BR(χ_{b1} = (33.9±2.2)% and BR(χ_{b2} = (19.1±1.2)%) the observable value to be tested can be obtained: $R_b(1P)$=0.43±0.014(stat.)±0.008(syst.)±0.025(BR) (where the errors on all Branching Ratios are considered togheter).

Performing a fit of the invariant mass spectrum as done in the previous paragraph leaving the ratio of the two spin states free allows to check if the above hypothesis is correct. The fit is performed only in the mass region of χ_b(1P) between 9.6 and 10.2 GeV, the parameters defining the yield of $1P_1$ and $1P_2$ states are free as well as the parameters describing the background. Figure 4.15 shows the result of the fit.

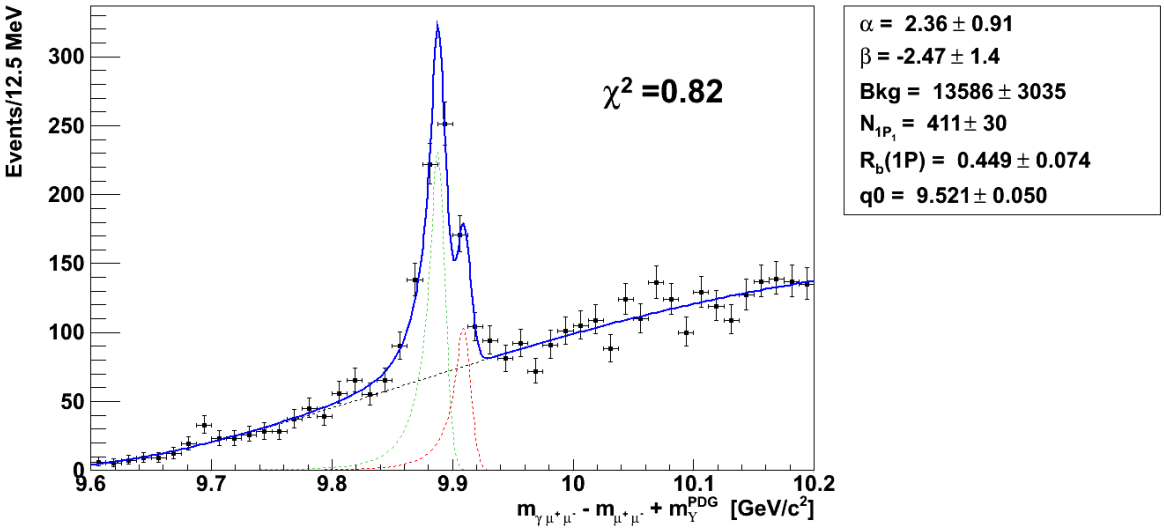

Figure 4.15: Unbinned maximum likelihood fit of χ_b invariant mass spectrum in the region of 1P resonance, with the spin ratio production left free.

From the fit a value of $R_b(1P)$=0.45±0.07 is found, which is perfectly compatible with the value calculated with the hypothesis above explained.

Note that a possible variation in reconstruction efficiency of the two spin states should also be considered and the found value eventually corrected, however considering the very narrow energy spacing between the two states in comparison to their mass it is assumed that the efficiency correction can be neglected.

4.6 Systematic uncertainties

Possible variations in the number of counted χ_b (1P) and (2P) due to different assumptions fitting the Q-value or calculating the efficiency ratio are here considered as source of systematic uncertainties. A conservative approach is followed evaluating the systematic errors.

Variations of the Q-value range in which the fit is performed result in different evaluated parameters of the fit, thus in different yields of χ_b states as well. Since the signal of the 1P resonance is too close to the lowest values of the Q-value available on the dataset,

the study is performed varying only the upper limit of the fitting range: between 10.6 GeV and 11.1 GeV the range is increased in step of 100 MeV for a total of 5 fits. The obtained ratios N_2/N_1 and $\sigma_2/\sigma_1 \times B_2/B_1$ (where B_n stand for $BR(\chi_b(nP) \to \Upsilon(1S)+\gamma)$ for the different fits are reported in table 4.3.

Fitting range	N_2 / N_1	$\sigma_2/\sigma_1 \times B_2/B_1$	χ^2/ndf	Prob.
[9.6, 10.6]	0.63±0.08	0.30±0.04	0.92	1.0
[9.6, 10.7]	0.63±0.08	0.31±0.04	0.91	1.0
[9.6, 10.8]	0.64±0.08	0.31±0.04	0.96	1.0
[9.6, 10.9]	0.64±0.08	0.31±0.04	0.92	1.0
[9.6, 11.0]	0.65±0.08	0.32±0.04	0.91	1.0
[9.6, 11.1]	0.66±0.08	0.32±0.04	0.91	1.0

Table 4.3: N_2/N_1 and $\sigma_2/\sigma_1 \times B_2/B_1$ for different fitting range with the obtained reduced χ^2 and it's probability.

From the result of the table 4.3 the extreme value of $\sigma_2/\sigma_1 \times B_2/B_1$ from the measure is used and the difference between its value and the measured one is used as systematic error of: $^{+0\%}_{-6\%}$.

The fit to the data is performed using a different PDF for the χ_b signal and a different PDF for the background signal to test if the ratio of counted number of 1P and 2P events varies. The χ_b resonances are fitted with a standard ROOFIT Crystal Ball function and the background with another standard ROOFIT PDF: the RooDstD0BG which is a a distribution designed to fit the background in the studies of D* - D^0 mass distribution in the radiative decay of the D* meson. The fit result in a χ^2/ndf of 0.99, $N_2/N_1 = 0.73\pm0.08$ and $\sigma_2/\sigma_1 \times B_2/B_1 = 0.35\pm0.04$. The result is different respect the one found fitting with the previously described PDF, a systematic error of ±9% is taken.

The assumption on the production ratio of J=1 over J=2 states is relaxed and the fit is performed leaving that parameter free for both 1P and 2P resonance, while leaving all the other parameters the same as in data analysis. The fit result in a χ^2/ndf of 0.66, the spin production ratio on 1P signal is evaluated by the fit to be $R_1 = 0.46\pm0.08$ and for 2P signal $R_2 = 0.6\pm0.3$, $N_2/N_1 = 0.7\pm0.2$ and $\sigma_2/\sigma_1 \times B_2/B_1 = 0.32\pm0.08$. The result is statistically compatible with the one previously found using an assumption on the spin ratio production, therefore no systematic uncertainty is evaluated from this study.

As previously mentioned the lack of knowledge of the production p_T spectrum of χ_b is the more realistic to be used in Monte Carlo simulations is treated as source of systematic uncertainty on efficiency ratio evaluation. Another set of simulations was produced using the measured p_T spectrum of Υ(2S) from [11] to generate the initial p_T spectrum of 1P and 2P χ_b. The efficiency ratio is calculated as indicated in a previous paragraph and all the possible combinations involving at least one of the two χ_b sample generated with Υ(2S) p_T spectrum are considered. Table 4.4 shows the different values of efficiency ratios obtained with different combinations of generation p_T spectrum and also $\sigma_2/\sigma_1 \times B_2/B_1$ obtained with those values.

1P gen p_T	2P gen p_T	ϵ_1 / ϵ_2	$\sigma_2/\sigma_1 \times B_2/B_1$
1S	2S	0.441±0.006	0.29±0.04
2S	1S	0.499±0.007	0.33±0.04
2S	2S	0.594±0.009	0.39±0.05

Table 4.4: ϵ_1 / ϵ_2 and $\sigma_2/\sigma_1 \times B_2/B_1$ for the three different combinations involving at least one χ_b sample generated with Υ(2S) spectrum.

The difference of the measure with the extreme values is taken as systematic error of: $^{+19\%}_{-9\%}$.

The statistical error on the evaluated efficiency ratio ϵ_1 / ϵ_2 is treated as a systematic error. The evaluated efficiency ratio is ϵ_1 / ϵ_2 = 0.481±0.08, propagating the error to N_2/N_1 gives an error of ±9% which is kept as systematic error.

Table 4.5 summarize the evaluated systematic errors.

Uncertainty source	Evaluated error on $\sigma_2/\sigma_1 \times B_2/B_1$
Fitting in different ranges	$^{+0\%}_{-6\%}$
Fitting with different PDF	±9%
No assumption on J=2 over J=2 production	*non significant*
Uncertainty on generation p_T spectrum	$^{+19\%}_{-9\%}$
Statistical error on ϵ_1 / ϵ_2	±9%
Total	$^{+22\%}_{-19\%}$

Table 4.5: Systematic errors on the measure $\sigma_2/\sigma_1 \times B_2/B_1$.

The final systematic error on $\sigma_2/\sigma_1 \times B_2/B_1$ considered is therefore the squared sum of the single contribution and its value is: $^{+22\%}_{-9\%}$.

4.7 Results

The cross-section production ratio in the kinematic region $|y(\Upsilon)| < 1.0$ and $p_T(\gamma) > 0.5$ GeV is thus evaluated to be $\sigma_2/\sigma_1 \times B_2/B_1 = 0.32\pm0.03(\text{stat.})^{+0.07}_{-0.06}(\text{syst.})$.

It is also possible to evaluate the absolute cross-section production ratio extracting the Branching Ratios constribution as indicated in eq 4.1. The four involved Branching Ratios are summarized in table 4.6.

State	Branching ratio
$1P_1$	(33.9±2.2)%
$1P_2$	(19.1±1.2)%
$2P_1$	(9.2±0.8)%
$2P_2$	(7.0±0.7)%

Table 4.6: Branching ratios of χ_b $1P_1$, $1P_2$, $2P_1$, $2P_2$ of the decay Υ (1S) + γ.

To evaluate a mean Branching fraction for each of the two state 1P and 2P is again necessary an assumption on the production ratio of the spin state J=2 and J=1. As done

before it assumed that the production ratio of the two spin state is the same of the one measured for the χ_c in [26]: J=2 / J=1 = 0.759.

The Branching fraction ratio result, therefore, in $B_1/B_2 = 3.3 \pm 0.4$.

The cross-section production ratio can thus be evaluated:

$$\frac{\sigma_{\chi_b(2P)}}{\sigma_{\chi_b(1P)}} = 1.1 \pm 0.1(stat.) \pm 0.2(syst.) \pm 0.1(BR). \tag{4.8}$$

This ratio is significantly higher with respect to the one predicted by the theoric work in [1]. However the cited work only consider χ_b prompt produced, that is χ_b mesons that are directly produced form the proton-proton collision. There are, however, other particle that decays into χ_b both 1P and 2P. Υ(2S), for instance, have a significant Branching Ratio in χ_b(1P) and Υ(3S) a signinficant Branching Ratio in χ_b(2P) (and a negligible one in χ_b(1P)).

It is possible to use the cross-section of the Υ measured by the work in [11] to evaluate the contribution to the χ_b production from Υ 2S and 3S decays. The cross-sections of the work [11] are expressed multiplied by the Branching Ratio of the Υ in $\mu^+ + \mu^-$, therefore the cross-section must be divided by that Branching Ratio and then multiplied again by the Branching Ratio in $\chi_b + \gamma$, that is:

$$\frac{\sigma(\Upsilon(3S) \to \chi_b(2P) + \gamma)}{\sigma(\Upsilon(2S) \to \chi_b(1P) + \gamma)} =$$

$$= \frac{\sigma(pp \to \Upsilon(3S))}{\sigma(pp \to \Upsilon(2S))} \times \frac{BR(\Upsilon(2S) \to \mu^+\mu^-)}{BR(\Upsilon(3S) \to \mu^+\mu^-)} \times \frac{BR(\Upsilon(3S) \to \chi_b(2P) + \gamma)}{BR(\Upsilon(2S) \to \chi_b(1P) + \gamma)} \tag{4.9}$$

Substituting the values found on [11] for the Υ cross-section production and the values of PDG for the Branching Ratio the constribute of the Υ to the production of χ_b can be evaluated: $\sigma^{\Upsilon}_{\chi_b(2P)}/\sigma^{\Upsilon}_{\chi_b(1P)} = 0.81 \pm 0.05$.

Summing this ratio with the one found on the theoric prediction gives an approximate value of 0.6 wich is still lower than the measured one. However there can be other, yet undiscovered, bottmonium states contributing to the total production of χ_b states which, in principle, could further modify the total production cross-section of χ_b.

Chapter 5

Measurement of the χ_b(3P) resonance

The exploration of the mass region between the 2P resonance and the $B\bar{B}$ mass threshold brings intersting results. An excess of events around the region of 10.5 GeV is observed, similar to the one discovered by ATLAS and identified as the χ_b(3P) resonance. It is indeed reasonable that, if such a state exist, it might have similar behaviour of lower masses states 1P and 2P and it should have an open decay channel in $\Upsilon(1S) + \gamma$. It is assumed that the 3P state comes in a triplet of spin as the 1P and 2P states, no information on each of the spin state is available: mass, width and Branching Ratios of each of the three spin states are yet unkown. It is reasonable to assume that the excess of events observed is a superposition of J=1 and J=2 spin states of 3P, while J=0 probably has too small contribution due to the low expected Branching Ratio with respect to other spin states, similarly to what occurs in 1P and 2P states. It is also reasonable to assume that the separation in mass between J=1 and J=2 states is inferior to the experimental mass resolution and, therefore the two spin states are indistinguishable to our experiment. What can be done, therefore, is to evaluate the barycenter of the 3P state, without resolving the single contributions from J=1 and J=2 states.

In order to measure the 3P barycenter, it will be needed to achieve a good understanding of the energy scale at the energies of interest for our measurement. In particular, the accuracy in the measurement of the photon momentum plays a fundamental role, as will be described in the following.

5.1 Barycenter of 3P state

The technique is the same explained in the previous chapter: the Q-value is calculated and a maximum likelihood fit performed. The signal is parametrized with 6 Double Sided Crystall Ball function (eq. 4.4) and an exponential background function (eq. 4.5).

An assumption on the relative abundance of the J=1 and J=2 states and their mass is necessary to perform the fit to the invariant mass. It is therefore assumed that spin J=0 has no contribution to the signal, the ratio of J=2 over J=1 states is 0.5 -similar to the one found for χ_c in [26]- and that the mass difference between J=1 and J=2 is of 12 MeV, according to theorical value found on the work in [20]. Variations of the result consequent to different assumptions will be evaluated as source of systematical error.

The data used for the study and the selections are the same used in the previous chapter.

The fit to the Q value spectrum performed to obtain 3P state mass is done similarly to the fit performed for 1P and 2P states. The parameter representing the mass of J=1 state is free and also the two σ of each spin. The mass of the J=2 state is set to be 12 MeV greater than the one of J=1, making that parameter fixed. All the parameters concerning 1P and 2P states are the one used for the cross-section production study in the previous chapter, the number of events of 1P and 2P are also fixed to the numbers obtained with the previous fit. All the parameters concerning the background (fitted with the same function used in the previous chapter), that is $\alpha, \beta, q0$ and the number of background events are left free. Figure 5.1 shows the result of the fit.

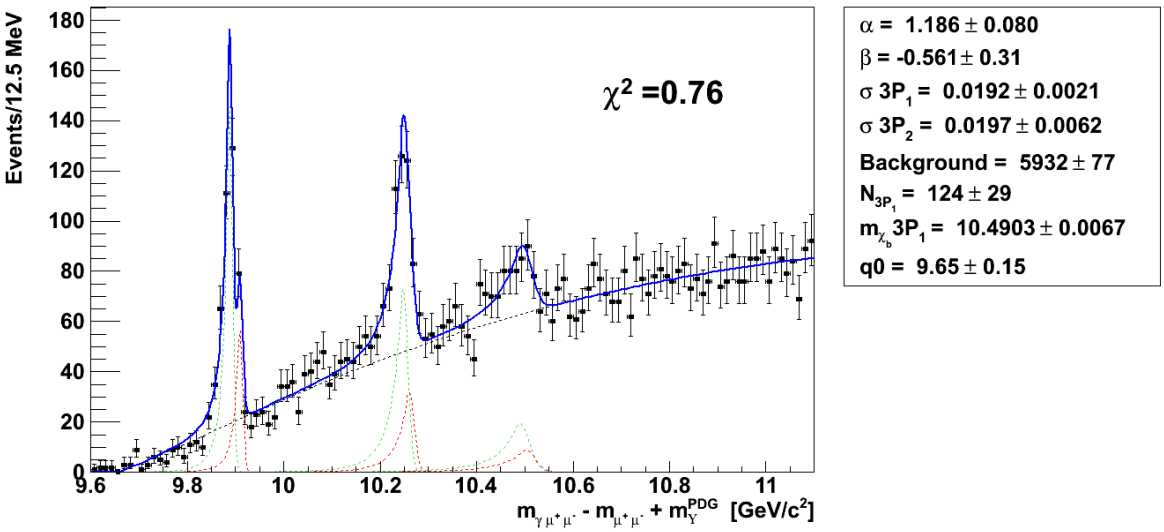

Figure 5.1: Unbinned maximum likelihood fit of χ_b invariant mass spectrum

The barycenter of mass is found to be $m_{3P} = 10.494 \pm 0.004$ GeV, which still needs to be corrected by the PES value.

5.2 Photon Energy Scale

The use of the Q-value, wich is the difference of the invariant mass of the di-muon and the photon minus the invariant mass of the di-muon, has the advantage that the event by event uncertainty on the dimuon invariant mass due to the finite momentum resolution cancels out.

The χ_b Q-value, therefore, cannot depend on the estimation of di-muon invariant mass but its accuracy and precision depend on the calibration and resolution of the gamma momentum measurement.

The electron and the positron deriving from the photon conversion lose energy in the tracker which can't be recovered. The two leptons, indeed, are subjected to brehmsstrahlung and multiple scattering because of their trajectory inside CMS's tracker material and they

are also subject to syncrotron radiation because of the strong magnetic field that causes their curvature. It is therefore necessary to estimate the fraction of unrecovered energy of the converted photons and check whether it is constant for different photon energies in the considered energy window.

The correction to the mass estimated with the mentioned method is called Photon Energy Scale (PES).

One method to estimate the PES is then to evaluate the Q-value of the reconstructed Monte Carlo signals used in the previous chapter and divide that Q-value by the "real" Q-value of the same states as read from PDG. Once the PES is evaluated the mass can be obtained with the simple formula:

$$M^{corr}_{\chi_b(3P)} = Q_{\chi_b(3P)}/f_{PES} + M^{PDG}_{\Upsilon(1S)} \tag{5.1}$$

In table 5.1 the measured Q-value of Monte Carlo sample and the PDG Q-value of the same states are reported.

State	MC Q	PDG Q	PES
$1P_1$	0.4262 ± 0.0005	0.4325 ± 0.0005	0.9855 ± 0.0017
$1P_2$	0.4467 ± 0.0004	0.4519 ± 0.0005	0.9885 ± 0.0014
$2P_1$	0.7840 ± 0.0003	0.7952 ± 0.0006	0.9860 ± 0.0009
$2P_2$	0.7977 ± 0.0003	0.8083 ± 0.0006	0.9869 ± 0.0008
$3P_1$	1.0367 ± 0.0004	1.0507 ± 0.0010	0.9867 ± 0.0010
$3P_2$	1.0477 ± 0.0004	1.0627 ± 0.0010	0.9859 ± 0.0010

Table 5.1: Table of Monte Carlo Q-value, PDG Q-value and PES of the six χ_b states.

This results are then fitted with a constant function to test the hypothesis that the PES is constant as a function of Q-value. The plot in figure 5.2 shows the result of the fit.

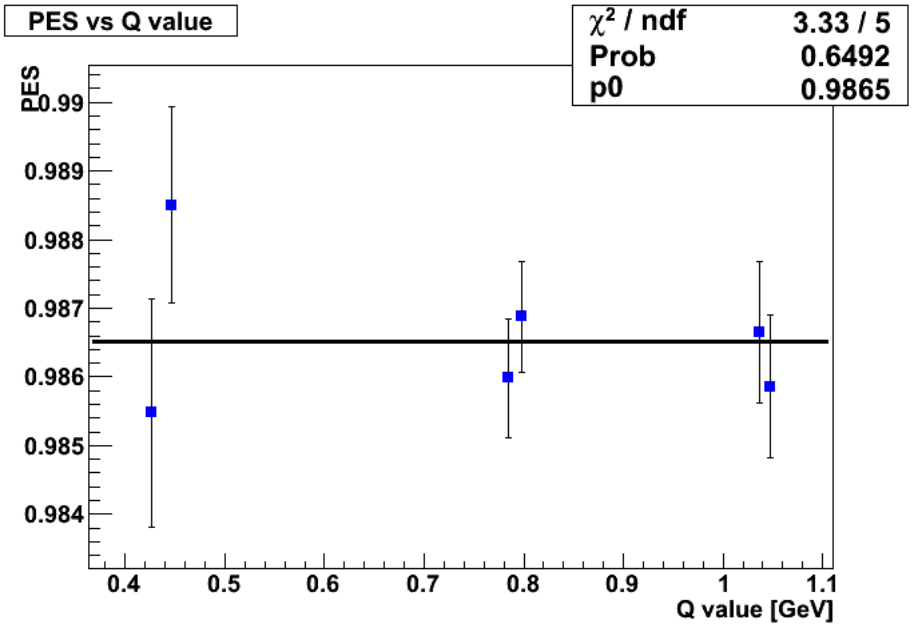

Figure 5.2: Plot of the PES as function of measured Q-value

The probability value of the χ^2 test is such that the null-hypothesis cannot be rejected. Therefore the hypothesis of a constant PES as a funtion of Q-value is considered correct and the resulting correction factor is evaluated from the fit to be $f_{PES} = 0.9865 \pm 0.0004$.

The barycenter corrected with the above PES value is $m_{\chi_b(3P)} = 10.509 \pm 0.004$, reporting statistical error only.

PES can also be evaluated by a complete data-driven method. The method developed in [28] uses the measured Q-value of four different states: χ_{c1}, χ_{c2}, χ_b(1P) barycenter and χ_b(2P) barycenter, then divided by the corresponding Q-value obtained from PDG tables. The masses of the two χ_c state are obtained from the fit to the Q-value of [26] whose plot is shown in figure 5.3. χ_b 1P and 2P masses, instead, are evaluated from a fit to the Q-value in [28] whose plot is shown in figure 5.4.

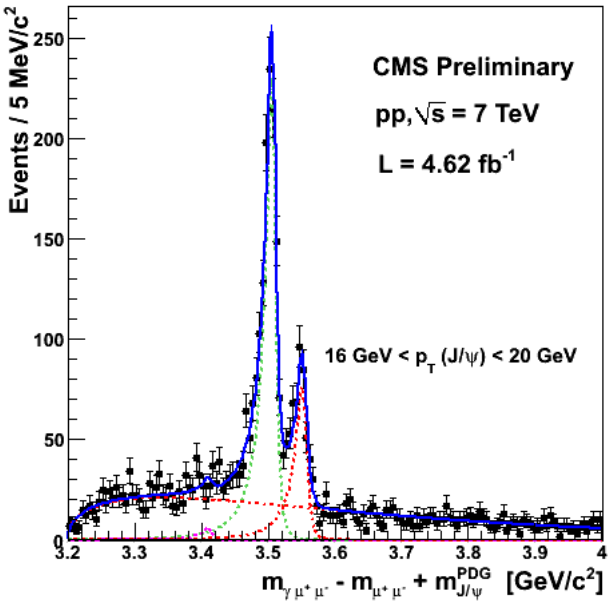

Figure 5.3: Fit to the Q-value of charmonium resonances χ_{c0}, χ_{c1} and χ_{c2} from [26].

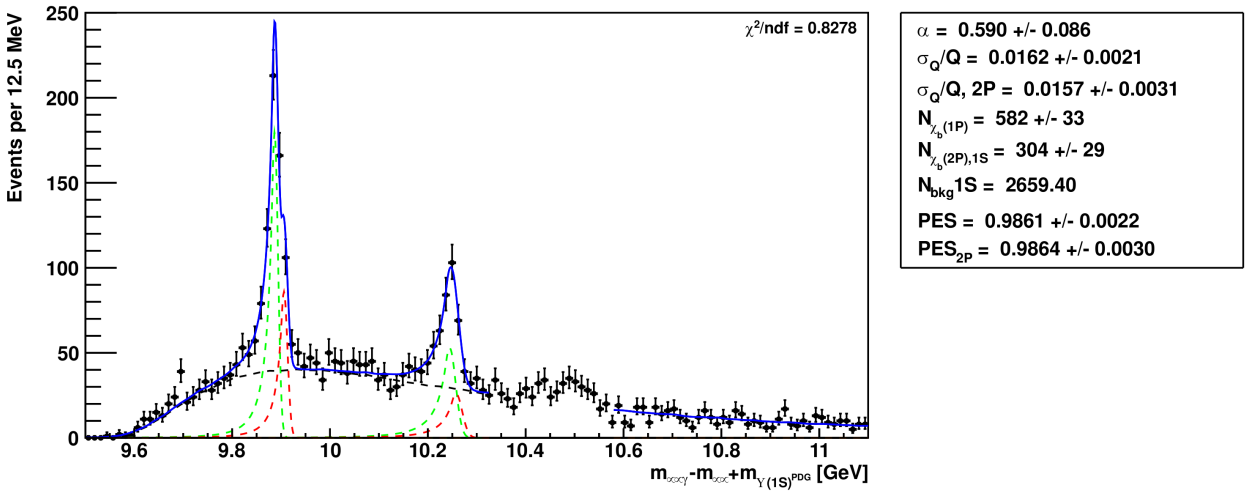

Figure 5.4: Fit to the Q-value of resonances χ_b 1P and 2P from [28].

Figure 5.5 shows the plot of the PES evaluated with the above method as a function of Q-value and it's fit using a constant function.

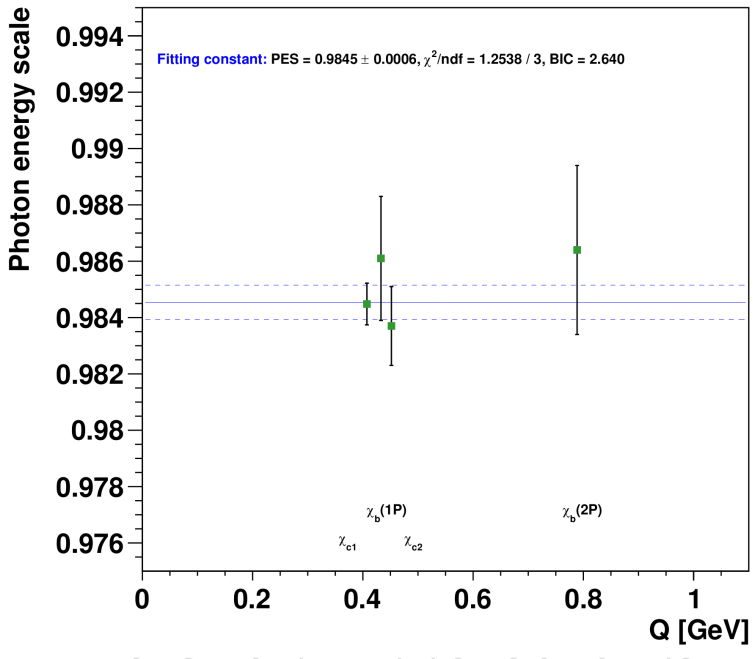

Figure 5.5: Plot of the PES as function of measured Q-value with data-driven method

The result, $f_{PES} = 0.9845 \pm 0.0006$, is not statistically compatible with the one previously found with Monte Carlo method. The variation of the mass resulting from the use of one correction and the other will be considered as a systematical error.

5.3 Systematic uncertainties

The lack of knowledge of the relative abundancy of J=1 and J=2 is treated as systematic uncerainty. Several fits are performed where in each a different value of the ratio of J=2 over J=1 is used. The greater and smaller values of the PES thus obtained are used to calculate the corrected mass. The values obtained are: $m^{low}_{\chi_b(3P)} = 10.504$ GeV and $m^{high}_{\chi_b(3P)} = 10.509$ GeV. The extreme values are considered and the systematic uncertainty is then evaluated to be $^{+0}_{-0.05\%}$.

The uncertainty on the determination of the PES value is taken as a source of systematic uncertainty. The value of the mass obtained from Monte Carlo evaluated PES is 10.509 ± 0.004 GeV while the value obtained with data-driven method gives 10.510 ± 0.004. Therefore a $\pm 0.01\%$ systematic error is assigned.

The sensitivity of the mass measurement to the selection cuts is taken as a source of systematic uncertainty. Several fits are again performed varying the the kinematical cut the mass is most sensible to: the photon p_T selection. The resulting masses as function of the photon p_T cut are shown in table 5.2. The plots obtained with the different kinematical cuts are shown in Appendix A.

$p_T^\gamma >$	mass [GeV]	χ^2/ndf	χ^2 prob
0.0	10.50±0.07	0.82	1.0
0.2	10.50±0.01	0.88	1.0
0.4	10.51±0.01	1.03	1.0
0.6	10.507±0.007	0.9	1.0
0.8	10.509±0.008	0.65	1.0
1.0	10.517±0.005	0.54	1.0
1.2	10.514±0.005	0.5	1.0
1.4	10.514±0.007	0.65	1.0
1.6	10.514±0.006	0.69	1.0
1.8	10.510±0.007	0.66	1.0

Table 5.2: Table of PES corrected masses for various photon p_T cuts

The greater deviations from the evaluated mass are $m^{low}_{\chi_b(3P)} = 10.50$+/-0.01 GeV and $m^{high}_{\chi_b(3P)} = 10.517$+/-0.005 GeV, therefore the systematic error is $^{+0.08\%}_{-0.09\%}$.

The sensitivity of the PES measurement to the selection cuts is considered. Kinematical selections used on data analysis are applied to the Monte Carlo samples in order to evaluate a possible variation in reconstructed mass and, therefore, a possible variation in calculated PES. The PES calculated with kinematical cuts on simulation samples show no statistically significant variation from the value obtained without cuts. No systematic error is assigned from this study.

The error deriving from the fit of the PES is also considered a systematical error. Its value is obtained multiplying the uncorrected mass value of 10.494 GeV by the statistical error on PES value of 0.0004. The result is ±0.04%.

The theorical work in [2] evaluate a hyperfine splitting for J=1 and J=2 of 16 MeV, different from the 12 MeV used for the barycenter calculation. The uncertainty on the mass difference between the two spin states is considered another source of systematic uncertainty. Fitting the Q-value with a fixed mass difference of 16 MeV between the J=1 and J=2 bring a mass of $m_{chi_b(3P)} = 10.507$+/-0.004 GeV. The systematic error is thus ±0.02%.

Finally all the systematic errors are considered as the squared sum of the single contributions. The result is: $^{+0.09\%}_{-0.11\%}$.

The individual systematic errors constributions are summarized in table 5.3

Uncertainty source	Evaluated error [MeV]
Spin state ratio	$^{+0}_{-0.05\%}$
PES model uncertainty	±0.01%
PES sensitivity to cuts	*non significant*
Mass sensitivity to cuts	$^{+0.08\%}_{-0.09\%}$
PES fit	±0.04%
$\Delta m^{J=2}_{J=1}$ from [2]	±0.02%
Squared sum of all errors	$^{+0.09\%}_{-0.11\%}$

Table 5.3: Summary table of systematic errors.

5.4 Result

The final result of the mass barycenter of 3P system is evaluated using the PES factor obtained from Monte Carlo samples.

The resulting mass is: $m_{\chi_b(3P)} = 10.509 \pm 0.004(\text{stat.})^{+0.009}_{-0.011}(\text{syst.})$ GeV.

The calculated $\chi_b(3P)$ barycenter is, within errors, in agreement with the theorical prediction in [30] which predicts a 3P barycenter of 10.520 GeV and close, but not agreeing, with [20] whose prediction is 10.525 GeV.

The ATLAS experiment, with his work [25], calculated a mass of $10.539 \pm 0.004(\text{stat.}) \pm 0.008(\text{syst.})$ which lies outside of this work evaluation.

A great source of systematic uncertanties comes from the approximate evaluation of the PES: a deep study of the energy the photons lose in the conversion examinated as function of the photons energy, rather than their Q-value, would probably bring more precise results and possibly even a different behavior of the PES (which, probably, is not constant as function of photon p_T). A more precise knowledge of the PES would, therefore, lower the systematic error on the evaluation of the 3P barycenter.

Moreover the total 2012 data will be on much more integrated luminosity than ever before and with that a much greater yield of 3P states, studying which will increase the precision of its mass measurement.

Chapter 6

Conclusions

Three different measures of the properties of the P-wave states of the Bottomonium where done.

The data sample originates from pp collisions at LHC recorded in 2011 for a total of 4.7 fb^{-1} of integrated luminosity.

In the kinematic range $p_T(\gamma) > 0.5$ GeV and $|y(\Upsilon)| < 1.0$ the production cross-section ratio of χ_{b2} over χ_{b1} of the 1P triplet was measured and its value found to be compatible to the one measured for the χ_c in [26] of:

$$\frac{\sigma_{\chi_{c2}}}{\sigma_{\chi_{c1}}} = 0.759 \pm 0.025(stat.) \pm 0.015(syst.) \pm 0.043(BR) \tag{6.1}$$

In the same kinematic range the production cross-section ratio of 2P over 1P states of bottomonium was measured:

$$\frac{\sigma(pp \to \chi_b(2P))}{\sigma(pp \to \chi_b(1P))} = 1.1 \pm 0.1(stat.) \pm 0.2(syst.) \pm 0.1(BR) \tag{6.2}$$

The kinematic range $p_T(\gamma) > 1.0$ GeV and $|y(\Upsilon)| < 1.0$ is instead used to study the 3P resonance. Its barycenter evaluated to be:

$$m_{\chi_b(3P)} = 10.509 \pm 0.004(stat.)^{+0.009}_{-0.011}(syst.) \text{ GeV} \tag{6.3}$$

Agreement with theory predictions and previous experimental results are discussed.

Appendix A

3P barycenter different $p_T(\gamma)$ cut

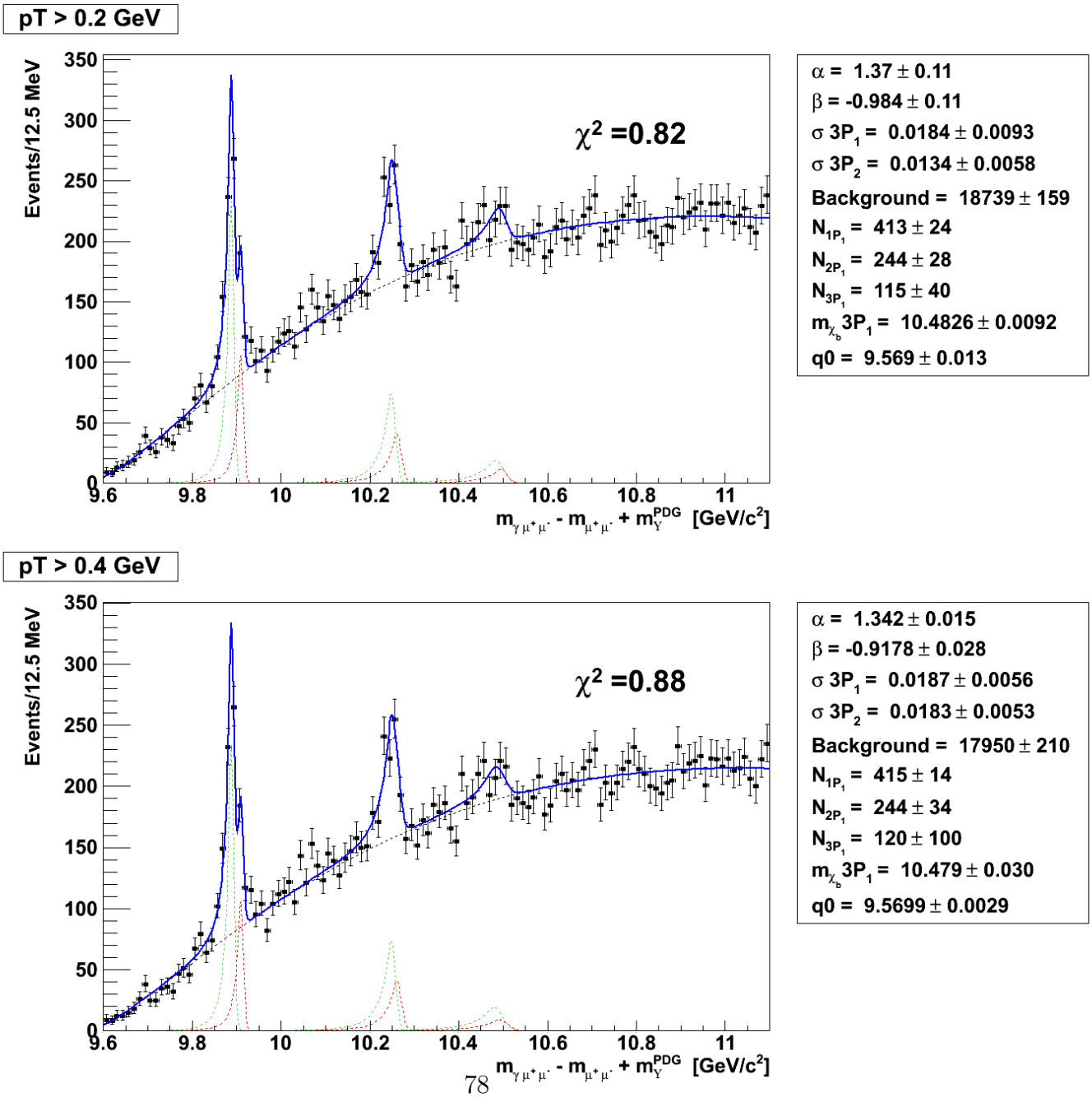

Figure A.1: 3P barycenter for $p_T(\gamma) > 0.2$ and 0.4 GeV.

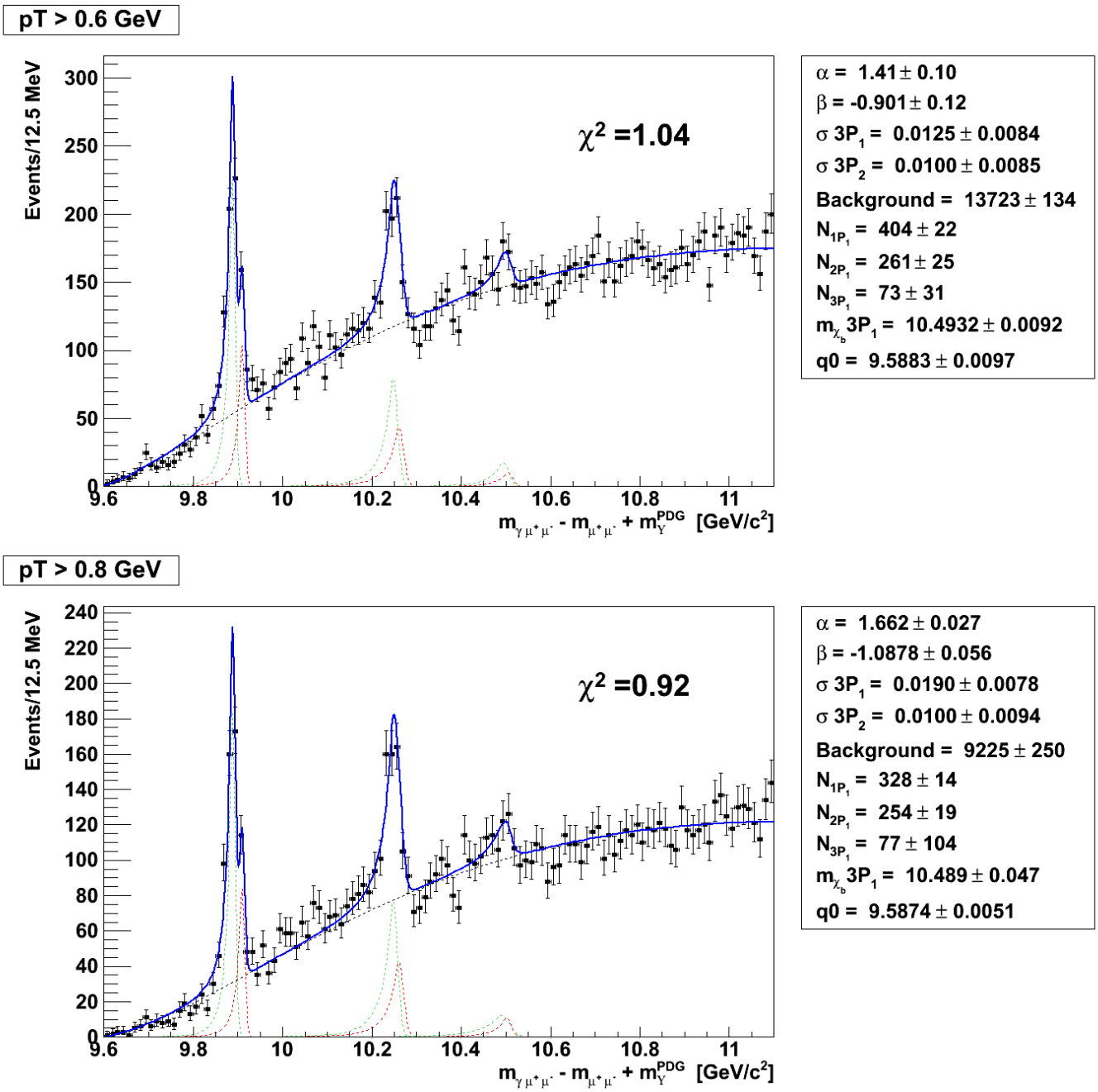

Figure A.2: 3P barycenter for $p_T(\gamma) > 0.6$ and 0.8 GeV.

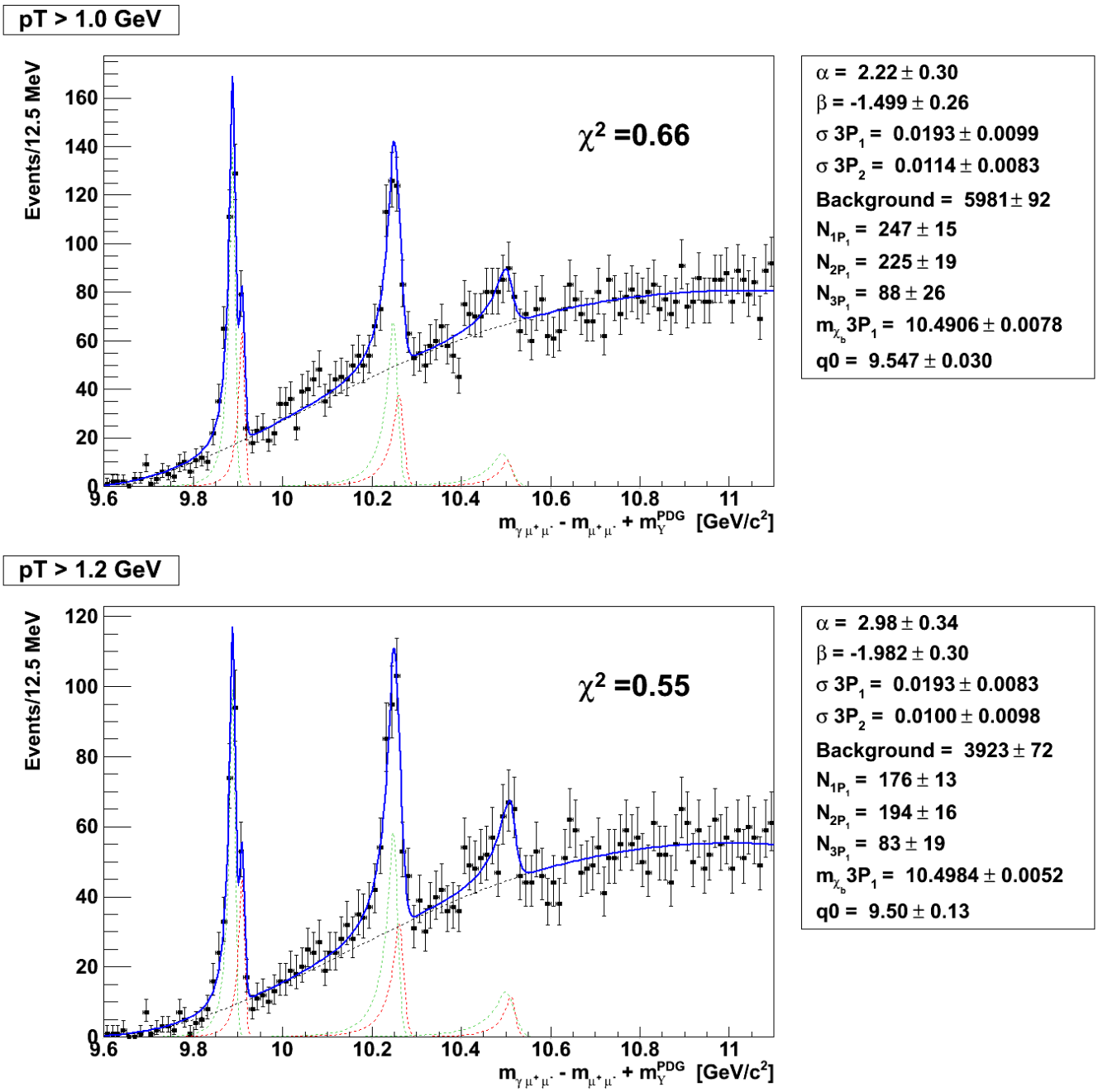

Figure A.3: 3P barycenter for $p_T(\gamma) > 1.0$ and 1.2 GeV.

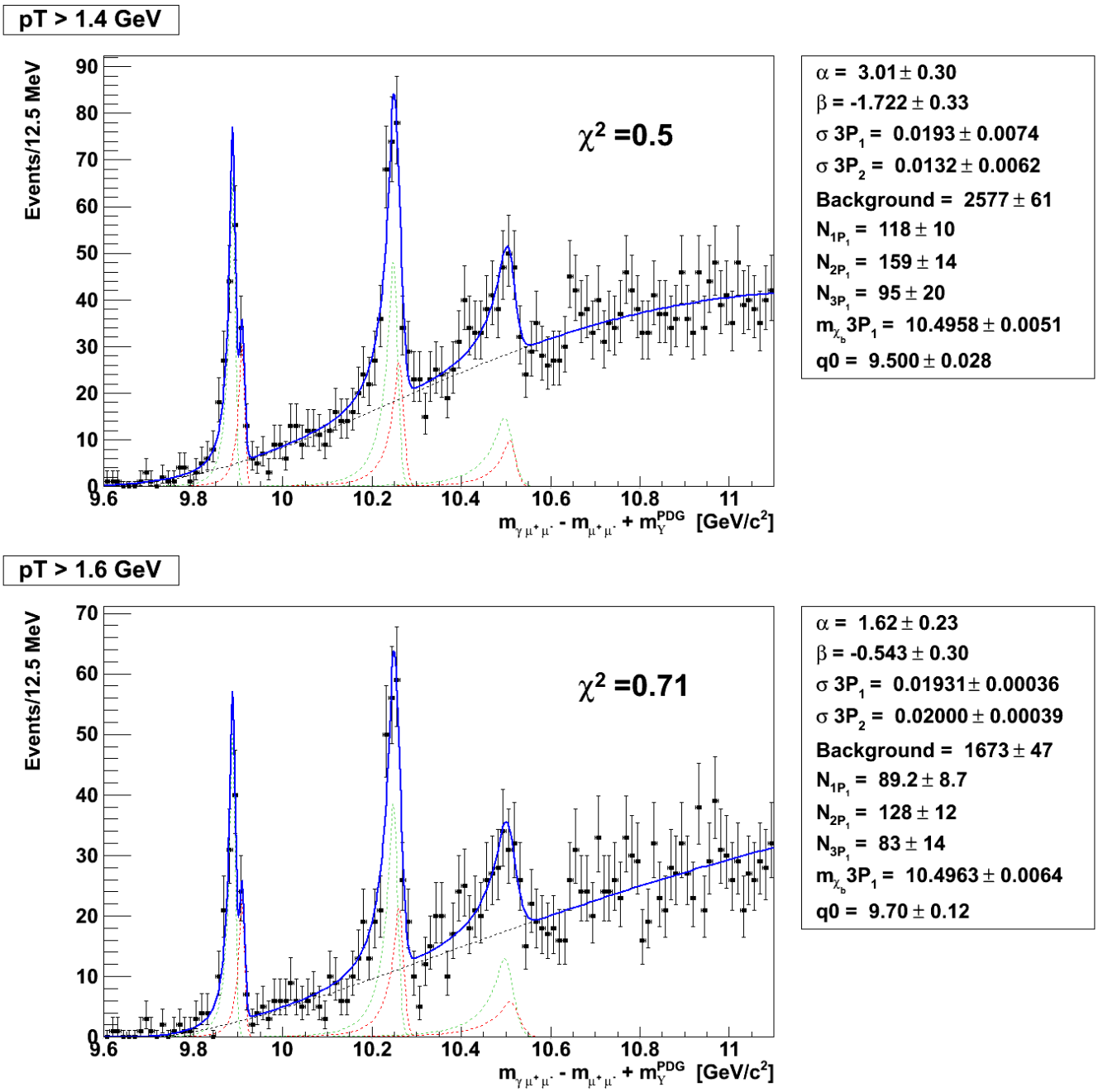

Figure A.4: 3P barycenter for $p_T(\gamma) > 1.4$ and 1.6 GeV.

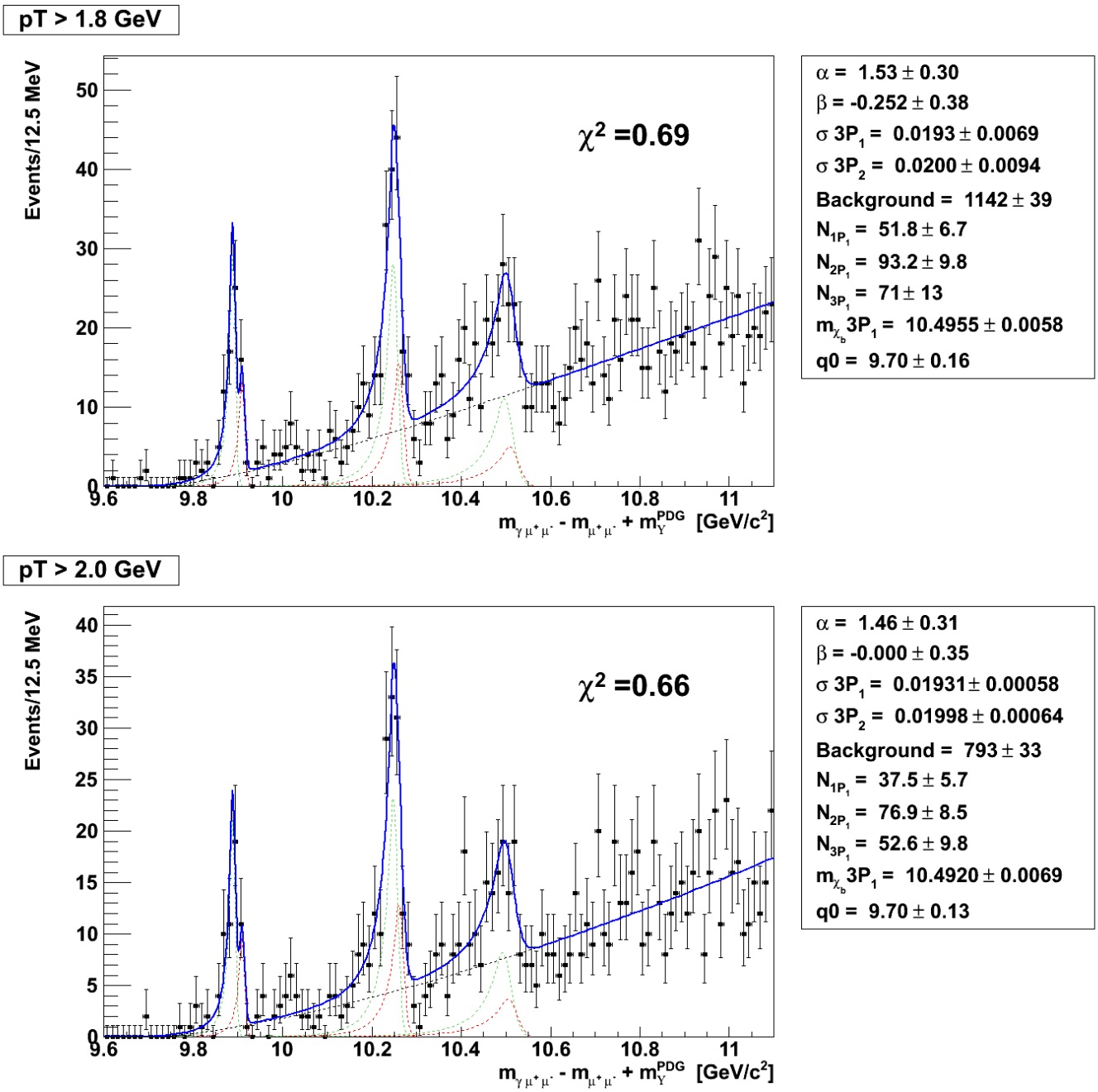

Figure A.5: 3P barycenter for $p_T(\gamma) > 1.8$ and 2.0 GeV.

Appendix B

Event Displays

Here are reported some event displays of χ_b candidates taken from the 2011 run.

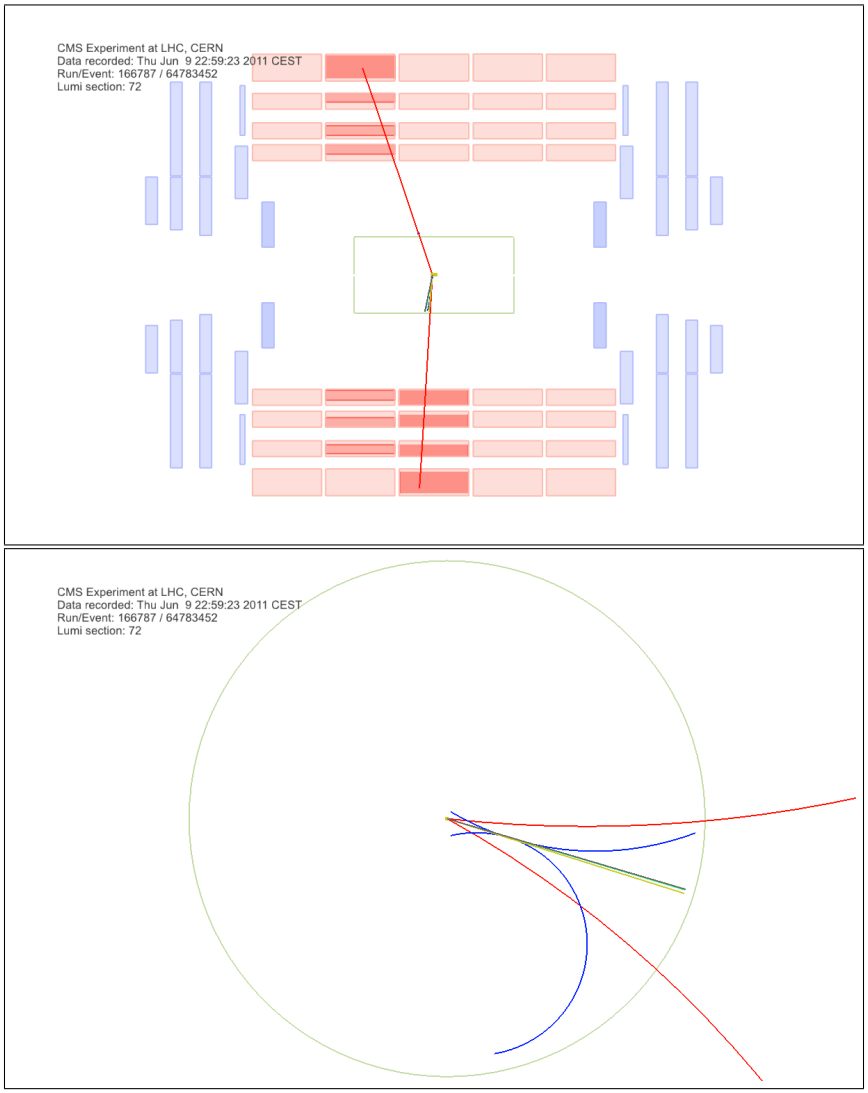

Figure B.1: Red: μ, yellow: γ candidate, blue: conversion e, light green: χ_b candidate, gray: Υ candidate, dark green: other tracks

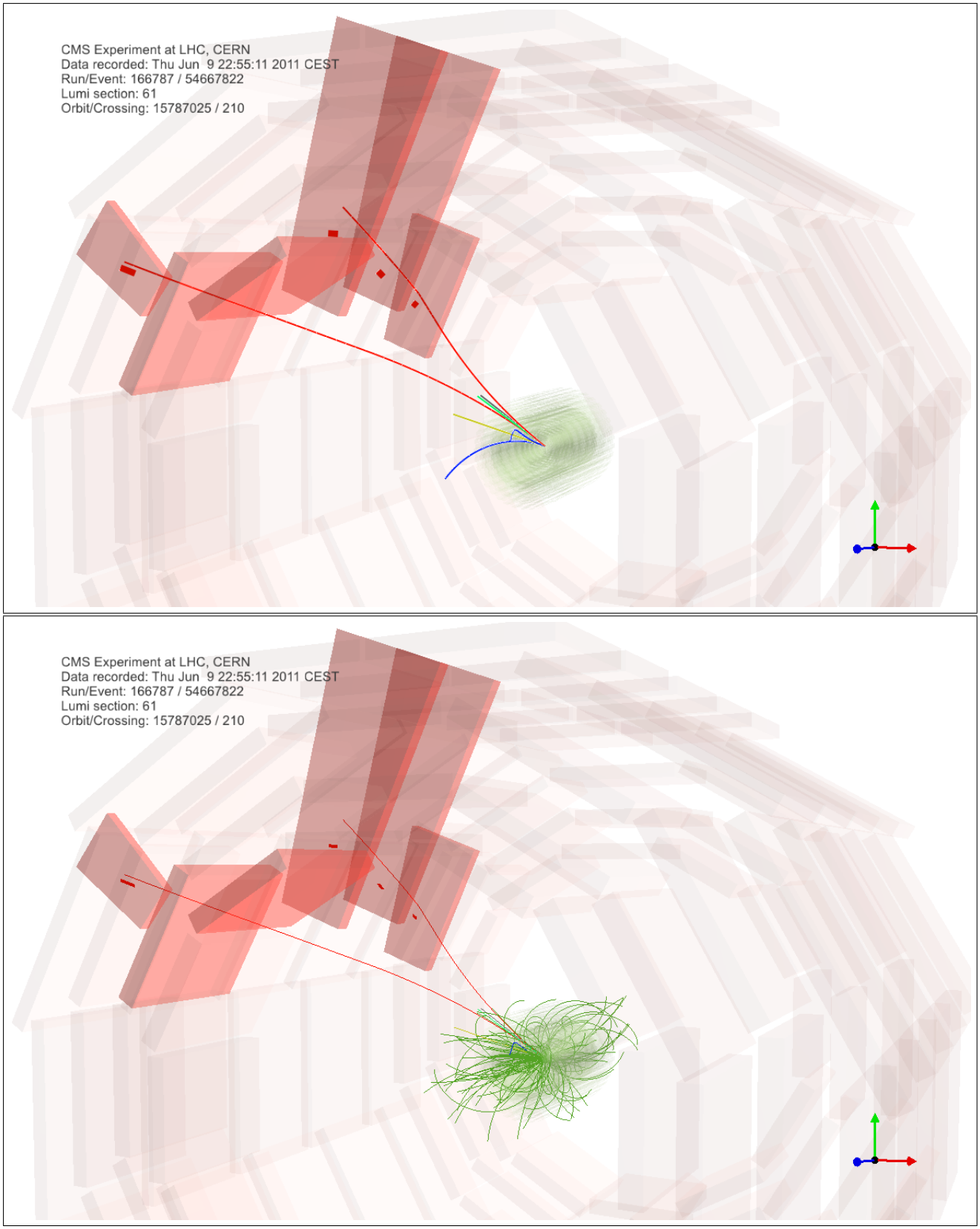

Figure B.2: Red: μ, yellow: γ candidate, blue: conversion e, light green: χ_b candidate, gray: Υ candidate, dark green: other tracks

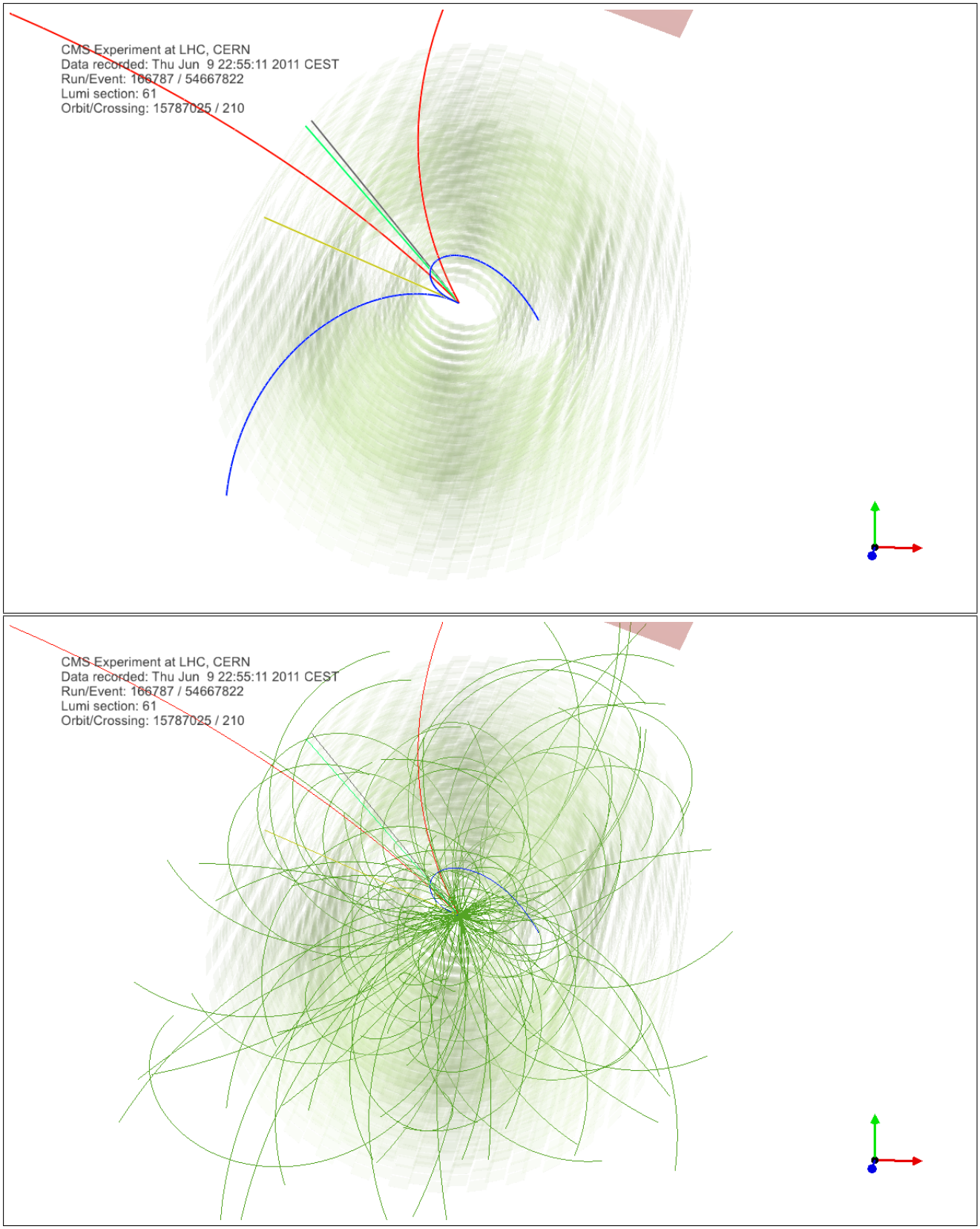

Figure B.3: Red: μ, yellow: γ candidate, blue: conversion e, light green: χ_b candidate, gray: Υ candidate, dark green: other tracks

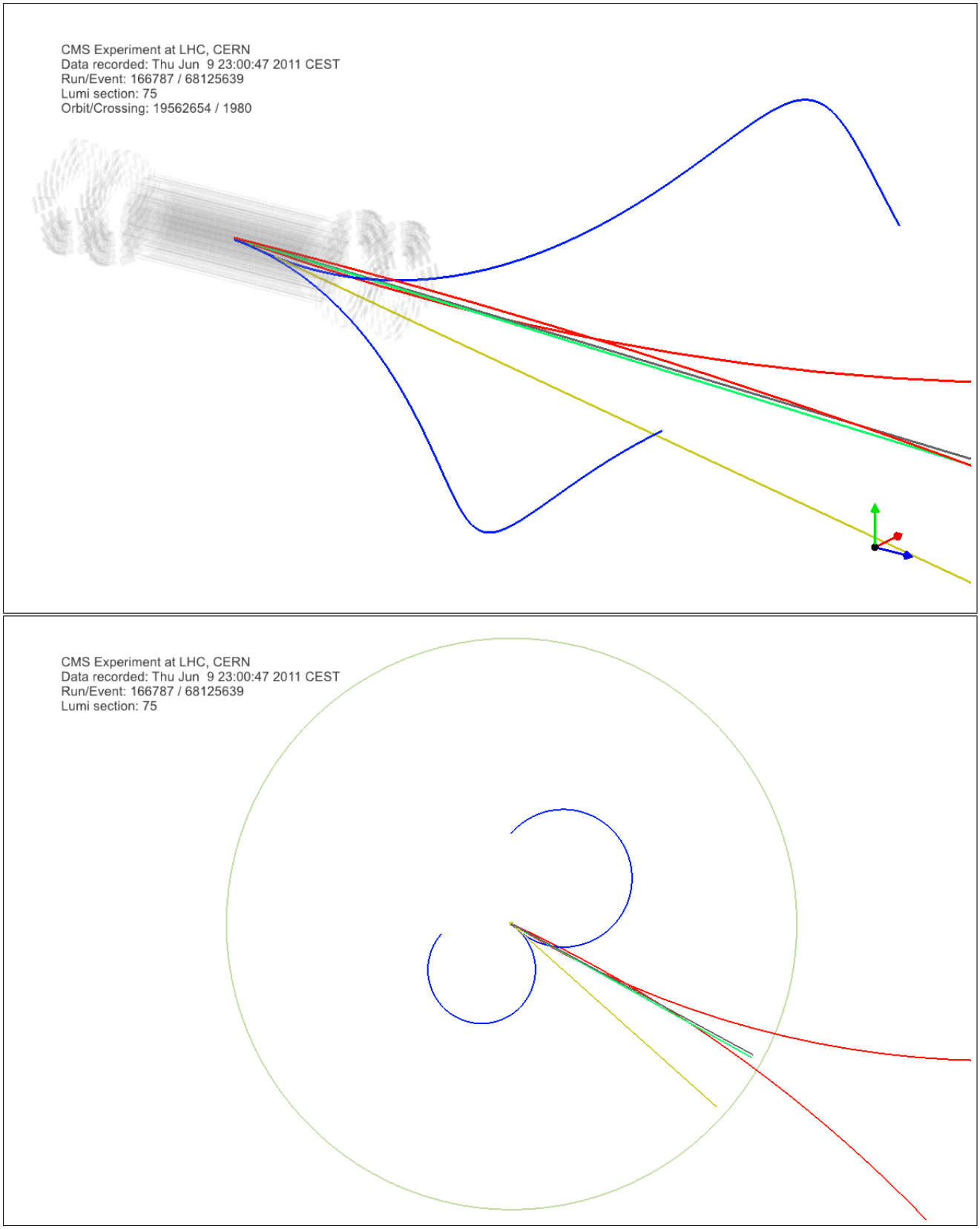

Figure B.4: Red: μ, yellow: γ candidate, blue: conversion e, light green: χ_b candidate, gray: Υ candidate, dark green: other tracks

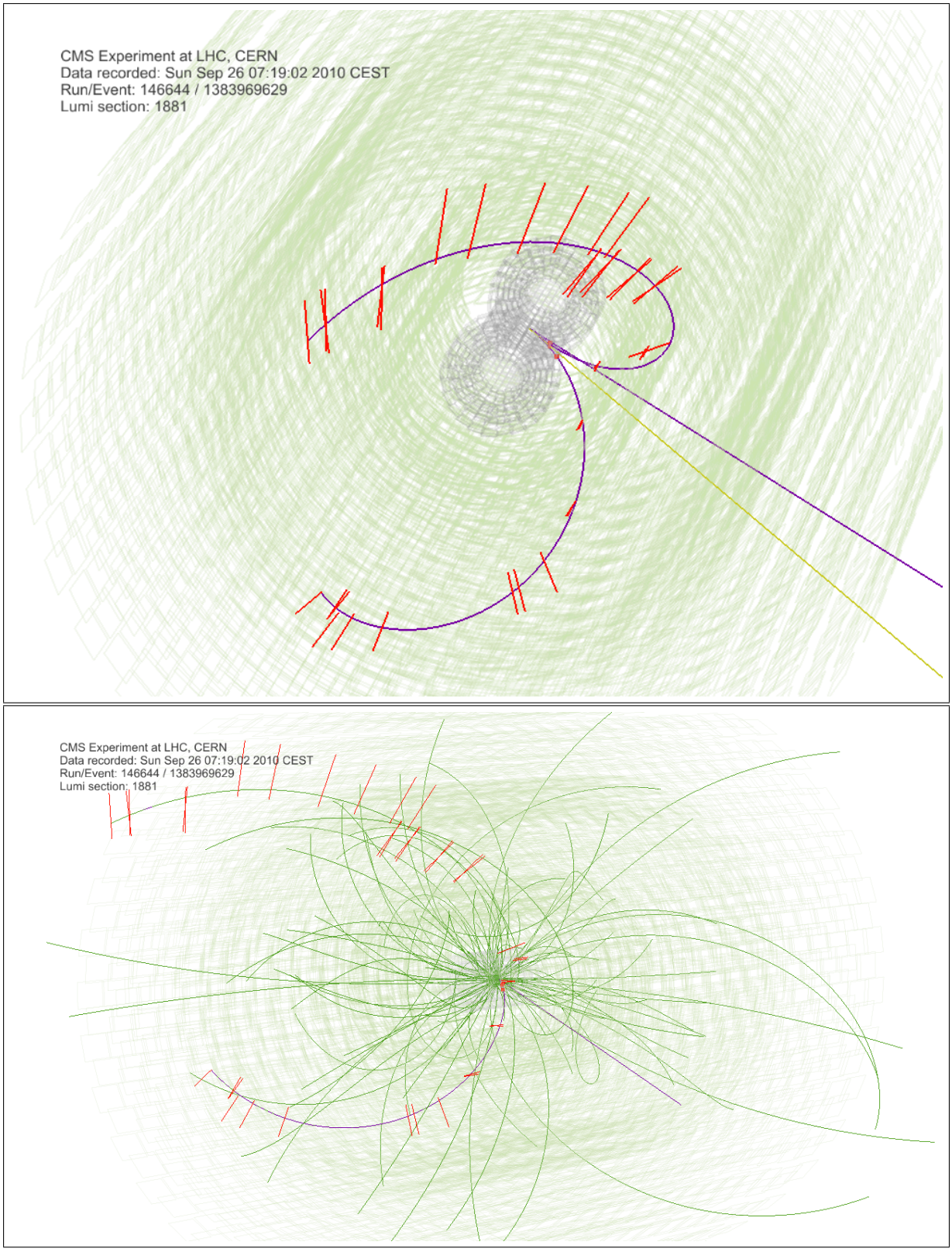

Figure B.5: Event display

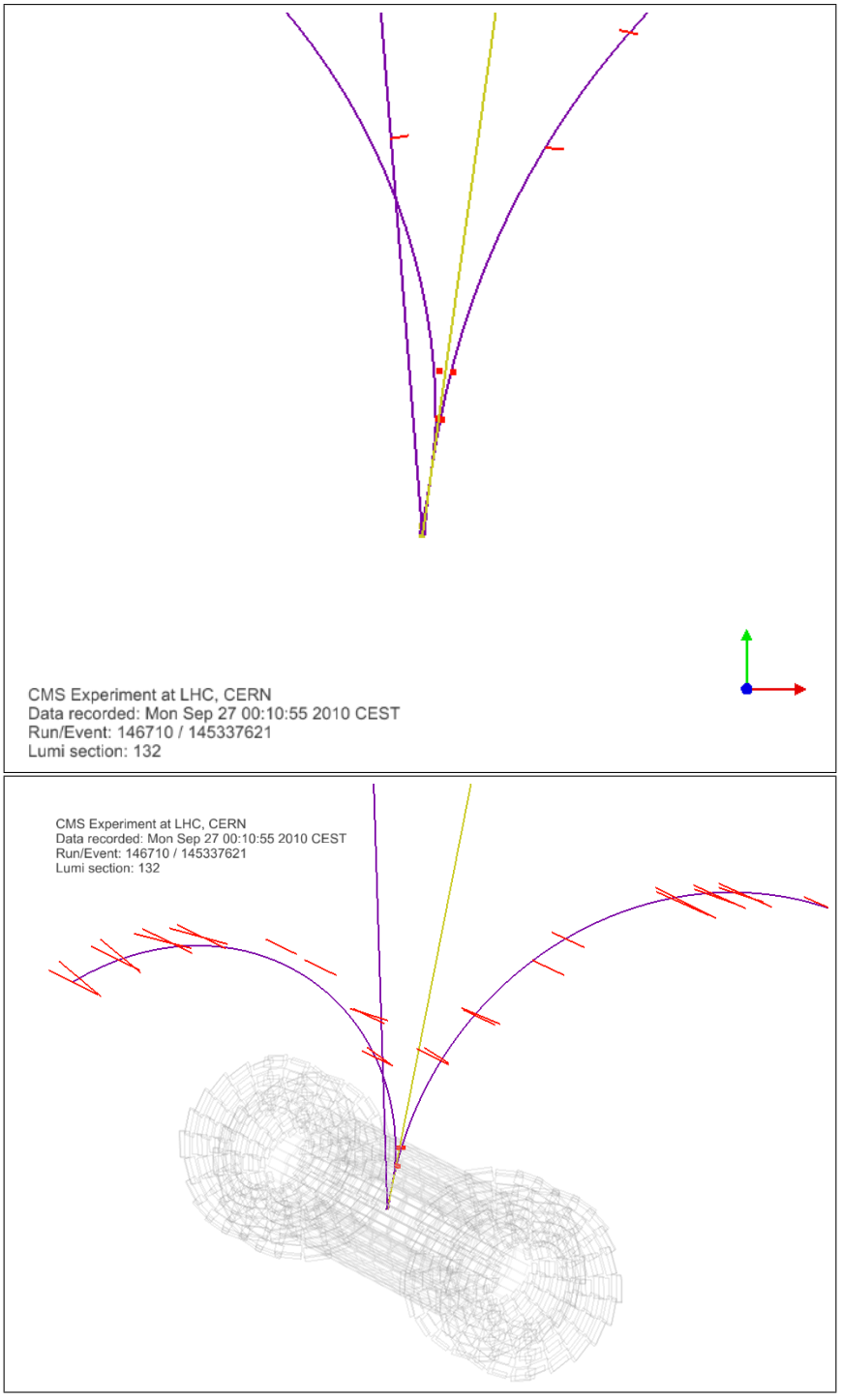

Figure B.6: Event display

Bibliography

[1] S.V. Poslavsky A.K. Likhoded, A.V. Luchinsky. Production of χ_b-mesons at LHC. *arXiv:hep-ph1203.4893v2*, 2012.

[2] Kuang-Ta Chao Bai-Qing Lia. Bottomonium spectrum with screened potential. *arXiv:0909.1369v1 [hep-ph]*, 2009.

[3] Y. Keung V.D. Barger and R.J. Phillips. *Phys.Lett. B, 91:253*, 1980.

[4] W. E. Caswell and G. P. Lepage. Effective lagrangians for bound state problems in qed, qcd, and other field theories. *Phys.Lett. B, 167:437*, 1986.

[5] The CMS collaboration. The magnet project technical design report tech.rep. *CERN/LHCC 97-10 and CMS TDR1, CERN*, 1997.

[6] The CMS collaboration. The Tracker Project, Technical Design Report. *CERN/LHC 1998-006, CMS TDR 5*, 1998.

[7] The CMS collaboration. Detector performance and software, physics technical design report, vol. i. *CERN/LHC 2006-001, CMS TDR 8.1*, 2006.

[8] The CMS collaboration. J/ψ prompt and non-prompt cross sections in pp collisions at $\sqrt{s} = 7TeV$. *CMS PAS BPH-10-002*, 2010.

[9] The CMS collaboration. Studies of tracker material. *CMS-PAS-TRK-10-003*, 2010.

[10] The CMS collaboration. Tracking and vertexing results from first collisions. *CMS-PAS-TRK-10-001*, 2010.

[11] The CMS Collaboration. Measurement of the $\Upsilon(nS)$ cross-section in pp collisions at $\sqrt{s} = 7TeV$. *CMS BPH-11-001*, 2012.

[12] K. Anikeev et al. B physics at the tevatron: Run ii and beyond. 2002.

[13] M. Raymond et al. The CMS Tracker APV25 0.25 mm CMOS Readout Chip. *Proceedings of the 6th workshop on electronics for LHC experiments, Krakow, Poland*, 2000.

[14] R. Adolphi et al. The CMS experiment at the CERN LHC. *JINST 0803*, 2008.

[15] H. Fritzsch. *Phys.Lett. B, 67:217*, 1977.

[16] Eric Braaten Geoffrey T. Bodwin and G. Peter Lepage. Rigorous qcd analysis of inclusive annihilation and production of heavy quarkonium. *ERRATUM-IBID.D, 55:5853*, 1997.

[17] J.F. Owens M. Glock and E. Reya. *Phys.Lett. D, 17:2324*, 1978.

[18] F. Halzen. *Phys.Lett. B, 69:105*, 1977.

[19] Jia-Feng Liu, Gui-Jun Ding. Bottomonium Spectrum with Coupled-Channel Effects. *arXiv:hep-ph/1105.0855v2*, 2012.

[20] K. Zalewski L. Motyka. Mass spectra and leptonic decay widths of heavy quarkonia. *arXiv:hep-ph/9709254v1*, 1997.

[21] L. Motyka and K. Zalewski. Mass spectra and leptonic decay widths of heavyquarkonia. *Eur. Phys. J. C 4 (1998) 107*, 1998.

[22] LHC Higgs Cross Section Working Group Handbook of LHC Higgs Cross Sections. 1. inclusive observables. *arXiv:1101.0593*.

[23] The LHC study group. Lhc the large hadron collider: conceptual design. *CERN/AC/95-05 vol.II*, 1995.

[24] B. A. Thacker and G. Peter Lepage. Heavy-quark bound states in lattice qcd. *Phys.Lett. D, 43(1):196-208*, 1991.

[25] The Atlas Collaboration. Observation of a new χ_b state in radiative transitions of $\Upsilon(1S)$ and $\Upsilon(2S)$ at ATLAS . *CERN-PH-EP-2011-225*, 2011.

[26] The CMS Collaboration. Measurement of the relative prompt production rate of χ_{c2} and χ_{c1} in pp collisions at $\sqrt{s} = 7TeV$. *CMS PAS BPH-11-010*, 2012.

[27] The D0 Collaboration. bservation of a narrow mass state decaying into $\Upsilon(1S) + \gamma$ in $p\bar{p}$ collisions at $\sqrt{s} = 1.96$ TeV. *arXiv:hep-ex/1203.6034v1*, 2012.

[28] Valentin Knünz, Carlos Lourenco, Domenico Giordano, Muhammad Ahmad, Ernest Aguilo, Ilina Akin, Stefano Argiro, Alessandro Degano, Candan Dozen, Pietro Faccioli, Gul Gokbulut and Giacomo Sguazzoni. χ_b production in pp collisions at $\sqrt{s}$= 7 TeV. *CMS draft analysis note*, 2012.

[29] D. Kirkby W. Verkerke. The roofit toolkit for data modeling. *arXiv:03061116*.

[30] Jonathan L. Rosner Waikwok Kwong. D-wave quarkonium levels of the Υ familty. *Pysical Review D,38,1*, 1988.